Charles University in Prague
Faculty of Mathematics and Physics

DOCTORAL THESIS

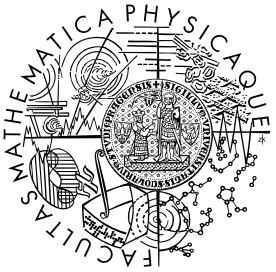

Eva Schmoranzerová,
née Rozkotová

Spin dynamics in GaAs-based semiconductor structures

Department of Chemical Physics and Optics

Supervisor: Doc. RNDr. Petr Němec, Ph.D.
Field of study: Physics
Specialization: Quantum Optics and Optoelectronics (F6)

Prague 2012

ACKNOWLEDGMENT

I would like to take the opportunity to express my gratitude to the people without whom I would be hardly able to present my work in its current form.

My biggest thanks belong to my supervisor Petr Němec, for the hours spent in scientific discussions and helping me with the experiments, for the immense patience he showed towards my work and for the moral support and endless source of motivation that he gave me. Miroslav Dušek, our technician, deserves my huge gratitude for his help with the strain gauge measurement and for the overall technical support of all the experiments. To František Trojánek I am grateful for excellent control software for the measurements which he created and for its prompt upgrades whenever needed. To Anna Fučíková and Jan Alster I am indebted for their practical help and tinkering lessons during the hybrid structures preparation. I must not forget all my fellow department students for creating a group with an atmosphere that everybody would like to work in, and for becoming not only my colleagues but also my friends. Above all, I would like to thank Nada Tesařová, with whom I had the pleasure to collaborate most closely as we shared a similar expertise.

From my colleagues from the Academy of Sciences I am indebted to Kamil Olejník and Vít Novák for supplying the excellent samples, and for introducing me to the SQUID measurement technique. I also acknowledge fruitful theoretical discussions with Jan Zemen, and Tomáš Jungwirth who provided all the theoretical background for our experiments.

My very special thanks belong to Jörg Wunderlich who gave me the opportunity to work for nine months in Hitachi Cambridge Laboratory, welcomed me in a very friendly manner and who included me into a top research project. To Byong-Guk Park I would like to thank for all the help during the laboratory work. I am also deeply grateful to my other Hitachi collegues, for many useful discussions and for making my stay in Cambridge a pleasant experience. In particular, Elisa de Rannieri deserves my thanks not only for all the hours spent introducing me into the piezo-stressor technology but also for being my very good friend and guide during my stay in Cambridge.

Finally, I would like to express my huge gratitude to my parents. Without their support, patience and also a bit of technical help I could not finish this work. To my husband I am immensely grateful for standing unconditionally beside me, for helping me whenever I needed and for making my life full of pleasure. Finally, I also thank my babies Lada and Filip, who gave me lots of joy and half an hour a day to work.

Prohlašuji, že jsem tuto disertační práci vypracoval(a) samostatně a výhradně s použitím citovaných pramenů, literatury a dalších odborných zdrojů.

Beru na vědomí, že se na moji práci vztahují práva a povinnosti vyplývající ze zákona č. 121/2000 Sb., autorského zákona v platném znění, zejména skutečnost, že Univerzita Karlova v Praze má právo na uzavření licenční smlouvy o užití této práce jako školního díla podle § 60 odst. 1 autorského zákona.

V Praze, dne 10. 4. 2012

podpis

Název práce: *Spinová dynamika v polovodičových strukturách založených na GaAs*
Autor: *Eva Schmoranzerová, née Rozkotová*
Katedra (ústav): *Katedra chemické fyziky a optiky*
Vedoucí disertační práce: *doc. RNDr. Petr Němec, Ph.D.*

ABSTRAKT: Tato práce se zabývá studiem spinové dynamiky v polovodičových systémech vhodných pro spintroniku, které jsou založeny na polovidiči galium arsenid (GaAs). Pomocí metod ultrarychlé laserové spektroskopie a transporního měření jsme zkoumali dva typy modelových polovodičových struktur.
Ve feromagnetickém polovodiči (Ga,Mn)As jsme se zabývali laserem vyvolanou precesí magnetizace. Zjistili jsme, že původem této precese může být nejen přenos energie z laserových pulsů, ale také přenos úhlového momentu z kruhově polarizovaného světla na elektrony a následně na magnetické momenty. Tento optický „spin transfer torque" je zcela novým jevem pozorovaným poprvé v rámci této práce. Dále jsme ukázali možnost kontroly precese magnetizace vyvolané přenosem energie, a to jak čistě opticky, tak elektricky za použití piezo měničů.

V oblasti čistě nemagnetické spintoniky jsme studovali nízkodimenzionální struktury založené na GaAs/AlGaAs kvantových jámách se speciálním typem spin orbitální (SO) vazby, které vykazují Hallův jev související s injecí spinově polarizovaných nosičů (SIHE). Tyto struktury byly litograficky zpracovány do formy dvojdimenzionální planární fotodiody. V našich experimentech jsme dokázali přímo elektricky detekovat precesi spinových momentů elektronů v SO poli, což je rozšířením původního SIHE. Tato metoda, společně s detekcí čistě spinového proudu uskutečněného v této práci, později přispěla k úspěšné realizaci spinového tranzistoru.

Klíčová slova: spintronika, magnetické polovodiče, spin injection Hall effect

Title: *Spin dynamics in GaAs-based semiconductor structures*
Author: *Eva Schmoranzerová, née Rozkotová*
Department: *Department of Chemical Physics and Optics*
Supervisor: *doc. RNDr. Petr Němec, Ph.D.*

ABSTRACT: This work is dedicated to the study of spin dynamics in systems based on the semiconductor gallium arsenide (GaAs) that are suitable for use in spintronic devices. We explored two types of model structures using experimental methods of ultrafast laser spectroscopy and transport measurements.
In the ferromagnetic semiconductor (Ga,Mn)As, we investigated laser-induced magnetization precession. We found out that transfer of both energy and angular momentum from the circularly polarized laser light can trigger magnetization precession, the latter one being identified as a new phenomenon, the "optical spin transfer torque". Furthermore, we demonstrate the possibility to control the energy-transfer-induced magnetization dynamics both optically and electrically using piezo-stressing.
When dealing with purely non-magnetic structures for spintronics, we studied the Spin-Injection Hall Effect (SIHE) in GaAs/AlGaAs heterostructures with a special type of spin- orbit (SO) coupling that are lithographically patterned to create a two dimensional planar photodiode. We managed to observe precession of the electron spin in the SO field directly in the space domain by extending the original detection method. This finding, together with the direct detection of a pure spin current, helped to propose a working spin Hall effect transistor.

Keywords: spintronics, magnetic semiconductors, spin injection Hall effect

PREFACE

In the last decade, there has been a huge development in the field of electronics. This success is also related to the invention of a new concept called "spintronics", which uses the spin of charge carriers to process and store information. Spintronics already offers many applications, such as hard disk read heads or magnetic sensors, all of which are based on metallic materials and use spin-polarized carriers in ferromagnets. However, even greater application potential lies in the incorporation of spintronics into commercial semiconductor-based devices, for which it is crucial to bring the two separate fields together. In principle, two possibilities exist for such unification. The first one assumes fabrication of materials that allow for ferromagnetic order while maintaining semiconducting properties, while the other possibility lies in taking advantage of strong spin-orbit coupling in existing semiconductors.

The first approach mentioned has lead to the development of so called "diluted magnetic semiconductors" (DMS), common semiconductors doped with magnetic ions, with a typical representative in the (Ga,Mn)As system. A special kind of carrier-mediated ferromagnetism that occurs in DMS pushes the structures far beyond the simple magnetic-semiconductor concept. It turns out that ferromagnetic order itself can be controlled by injection of carriers (by gating, optically etc.), opening the door for a whole range of new applications in reprogrammable logic devices, new generation of magnetic memories, etc. Unfortunately, several technological issues remain unresolved in these materials. Perhaps the most important one is the low ferromagnetic transition temperature, which still lies far below room temperature (maximum of 190 K in (Ga,Mn)As).

Therefore, the interest of scientists is attracted towards the concept of spintronics where there is no need for ferromagnetic order and thus it is possible to work with common semiconductors (such as GaAs and its nanostructures) at room temperature, avoiding the problems of new material research. In such "non-magnetic" devices the spin-orbit interaction (SO), which couples orbital moments of the carriers to their spin, is the driving force that manipulates the spin moments of carriers. Tuning the SO coupling by means of nanopatterning or by external electric field can affect the carrier spins directly, which forms the basis for the operation of spin field effect transistors and other logic operation devices.

This thesis is dedicated to the study of materials and pre-fabricated devices to be used in both spintronic concepts by the experimental methods of Hall transport measurements and time-resolved magnetooptics. The aim was to investigate processes connected with spin dynamics, with emphasis on a possibility of their external control by the means of laser light and electrical field. This thesis reports on two sets of experiments – studies of (Ga,Mn)As and its hybrid multiferroic structures performed in the laser laboratory of the Department of Quantum Optics and Optoelectronics at Charles University in Prague, and work on spin dynamics in non-magnetic GaAs quantum well systems, conducted in cooperation with the Hitachi Cambridge Laboratory, where also some of the devices studied in Prague had been produced.

The thesis is divided into four chapters. Chapter (1) introduces basic concepts of semiconductor spintronics in context of the structures studied in this work. Chapter (2) describes experimental methods for studying spin dynamics in semiconductors, while chapters (3) and (4) are dedicated to experimental results obtained on ferromagnetic semiconductors and non-magnetic devices, respectively.

CONTENTS

1. INTRODUCTION

In this chapter we would like to briefly introduce the main concepts of spintronics whose cornerstones are semiconducting (SC) materials and devices. We will mainly focus on SC gallium arsenide (GaAs), as the presented work is devoted to systems based on this particular material. The band structure of GaAs and related heterostructures will be described, including the effects of spin-orbit interactions that determine the material behavior in terms of spin dynamics. Individual structures used in the experimental part of this thesis will be discussed in detail in chapters 3 and 4.

1.1 Semiconductor spintronics

In data storage applications, spins of charge carriers in strongly polarized ferromagnetic materials (mainly metals) are typically used, and the saved information is thus independent of power supply (the device is "non-volatile"). On the other hand, semiconductor components such as transistors use the sensitivity of the material to external electric field (gating) and serve for data processing – these components are "volatile". Semiconductors (SC) are extremely favorable materials for electronics, mainly due to the strong dependence of their behavior on doping, well managed and cheap fabrication, and also their high optical quality. Therefore, there is a strong demand on keeping SC as the base of new technologies and to incorporate new functionalities – either in the form of quantum bits on the singe-electron level or as functional extensions of standard electronic devices, such as spin – FET transistors [**1**], [**2**]. New developments meeting this demand are possible due to a typically strong spin-orbit coupling characteristic of semiconductors that opens door for fast (below 1 ps) and simple spin manipulation. However, for a practical integration of semiconductors into spintronics, certain requirements are to be fulfilled. We have to achieve significant spin polarization of the carriers, the polarization has to be remembered by a system for a sufficiently long time, and the spins have to be detected efficiently. There are several possibilities how to face these issues.

Large effort has been devoted to the concept wherein spin-polarized carriers are injected into standard SC extrinsically – either optically by absorption of circularly polarized light (see **chapter 2.1**) or through an interface with ferromagnetic metals [**3**]. The spins can be manipulated due to the presence of the spin-orbit (SO) field which is further tunable by external means – nanopatterning, strain, electric field etc. However, major drawbacks of this concept still lie in short spin lifetime resulting from various spin relaxation mechanism in standard SCs, and in the lack of efficient purely electrical injection and detection, which is desirable for device fabrication. While the first problem has already been overcome in specially designed two-dimensional quantum well (QW) systems with a highly symmetrical SO field [**4**], [**5**], the issue of spin injection still remains a challenge. Therefore, the research branched and diversified, also aiming for such materials in which spin-polarization of carriers is inherent. This can be achieved when making standard SCs ferromagnetic by doping them with magnetic ions. These artificial structures, called "diluted magnetic semiconductors" (DMS), not only represent ferromagnetic semiconductor system, but also manifest a special type of carrier mediated ferromagnetism that can be controlled by external means – optical injection of carriers, gating, strain etc. [**6**].

However, the issue of low transition (Curie) temperature still remains the major unresolved problem.

Both of the above described fields of study share the same basic principles. The functionality of the materials relies on strong spin-orbit coupling typical for SCs – whether it results in the possibility to tune spin relaxation in QWs or magnetic anisotropy in DMS systems. Both concepts also take advantage of using the common semiconductor GaAs as a base material, whose well-known band structure enables to elaborate theoretical descriptions of the observed phenomena. Furthermore, the direct band gap of GaAs that lies in visible/near infrared range (1.42 eV at room temperature) is ideal for optical injection of carriers by intraband absorption in many optical techniques, including those used in this thesis. Therefore, we will now proceed to discuss this material more in detail.

1.2 Bulk GaAs and related structures

1.2.1 Structure of bulk GaAs

GaAs is a typical representative of the group of III-V semiconductors with a zinc-blende type crystal lattice. Its overall optical and transport properties result from its band structure, which is schematically depicted in Fig. 1.1. In the case of GaAs, the conduction band (CB) is formed by electron s-states (with angular momentum $l = 0$), while at a top of the valence band *p*-states ($l = 1$) dominate [7]. If we take spin-orbit coupling (SO) into account, (orbital) angular momentum ceases to be a proper quantum number. Instead, we obtain bands with electronic states characterized by the total angular momentum $j = 1/2$ and $j = 3/2$ and its corresponding projection in the direction of quantization $j_z = -j \ldots j$. At the Γ point (for a wave vector $k = 0$), the quadruply degenerated $j = 3/2$ band, consisting of heavy holes and light holes, is split in energy by a gap Δ_0 from the $j = 1/2$ band due to SO coupling. For non-zero k-vectors there is spin splitting even between heavy and light hole bands.

The simple model of band structure presented herein remains valid only for ideal bulk crystals. In heterostructures or systems with lower dimensionality, it is strongly modified by strain and/or spatial confinement. These systems are of great importance with regard to our work and therefore they will be discussed in more detail in the following chapters.

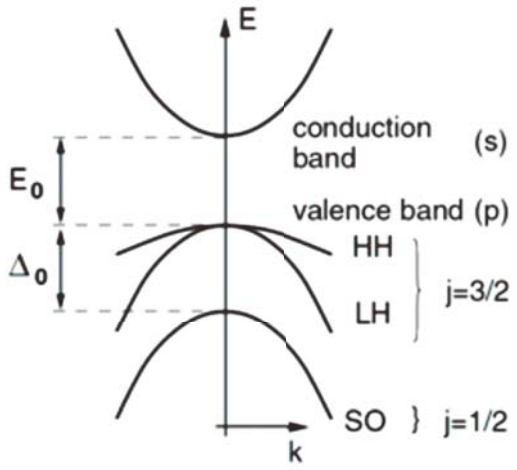

Fig. 1.1: Schematic depiction of band structure of GaAs in the vicinity of the direct band gap. [7]

1.2.2 Heterostructures

Heterostructures (HS) denotes semiconductor structures consisting of several different materials. Such systems provide the possibility of so-called "band-gap engineering" – manipulation of electron and hole states through seaming together materials with different band gaps [**8**] – which is one of the keystones of modern electronic components (diodes, transistors etc.).

There are several restrictions imposed when choosing a combination of semiconductors in order to obtain smooth interfaces. The materials have to be similar both in terms of crystal structure and lattice constants [**8**]**.** While the first condition is satisfied in many common III-V compounds, they only rarely match also in the lattice parameters *a*. The most commonly used representative of a matching compound pair is GaAs/$Al_xGa_{1-x}As$ [**8**], out of which the low-dimensional structures, such as quantum wells, superlattices etc., are fabricated.

If the condition of lattice matching is not met, strain occurs at the interface between the two layers, which breaks the inherent symmetry of the crystals [**8**], [**7**]**.** This in turn leads to further shifting and spin-splitting of the energy levels. A special case of this distortion occurs when thin layers are grown on a markedly thicker lattice-mismatched substrate. Here the main distortion happens in the thin layer in the growth direction (z), while the substrate remains unaffected. In particular, in the III-V SCs, the resulting lowering of crystal symmetry affects mainly p_z orbitals, removing their degeneracy and causing anisotropic splitting of the valence band – Fig. 1.2. An important example of this kind of layer is the ferromagnetic (Ga,Mn)As, where magnetic symmetry is strongly affected by the generated strain (see **chap. 3.1.3**). However, the impact of the strain effects on spintronics is much broader, see, e.g., refs. [**9**]-[**13**]**.**

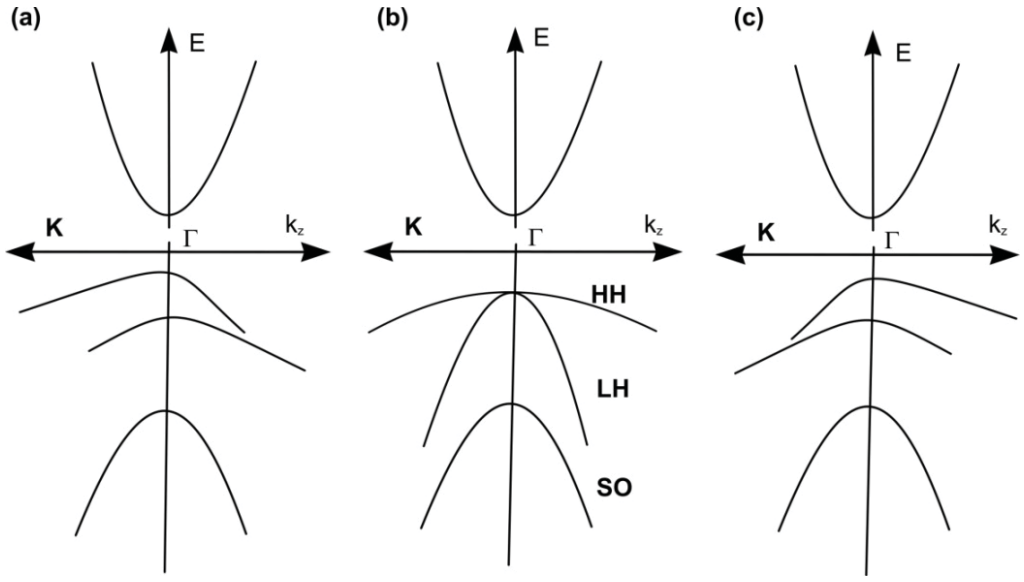

Fig. 1.2: Schematics of strain effect on band structure of a zinc-blende semiconductor. The electron/hole wave vector has components $\mathbf{k} = (\mathbf{K}, k_z)$, where z is the direction of the strain generated when the lattice constant of the substrate is larger (a) and smaller (c) than the lattice constant of the thin layer. The band diagram of an unstrained SC is shown in (b). Redrawn from ref. [**8**].

In order to ensure good conductivity of the HS, which is usually essential for device fabrication, the SCs have to be P- or N-type doped. In order to avoid unwanted impurity scattering, two types of doping are typically used in HSs. In the case of *δ-doping*, the dopants are introduced in monolayers directly during structure growth [**8**]. However, the most common method used is *modulation* or *remote doping*. Here the carriers are spatially separated from the dopants as they migrate from one region of the heterojunction to the other. This type of doping offers the possibility to create a two-dimensional electron/hole gas, a structure of great importance for high mobility electronic components (field effect transistors (FETs)) [**8**].

1.2.3 Two-dimensional electron/hole gas

Two-dimensional electron/hole gas (2DEG/2DHG) represents a system, where the carriers are trapped in a potential well in one dimension, while staying free in the other two. 2DEG is typically fabricated by modulation doping of a heterostucture, as illustrated on the example of AlGaAs/GaAs structure in Fig. 1.3. After introducing dopants (assume N-type) to the AlGaAs layer, a discontinuity of the conduction band ΔE_c of the two materials causes weakly bound electrons to migrate to the GaAs layer. Electrostatic potential of the ionized donors tends to draw the electrons back to the n-AlGaAs layer. However, due to the discontinuity in ΔE_c the electrons can only "squeeze" against the interface, trapped in a roughly triangular potential well to form an *accumulation region*. The part of n-AlGaAs from whence the carriers were removed is called the *depletion region,* in analogy with the standard diode PN junction. A spacer of undoped material (AlGaAs) can be added in order to increase the carrier density of the 2DEG.

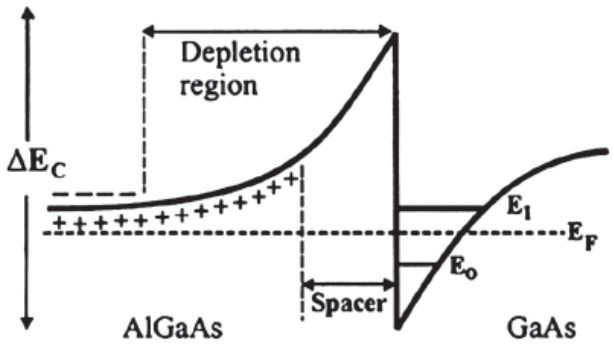

Fig. 1.3: Schematics of the conduction band at the interface between individual layers of n-AlGaAs/GaAs heterojunction.

A solution for the energy levels in a triangular potential well can be found elsewhere (i.e. ref. [**8**]). Here we would only like to stress that as the quantum well broadens, distance between energy levels decreases for higher levels.

As was already mentioned above, the 2DEG/2DHG is of special importance for electronics, especially due to the possibility to control the carrier density by external voltage (gating). However, not only carrier density but also their spin can be manipulated by gating of 2DEG/2DHG, if spin-orbit coupling is taken into account.

1.3 Spin-orbit coupling in GaAs based structures

In systems without inversion symmetry, such as the zinc-blende GaAs and derived structures, the relativistic effect of spin-orbit coupling causes spin splitting of energy bands. Beyond Γ point, the splitting occurs not only in the valence band, but also in the conduction band. The crystal

field of the SC then acts as an effective magnetic field ***B(k)*** on itinerant electrons with wave vector ***k*** and energy corresponding to the CB**.** The resulting term of the Hamiltonian is then obtained in the following form [7]:

$$H_{SO}(\mathbf{k}) = \frac{1}{2} g\mu_B \mathbf{B}(\mathbf{k}) \cdot \sigma \tag{1.1}$$

where g denotes the g-factor, μ_B stands for the Bohr magneton, and σ is the Pauli spin matrix. The effective magnetic field ***B(k)*** is strongly anisotropic, and its form depends on the material symmetry. In the case of bulk zinc-blende GaAs with *bulk inversion asymmetry (BIA),* SO coupling gives rise to the *Dresselhaus term* in the Hamiltonian:

$$H_{Dress} = \frac{\hbar}{4m^2c^2} \nabla V(\mathbf{r}) \times \mathbf{p} \cdot \sigma \tag{1.2}$$

here m marks the effective mass and ***p*** is the momentum operator. ***V(r)*** denotes the crystal potential, that in combination with SO coupling causes the magnetic field ***B(r)*** to occur [14].

In addition to BIA, the symmetry can be broken also when an additional electric field is present in the material, which causes *structure inversion asymmetry (SIA).* This in turn leads to the *Rashba SO term*:

$$H_{Rashba} = \alpha(\mathbf{r}) \times \mathbf{p} \cdot \sigma \tag{1.3}$$

The parameter *α(**r**)* relates to the additional electric potential, which can be either inherent to the system (internal electric fields in low dimensional structures, heterostructures etc.) or it can be added as an external field. As such, Rashba SO field can be tuned by structure engineering, or dynamically by gating, while the Dresselhaus field remains constant. By these means it is possible to manipulate electron spins electrically, which is the basic working principle of spin transistors and other components. On the other hand, strong SO interaction results in rapid loss of spin polarization (i.e., loss of information in spintronic devices). As the electrons injected to the system sense the SO field ***B(k)***, they start to precess, and the precession depends on their ***k*** vectors. Scattering in k-space then leads to spin relaxation, known as *D'Yakonov – Perel mechanism* [15]. This relaxation channel often dominates in quantum wells [15], but it can be strongly suppressed by tuning the SO Rashba field (see **Chap. 4.**). It is known that under certain conditions in can be dominant also in bulk GaAs [14].

Besides the important role that SO coupling plays in spin relaxation, its presence enables also efficient optical generation of spin polarization in SCs via *optical orientation* discussed in the following section, which forms the basis of the experimental methods used in this work.

1.4 Optical properties of GaAs based structures

1.4.1 Optical transitions and optical orientation

Rate of light absorption is generally given by dipole matrix elements. Selection rules that determine the values of the elements can be different for various polarization states of the incident light. The simplest understanding of the problem is through the momentum formalism, in analogy to transitions in atoms. The allowed optical transitions can be determined from the conservation of total angular momentum. Circularly polarized light carries an angular momentum of *J = 1*, with

projections to the main quantization axis $J_z = \pm 1$. The only transitions allowed in the system are those with $\Delta J = \pm 1$, and their probability is given by the square of the transition matrix elements in dipole approximation $\left|\left\langle \Psi_f \left| \vec{e} \cdot \hat{p} \right| \Psi_i \right\rangle\right|^2$, where Ψ_i and Ψ_f denote initial and final states, $\boldsymbol{p}$ is the dipole operator and e corresponds to the polarization vector of the incident light. The selection rules are illustrated in Fig. 1.4 a). Relative probabilities of these transitions (see also [**16**]) are indicated for the absorption of left (σ^+) and right (σ^-) handed circularly polarized (CP) light in bulk GaAs at the G point.

Let us now have a closer look at what happens if the wavelength of incident light is tuned to match the energy difference between the LH/HH valence band and the conduction band. We define spin polarization as:

$$P = \frac{n_\downarrow - n_\uparrow}{n_\downarrow + n_\uparrow} \tag{1.4}$$

where $n_\uparrow$ indicates number of carriers with spin projection along the quantization axis, while $n_\downarrow$ is number of carriers with opposite projection. Absorption of CP light in bulk GaAs then leads to net spin polarization of photoexcited carriers up to $P = 50\%$ [see Fig. 1.4 b)]. The situation becomes different if the symmetry of bulk zinc-blende structure is broken and the degeneracy of HH/LH bands is lifted [Fig. 1.5 c)]. Various effects can lead to symmetry breaking in bulk GaAs, e. g., application of strain (Fig. 1.2) or quantum confinement (8). In such case, it is possible to obtain very high net spin polarization ($P = 100\,\%$ in principle) if the carriers are excited entirely from the HH band.

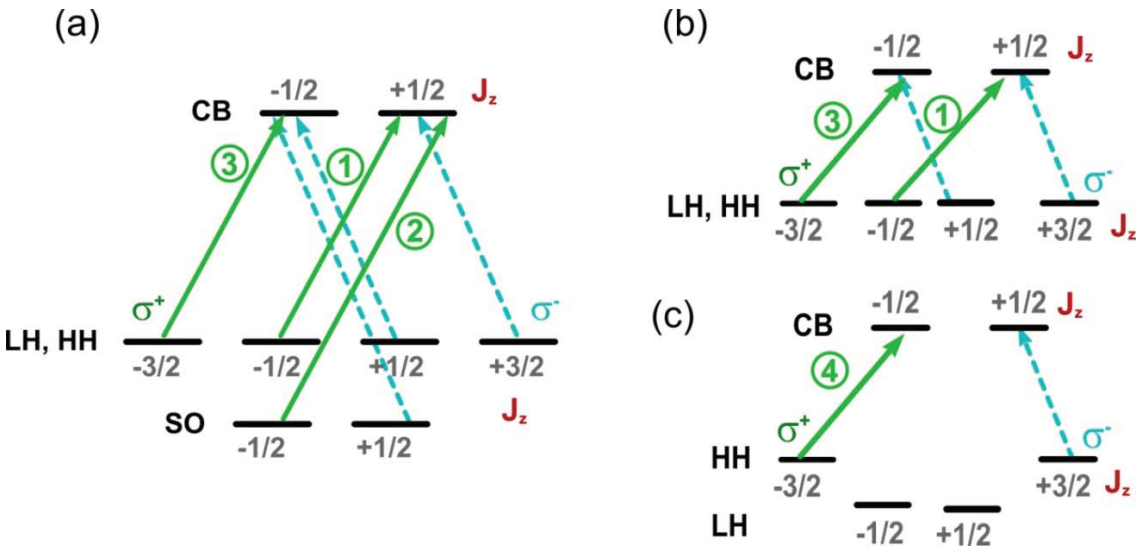

Fig. 1.4: a) Selection rules for absorption of left (σ^+) and right (σ^-) handed circularly polarized (CP) light in zinc-blende GaAs. CB denotes the conduction band, LH (HH) light (heavy) holes bands. Numbers corresponding to each band indicate the projection of total angular momentum to the direction of quantization J_z, while the numbers near each transition depicted as an arrow describe the absorption probability. Absorption of CP light from HH, LH bands to CB b) in bulk GaAs and c) after lifting of valence band degeneracy.

From a macroscopic point of view, spin polarization of photoinjected carriers behaves as an effective magnetic field, even in non-magnetic materials like GaAs. Internal magnetic field can

also be a result of ferromagnetic order, e. g., in magnetic semiconductors (see **Chap. 3**). As a result, the material can display magnetooptical effects.

1.4.2 Magnetooptical effects

The family of magnetooptical effects includes a large number of phenomena connected with the interaction of polarized light with a magnetized medium. Each state of polarized light can be decomposed into an orthogonal basis formed either by two perpendicular linear polarizations (*s*, *p*) or by two circular polarization of opposite helicities (σ^+, σ^-). MO interactions result in different complex indices of refraction $\hat{N}$ for the two orthogonal base polarizations. The polarization-dependent real part of complex $\hat{N}$ is responsible for *birefringence*, whereas the imaginary part – absorption – is related to *dichroism.* The MO effects then result either in rotation of the polarization plane or in changes of ellipticity [**17**].

For our experimental work, which was always performed under nearly normal incidence, and in which the rotation of a linearly polarized probe beam was usually detected, two effects are of significant importance – *magnetic linear dichroism* and *magnetic circular birefringence (*commonly known as *polar Kerr effect)*. Let us now briefly describe both of these effects. Special attention will be paid to these in **chapter 3** where they will be discussed in context of our signal analysis.

Polar Kerr effect (*PKE)* is based on different values of the index of refraction for circularly polarized light of opposite helicities, which induces phase shift between these orthogonal base components. This in turn leads to the rotation of the linear polarization plane of the light, see Fig. 2.3 (a). If we assume normal incidence geometry (i.e., the plane of incidence is perpendicular to the sample plane), PKE occurs in the material where the *incident beam is parallel with the magnetic field* causing the MO effect. *PKE* is thus connected with the presence of the *out-of-plane* component of magnetization. It is one of the well known effects and it often dominates the MO behavior of many materials (e. g., some metals, permalloys, etc.). Additional contributions to the internal magnetic field can result also from photoinjected spins due to the optical orientation. The spins of such carriers are aligned in the direction of beam incidence, which usually means perpendicular to the sample plane – see ref. [**14**]. *PKE* is therefore important also for the detection of spin dynamics in non-magnetic semiconductors.

Magnetic linear dichroism *(MLD)* is detected if the *light propagates perpendicularly to the direction of the magnetic field*, if we again assume normal incidence of light. It is a second-order MO effect resulting from different absorption (reflectivity) coefficients for the two linear polarizations [**17**]. In this case the basis is given by the linear polarizations parallel (*p*) and perpendicular (*s*) to the magnetization in the sample plane. This effect again leads to the rotation of the polarization plane – see Fig. 1.5 (b). Even though MLD is negligibly small in the majority of materials compared to first order MO effects [**17**] in diluted magnetic semiconductors, and especially in (Ga,Mn)As, it can be quite larg [**18**]. In a certain spectral range, it can even exceed the polar Kerr effect.

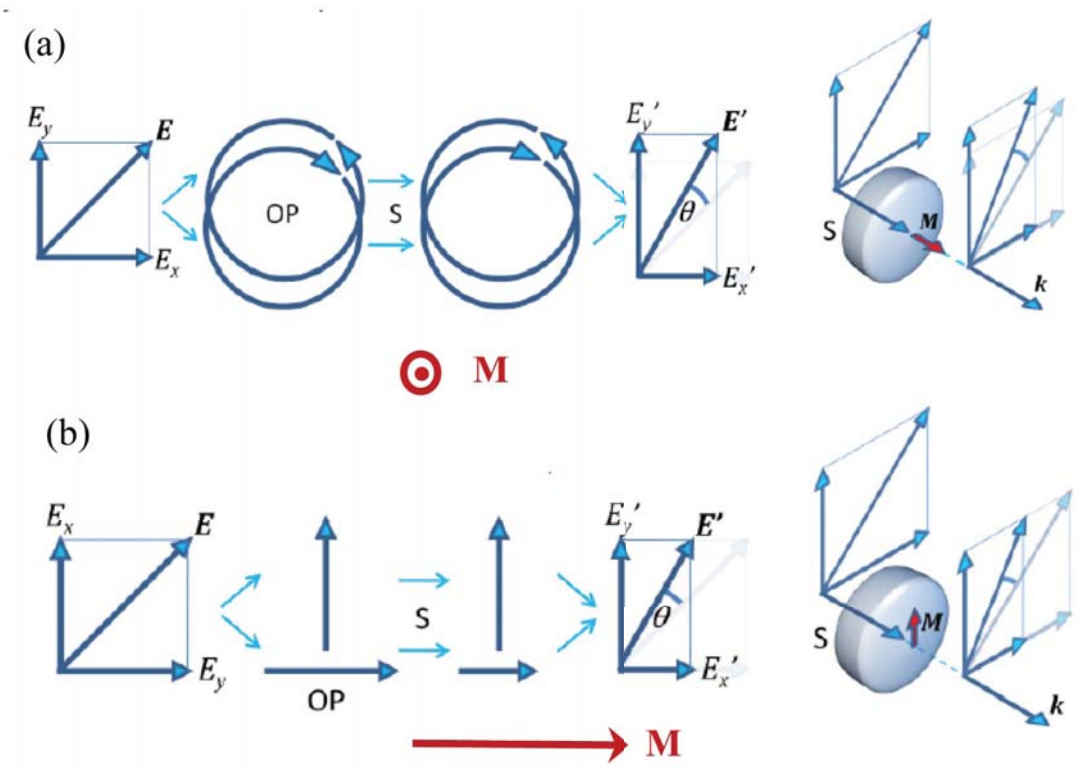

Fig. 1.5.: Schematic illustration of (a) polar Kerr effect and (b) magnetic linear dichroism. Here **M** represents the direction of magnetization relative to the sample plane **S**, while **k** stands for the wave vector of the incident light. E_x, E_y represent the individual projections of the electric field vector **E** into orthogonal polarization components (OP). After reflection from the sample plane, the electric field vector is rotated by the angle **q** and becomes **E'** (components E_x' and E_y'). Taken from [**19**].

The microscopic origin of these MO effects lies generally in the spin-splitting of valence/conduction bands, different filling of the bands with different spin polarization (for example after optical excitation), or a combination of these effects. Therefore, measurement of MO spectra, where these effects are traced at different energies, can also provide useful information about the exact band structure of the material and about the nature of its ferromagnetic order [**20**].

2. EXPERIMENTAL METHODS FOR SPIN DYNAMICS MEASUREMENT

In this chapter, an overview of experimental methods used for the measurement of spin dynamics in GaAs related structures will be given. Even though the final detection varies significantly among the individual experimental techniques, optical orientation still remains the most efficient way for injection of spin polarized carriers, as described in the previous chapter [**16**].

2.1 Ultrafast laser spectroscopy

Ultrafast laser spectroscopy, namely *pump and probe* techniques, turned out to be very convenient for measuring ultrafast carrier and spin dynamics in various types of materials [**21**]. The unique time resolution of these methods, which goes down to ~ 100 fs, enables us to study the relevant processes directly in time domain. A possibility of spatial resolution represents another important advantage compared to standard electrical measurements.

The basic working principle of all the pump and probe experiments is similar. A non-equilibrium carrier population is excited by above-bandgap absorption of laser light. If circularly polarized light is used, the resulting population will be spin polarized.

The photo-injected carrier population triggers changes in the system. These changes are visualized using the second time-delayed probe beam [Fig. 2.1 a)]. It is the detection that determines what phenomenon can be studied – ranging from time evolution of luminescence in up-conversion to spin dynamics in the Kerr rotation method. In this work we used two pump-probe techniques – *time resolved transient reflectivity (TRR)* and *time-resolved magnetooptics (TRMO)*. Both of them were performed in reflection geometry due to the nature of samples grown on thick non-transparent substrates. Furthermore, under certain conditions (**see Chap. 3.6**), the second pump pulse can be used to coherently control changes triggered by the first pump pulse. In such case, double-pump modification to the setup is needed [Fig. 2.1 b)], where a time delay is independently varied also between the two pump pulses.

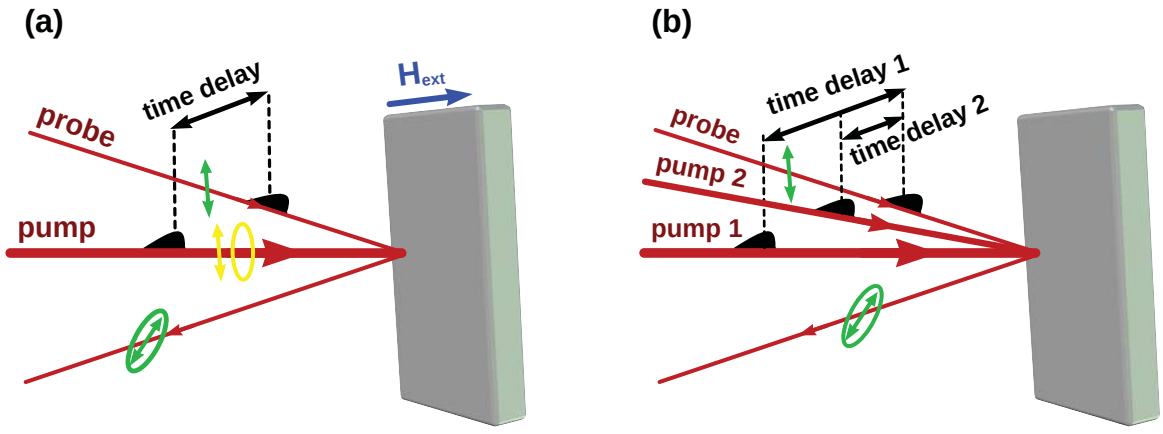

Fig.2.1: Schematic depiction of a) standard pump and probe method and b) double-pump method in reflection geometry. Here H_{ext} denotes the external magnetic field applied in the sample plane during most of the experiments.

2.1.1 Time-Resolved Transient Reflectivity Method

Time-resolved transient reflectivity (TRR), or its modification in transmission geometry (TRA), is one of the most commonly used methods of ultrafast laser spectroscopy. It is based on the modification of the refraction index (or absorption coefficient in TRA) due to the absorption of the strong pump pulse, resulting in generation of electron/hole pairs. This manifests as a change of the sample reflectivity, which subsequently influences the detected probe beam intensity. Reflectivity, as a function of the time delay between pump and probe pulses, follows non-equilibrium carrier population dynamics. The dominant part of the signal in semiconductors comes from the photo-injected electrons while the holes can usually be neglected [**14**].

The dynamics is characterized by the *lifetime* τ_r of the electrons in the conduction band. In the simplest case of exponential population decay, the transient change of reflectivity due to the pump pulse [ΔR(t)] is connected with τ_r through the following expression [**22**]

$$\frac{\Delta R(t)}{R_0} \propto n_0 \exp\left(-\frac{t}{\tau_r}\right) \tag{2.1}$$

where R_0 indicates the static reflectivity of the sample, and *n0* the total number of the photoexcited electrons.

From the microscopic point of view there can be many reasons for changes in the refraction index. Photoexcited carriers can lead to band filling, many-body effects, or the absorption on free carriers can occur [**23**]. All of these affect the absorption of the material differently, depending on the excitation intensity and wavelength [**24**]. The index of refraction is then connected with absorption by Kramers-Kronig relations. Unfortunately, it means that the absorption at one wavelength modifies refraction index in the whole spectral range, which makes analysis of the signal detected in reflection geometry rather complicated, especially with regard to spectrally-resolved measurements. Despite these problems, the TRR method can provide very important information about electron dynamics in the materials.

2.1.2 Time-Resolved Magnetooptics

For the study of fast dynamics of magnetization of carrier spins, many methods have so far been proposed, mostly based on the use of magnetooptical (MO) effects for detection [**25**]. The basic principle of pump-probe (P&P) methods remains the same – strong pump pulse induces changes that are seen as a variation of ellipticity or polarization plane rotation of the probe beam, resulting from the MO effects that occur in magnetized materials – see Fig. 2.1(a).

Time resolved magnetooptics (TRMO) is not bound only to the presence of photoexcited carriers, unlike the above described TRR and related techniques. As a result, it is possible to track the changes in internal magnetization of magnetic media as well as spin polarization of photoexcited carriers [**21**]. The TRMO technique has been extensively used in various materials for studying the magnetization and carrier spin dynamics [**26**]–[**30**]. However, in these materials there is no direct link between the photoexcited carriers themselves and the change of magnetization. The situation is different in diluted magnetic semiconductors (see **Chap. 3**) with carrier mediated ferromagnetism, where changes of carrier concentration can significantly influence the magnetic order [**21**], [**31**]–[**33**]. Therefore it is convenient to combine the carrier and magnetization dynamics measurement in one experiment.

2.1.3 Setup and experimental details

The time-resolved optical measurements were done in standard pump-probe setup. Pulse titan-sapphire laser (Spectra Physics, Tsunami 3960) was used to generate ~100fs long laser pulses with a repetition rate of 82 MHz. The laser system can be spectrally tuned in the range of 720-1050 nm which is suitable for measurements in GaAs with the band gap in the infrared region (870 nm at room temperature).

The experimental setup common for both of the above described methods is depicted in Fig. 2.2. The laser pulses are divided into two separate arms by a beam splitter. The probe pulse is time-delayed with respect to the pump one by a computer-controlled delay line. The pump and probe beams are synchronized at the time they reach the sample by careful setting of the optical paths in both arms they pass. Polarization state of the light in both arms is controlled by λ/2 and λ/4 waveplates and it can be set to either circular or linear. Both beams are then focused in nearly normal incidence geometry on the sample. For low-temperature measurements, the sample is glued to a cold-finger of a closed-cycle cryostat, which in principle enables cooling down to 8 K. However, due to the imperfect thermal contact of the sample with cold finger, the lowest surface temperature is 15 K in the case of simple (Ga,Mn)As/GaAs layers, and it reaches above 35 K for hybrid structures with piezo stressors. The head of the cryostat is located between pole extensions of an electromagnet, where a magnetic field up to ~ 0.7 T can be applied.

The probe beam reflected from the sample is further focused to the optical bridge. Basic principle of this system is simple – linear polarization is divided by a polarizer into *s*- and *p*- base polarization, each of which is deflected to different arms of the bridge, where they are detected separately by silicon detectors. The signals from the detectors are transferred to differential preamplifiers that allow extracting sum and difference of the individual input signals. The output of these preamplifiers is transferred to Standford SR830 lock-in amplifiers that are phase-matched to the reference signal of an optical chopper placed in the path of the pump beam. Therefore, the resulting signal detected by the lock-in amplifier is sensitive only to the changes of the reflected probe pulse induced by the pump [14].

By measuring the sum of the intensity detected in both arms of the bridge we gain access to information about the reflectivity dynamics through the following expression:

$$\frac{\Delta R(t)}{R_0} \approx \frac{\Delta I_p(t) + \Delta I_s(t)}{I_p^{off} + I_s^{off}} \tag{2.3}$$

Here $\Delta R(t)$ is pump-induced reflectivity change as a function of time delay between pump and probe pulses and R_0 indicates static reflectivity of the sample. $\Delta I_s(t)$ [$\Delta I_p(t)$] are corresponding changes of intensities in the *s*- (*p*-) arms of the bridge and I_s^{off} (I_p^{off}) indicate static intensities (i.e., without the pump pulse).

The difference in the detected intensity of the s- and p- polarization, normalized to the total reflected intensity, directly relates to the rotation of the polarization plane as follows [22]:

$$\Delta\theta(t) \approx \frac{\Delta I_p(t) - \Delta I_s(t)}{2\left(I_p^{off} + I_s^{off}\right)} \tag{2.4}$$

where $\Delta\theta(t)$ represents the rotation of polarization plane as a function of time delay t between pump and probe pulses. This equation remains valid only if the pump-induced change of the

reflectivity can be neglected. For the derivation of the above expressions, as well as for a more detailed description of the optical bridge system, see [22].

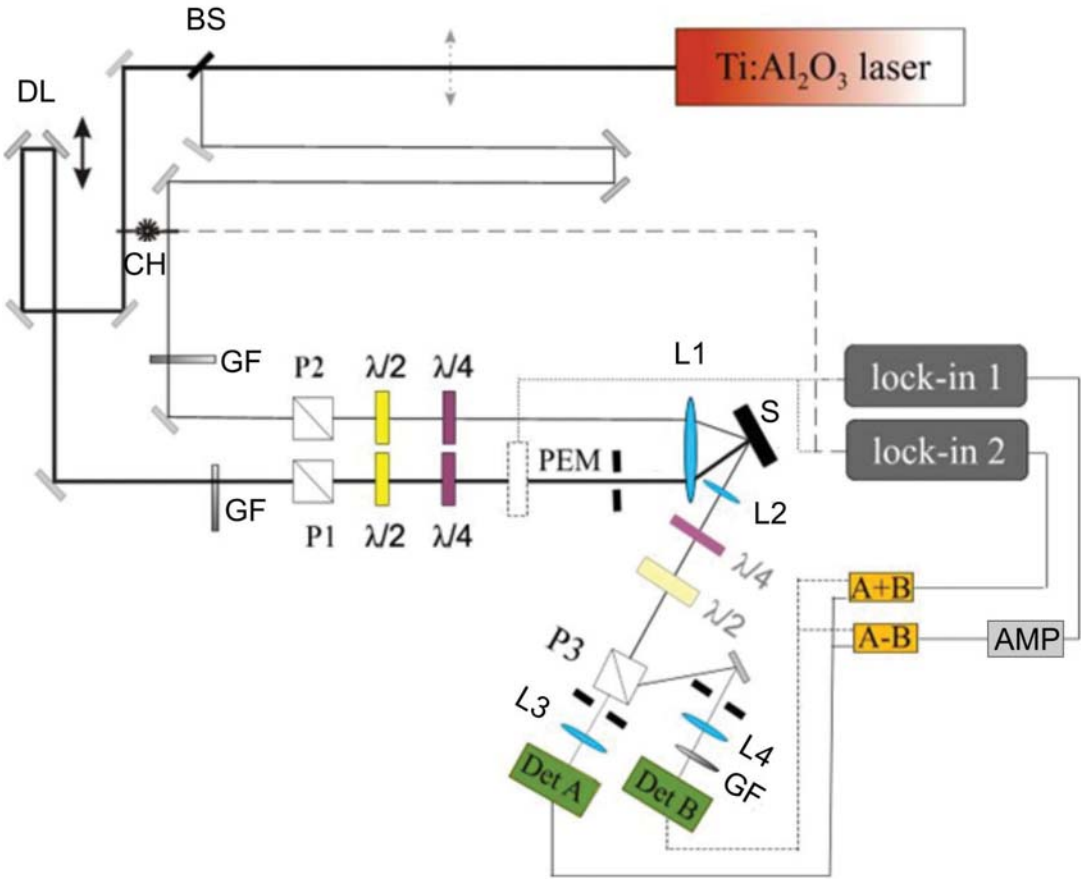

Fig. 2.2.: Experimental setup for TRR and TRMO methods. Meaning of the abbreviations is as follows: BS – beam splitter, DL – delay line; CH – chopper; GF – adjustable grey filters; P1, P2, P3 – polarizer; L1-L4 – lenses; λ/2 and λ/4 – waveplates; det A (B) – silicon detectors; A+B, A-B – differential preamplifiers, AMP – commercial preamplifier, lock-in 1,2 – phase sensitive (lock-in) amplifiers.

2.2 Electro-optical Hall measurements

Various methods have so far been proposed for detection of spin transport related phenomena in non-magnetic semiconductors. Many of them use electrical injection of spin polarized carriers through ferromagnetic contacts, and a detection based on standard experimental techniques – either optical, such as Kerr imaging [34]–[36] and circularly - polarized electroluminescence [37]–[38] etc., or magneto – electrical by using the spin valve effect, spin-orbit coupling etc. [39]–[41]. However, all these methods have to deal with serious experimental issues. Electrical injection requires hybrid ferromagnet/semiconductor design that cannot be easily fabricated. On the other hand, optical detection lacks nanoscale resolution and it also too complicated for massive use. Therefore, it is convenient to go beyond standard techniques, and use such a combination of injection and detection that is suited for the given material and device. In our case, this means optical orientation of the carriers and purely electrical, local detection of spin polarized carriers. As more details on structures studied in this thesis will be given in **Chap. 4**, in this section we only briefly introduce the working principles of this method.

2.2.1 Basic principle

The combined electro-optical measurement relies on the characteristics of the planar photovoltaic cell investigated in Ref. [**42**]. The device itself consists of 2 dimensional electron gas (2DEG), on top of which the 2 dimensional hole gas (2DHG) layer is grown. Both of these nanostructures are formed by doping of AlGaAs/GaAs quantum wells and beneath the P-doped part the 2DEG is usually depleted. The upper part of the multilayer is etched away in a certain region so that a narrow lateral PN junction is formed between the 2DEG/2DHG (see Fig. 2.3). Note that depending on the fabrication procedure, in certain cases the 2DEG is not fully depleted in the unetched part, and therefore a planar PN junction stretches under the whole P-region [**43**]. The multilayer is further lithographically nanopatterned to form a device with several 10 nm wide Hall bars (HBs). For more details on the structure see **Chap. 4.2.1**.

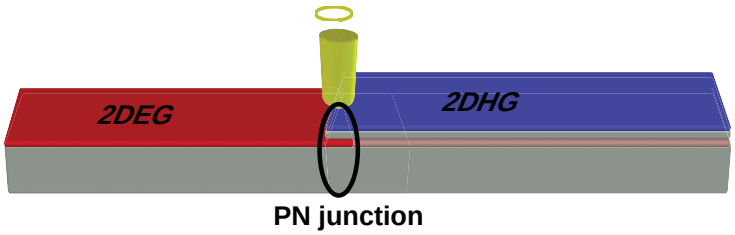

Fig. 2.3: Schematic drawing of 2DEG/2DHG planar photodiode

The method itself then takes advantage of the photodiode characteristics of the device. At small reverse bias applied along the narrow channel in darkness, the device is not conductive. If the PN junction is irradiated by light with wavelengths below the bandgap of bulk GaAs, carriers are generated by the transitions from the 2DHG quantum well (QW) to 3D electron states. Stark effect in the QW leads to spin-splitting of heavy hole/light hole states (see **Chap. 1.4.1**) and the absorption of CP light therefore leads to a very high degree of spin polarization of the photoexcited carriers via optical orientation. In the reverse-biased device, the optically generated electrons propagate into the N-region (holes to P-side). As a result of SO coupling in the channel, different types of Hall effects can occur (see **Chap. 4.1.1**) and spin polarized carriers are deflected to the HBs. By detecting transverse voltage between the pairs of opposite HBs [**42**] together with the total photocurrent flowing along the channel, we can deduce Hall resistivity. Hence information about local spin orientation between the given contacts can be inferred. Spatial resolution along the channel can be achieved by using several pairs of contacts in a row.

2.2.2 Experimental setup

The electro-optical Hall measurement was performed in the following setup. Tunable CW titan-sapphire laser was used to generate monochromatic light in the spectral range 820-860 nm, which is below the band gap of GaAs. The beam was chopped at a low frequency (150 Hz) by a mechanical chopper, and its intensity was measured by an Si detector and lock-in amplifier. Linear polarization of the beam is set by a combination of polarizer and $\lambda/2$ waveplate to be oriented 45° with respect to the axis of a photoelastic modulator (PEM). The PEM allows modulating of polarization at the frequency of 50 kHz. Depending on the mode used, the polarization can be changed between two helicities of circular polarization, or between two perpendicular linear polarizations. After passing through the PEM, the beam is focused on the PN junction of the device by a microscope objective Mitutoyo M plan NIR 100x, mounted

on high-precision XYZ piezo-electric stage. The stage can be computer driven which enables to precisely shift the beam spot across the device. Furthermore, additional beam splitters in combination with an objective and CCD camera provide a possibility to directly observe the device and align the laser spot with respect to the PN junction. The device itself is placed in a low-vibration continuous flow cryostat with adjustable measurement temperature ranging from less than 4K up to room temperature.

The total photocurrent (I_{PH}) flowing through the channel is measured using the SR570 current preamplifier, connected to a lock-in amplifier with reference frequency from the chopper. The light intensity is always set so that the photocurrent does not exceed 1μA (typically 0.5-1 μA). Voltage between the two opposite HBs (U_H) is detected by a combination of high-impedance preamplifiers (SR560) and lock-in amplifiers with reference frequency taken from the PEM. Signal from the three successive HBs located in the 2DEG region is typically recorded simultaneously. Furthermore, longitudinal voltage drops (U_L) between two adjacent Hall probes are monitored by the same technique.

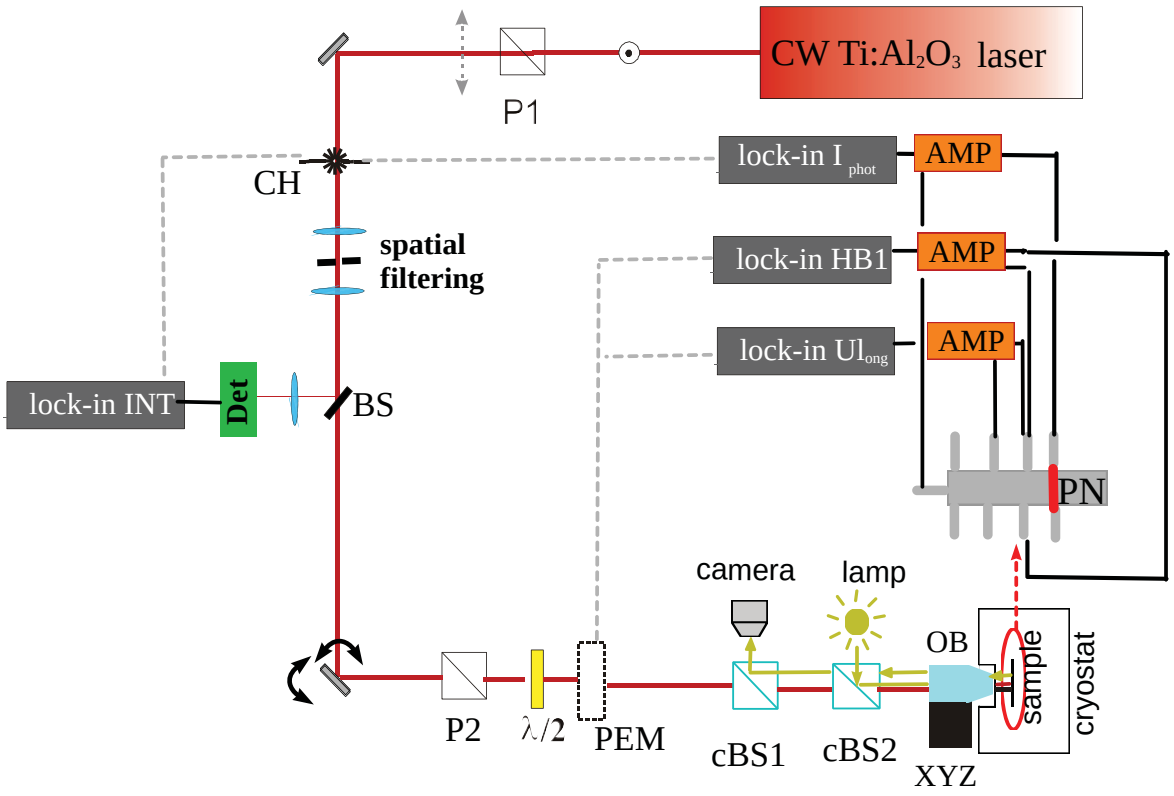

Fig. 2.4: Experimental setup for electro-optical Hall measurement. A meaning of the abbreviations is as follows: CH – chopper, BS – beam splitter; Det – silicon detector P1,P2 – polarizers; λ/2 – waveplate; PEM – photoelastic modulator, cBS1, cBS2 – non-polarizing cube BS, OB – objective 100x, XYZ – piezo-electric stage, AMP – preamplifiers

The relevant quantities for the detection of spin accumulation by Hall effects are *Hall resistance* and *Hall angle*. Hall resistance is connected to the measured U_H and I_{PH} in a straightforward way:

$$R_H = \frac{U_H}{I_{ph}} \tag{2.5}$$

The Hall angle takes also longitudinal resistance $R_L = U_L/I_{PH}$ in account, and is defined as:

$$\alpha_H = \frac{R_H}{R_L} \tag{2.6}$$

Hall angle can be understood as an angle between electric field generated in the device after biasing, and the effective internal field, connected with SO coupling, which causes the electrons to deflect to sides [15]. More of the physics of Hall effects will be described in **Chap. 4.1.1.**

3. MAGNETIC SEMICONDUCTORS

The magnetism in semiconductors (SC) has been studied extensively since 1960s. The first materials of interest were magnetic chalcogenides [**44**] and semiconducting spinels [**45**]. However, they turned out to be much too complicated both in terms of fabrication and in compatibility with standard electronics that uses mainly silicon or gallium arsenide. In early 1990s, the research shifted towards the diluted magnetic semiconductors (DMS), artificial structures where a certain percentage of atoms in the standard SC lattice is replaced by the magnetic ions (typically Mn). Natural materials of choice for such structures are II-VI SCs like CdTe or ZnSe, where the matching of valence between the host material and the common magnetic ions allows relatively easy preparation by equilibrium methods [**6**], [**46**]. By the equilibrium growth procedure it was possible to incorporate significant amounts of magnetic ions [up to 77% of Mn in the case of (Cd,Mn)Te]. However, the magnetic interactions in such high-doped materials were dominated by a direct antiferromagnetic exchange among Mn atoms, and the ferromagnetic order was achieved only at very low temperatures (< 2 K) in heterostructures [**47**]. But even there, the first signs of the ferromagnetic order mediated by the itinerant carriers have already appeared, which is a very important property of the DMSs. This kind of ferromagnetic order was observed also in IV-VI based DMS ternary alloys [**48**] but the most straightforward path to follow was using the common III-V SCs (such as GaAs, InAs…) [**49**] that were easily achieved in high quality and the resulting DMS would match the standard electronics. The major obstacle that prevented from the fabrication of the III-V DMS was a low solubility of the magnetic ions in the host material. It has been overcome by using the non-equilibrium low temperature molecular beam epitaxy (LT-MBE) which allowed the incorporation of several percent of Mn directly to the host lattice and fabricating the first ferromagnetic (In,Mn)As sample [**50**]. Several years later, the first DMS based on GaAs, the most explored member of the III-V family, was prepared, giving rise to (Ga,Mn)As alloy [**51**]–[**53**]. Since then the (Ga,Mn)As has remained the main material of interest that has been investigated by various magnetic, transport and optical methods.

Despite all its promising properties, the problem still remains in the low ferromagnetic transition temperature in (Ga,Mn)As. Therefore, parallel branch in the magnetic semiconductor research has developed which deals with diluted magnetic oxides (DMO) and nitrides (DMN). It has been predicted theoretically that these structures should exhibit ferromagnetism even at room temperature (RT) and higher [**54**]. Unfortunately, none of the DMN or DMO alloys, where the theoretical conditions for carrier mediated RT ferromagnetism are met, has been so far synthesized [**6**], [**55**].

3.1 Magnetic semiconductor (Ga,Mn)As

As was already mentioned, (Ga,Mn)As has kept the main interest in the field of DMS for the last decade. It is based on GaAs, whose band structure and overall properties are very well known. Even though the practical use of this material might be limited by a low critical ferromagnetic temperature [**6**], [**55**] which currently reaches $T_c = 185\ K$ [**56**], (Ga,Mn)As still remains a crucial model material for the study of the fundamental interactions in all the magnetic semiconductors. In this chapter we would like to briefly describe the properties of (Ga,Mn)As, with a special emphasis on magnetic ordering.

3.1.1 Structure and properties of (Ga,Mn)As

The (Ga,Mn)As structure is derived from GaAs which is doped with magnetic manganese atoms. In order to achieve the ferromagnetic order only a few percent of the dopant are needed. Therefore, the resulting (Ga,Mn)As layers keep the zinc-blende structure and overall character of the host material, the Mn atoms acting only as a perturbation to the structure. Some of the optical properties, such as the above band-gap absorption or the index of refraction, are believed to be only little affected by the presence of magnetic impurities [**57**]. From this point of view, the material is very similar to a low-temperature grown GaAs. On the other hand, several issues concerning mainly the position of Fermi level and formation of impurity band remain unresolved ([**20**], [**58**] and references therein). From the optical point of view the biggest difference between GaAs and (Ga,Mn)As is in the ferromagnetic order of the latter one and subsequent strong magnetooptical activity.

The Mn impurities incorporated into the host zinc-blende lattice can occupy various positions (see Fig. 3.1). Energetically the most favourable position is the one where Mn substitutes Ga atoms (Mn_{Ga}) due to the similar atomic structures of Ga ($3d^{10}4s^2p^1$) and Mn ($3d^54s^2$) [**59**]. The Mn-As bonding is formed by the two 4s electrons of Mn in the same way as it was in the case of Ga-As, but with the one p^1 electron missing. This results in the acceptor character of Mn_{Ga} impurity. The weakly bound hole occupies one of the antibonding states [**59**]. Furthermore, the localized d-electrons of Mn with total spin S = 5/2 (g-factor of 2) and zero orbital momentum cause that Mn_{Ga} defects act as localized magnetic moments. Itinerant holes and localized spins, both crucial for the ferromagnetic order to be established in the material, are therefore provided by Mn_{Ga} impurities.

Besides the most common Mn_{Ga} position, other defects are formed during the growth [**60**]. The Mn atoms can occupy the interstitial positions (Mn_I) and As atoms can also replace Ga as the antisites (As_{Ga}) – see Fig. 3.1. The percentage of these defects increases for higher doped samples where as much as 20% of Mn can occur as interstitials unless some post-growth treatment is implemented. Both these impurities act as double donors [**59**] and have compensating effects on the holes provided by $Mn_{Ga.}$ Furthermore, the interstitials also couple antiferromagnetically to Mn_{Ga} and the total spin of such complexes is smaller than S = 5/2 [**59**]. It means that also the total magnetic moment is compensated by the "additional" impurities, which affects strongly the ferromagnetic order.

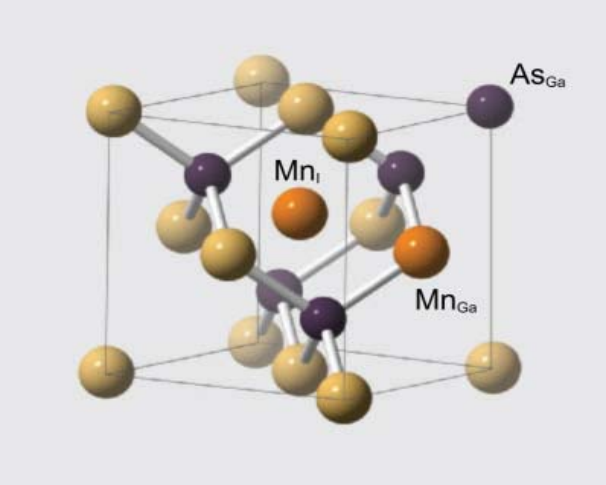

Fig. 3.1: The lattice structure of (Ga,Mn) As. Zinc-blende lattice of the host GaAs is influenced by manganese dopants and other deffects. The As_{Ga} stands for the arsenic antisite, Mn_{Ga} gallium substitution atom and Mn_I manganese interstitial [55]

3.1.2 Magnetic interactions

The ferromagnetic (FM) order in (Ga,Mn)As is mediated by the itinerant holes provided by the manganese, which is the key property that allows for the ferromagnetism to be controlled by external means. The Zener kinetic exchange is a generally accepted model describing the magnetism in this material [54] – [55], [59], [61]. In this description the randomly distributed Mn ions are treated as localized spins with S = 5/2. The weakly bound holes on the top of the valence band that is formed dominantly by the 4p-levels of As atoms strongly hybridize with the d-states of the Mn_{Ga} atoms which results in spin-splitting of the valence band and subsequent antiferromagnetic (AF) coupling between the holes and the localized spins. If treated in the mean field approach, this AF interaction can be described by a single exchange parameter J_{pd}. The itinerant spin polarized holes transfer the magnetic moment further into the lattice, causing the long-range FM order, as schematically depicted in Fig. 3.2. For further details on the theoretical description see ref. [59].

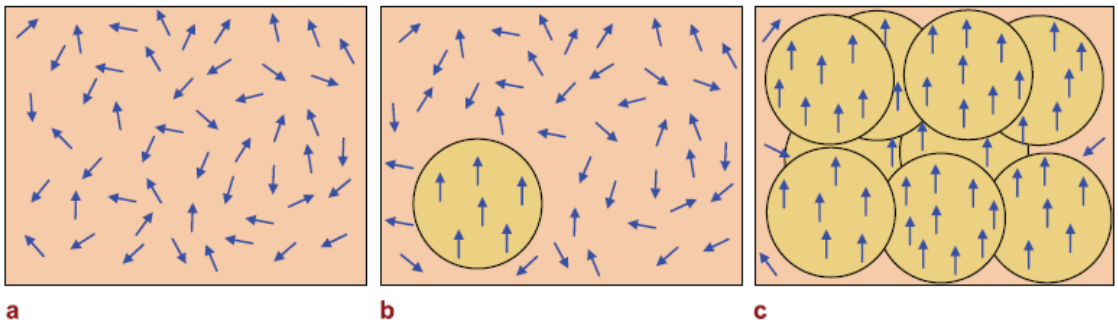

Fig. 3.2: Schematic depiction of the long-range ferromagnetic order. At low hole concentration (a) the spin are randomly distributed. The local spin alignment of Mn spins (b) occurs by doping and for high enough concentration of delocalized holes the long-range ferromagnetic order is transmitted to whole crystal (c). [55]

The overall strength of the magnetic order, and thus also the FM critical temperature (Curie temperature T_C), is given not only by the J_{pd} constant but also by the number of the localized spins and the hole concentration. In the mean field approximation, a simple relation that connects T_C to these parameters can be derived [54]:

$$k_B T_C = \frac{N_{Mn}\, s(s+1)}{3} J_{pd}^2\, x_F \qquad (3.1)$$

Here N_{Mn} indicates the number of the Mn_{Ga} atoms, S their spin moment, χ_F spin susceptibility and k_B denotes the Bolzman constant. Both the parameters N_{Mn} and S are not necessarily proportional to the level of Mn doping due to the presence of compensating defects Mn_I and As_{Ga} arising during the growth. The number of these defects can be decreased by optimizing the growth procedure and post-growth treatment. From Eq. 3.1 it thus follows that for a given nominal doping x of the (Ga,Mn)As layer the value of T_c is a good indicator of the sample quality (i.e., it reflects a number of the Mn_{Ga} atoms compared to the amount of the "unwanted" impurities).

3.1.3 Magnetic anisotropy and free energy functional [62]

The ferromagnetic order in (Ga,Mn)As has a striking feature of the relatively complex and strong magnetic anisotropy (MA). The MA is dependence of the energy of the system, which is described by a total *free energy functional F*, on the crystallographic direction. Under

the equilibrium conditions, the directions where the energy reaches its minima/maxima are usually denoted as "*easy/hard axis of magnetization*". At equilibrium conditions, the macroscopic magnetization vector is aligned in the direction that minimizes the total energy – *easy axis*. In the case of (Ga,Mn)As the MA occurs due to the fact that the ferromagnetic order is mediated by the holes in valence band that are strongly spin orbit coupled [**4**]. It also means that the magnetic order will reflect the symmetry of the valence band and all its distortions. Let us now summarize the individual contributions to the total free energy of the (Ga,Mn)As layer.

A. Intrinsic anisotropies in (Ga,Mn)As epilayers

Magneto-crystalline anisotropy

In an undistorted bulk crystal, the hole-mediated ferromagnetism leads to the presence of *cubic magnetocrystalline* anisotropy which reflects the zinc-blende cubic symmetry of the host lattice. Its contribution to the free energy has a following phenomenological form (see [**62**], Eq. 12):

$$F_{cryst}\left(\hat{M}\right) = K_{c1}\left(n_x^2 n_y^2 + n_x^2 n_z^2 + n_z^2 n_y^2\right) \qquad (3.2)$$

Here, $\hat{M}$ represents a magnetization unit vector with the individual components n_x, n_y and n_z (as defined later – Fig. 3.4). K_{c1} stands for the first order cubic anisotropy constant. Note that the higher order magnetocrystalline contributions are usually small compared to the K_{c1} [**62**] and in further discussion, we will use just K_c for the cubic anisotropy.

Intrinsic strain-induced anisotropies

The cubic magnetocrystalline anisotropy has three equivalent easy axes in the [100], [010] and [001] directions. However, due to the fact that (Ga,Mn)As is grown in thin layers, the simple cubic symmetry of the lattice is further distorted by the internal strains (**Chap. 1.2**). It can be shown that the small uniaxial deformations of the crystal lattice manifest themselves as an additional *uniaxial anisotropy*. [**62**] However, the local energy minimum of the system resulting from this additional anisotropy (i.e., the new "*easy axis*") does not generally correspond to the strain direction as the inherent cubic crystal symmetry has to be taken into account. The directions are equivalent only for the highly symmetrical cases, e.g., the main crystallographic axes and the diagonals [110], [-110]. Ref. [**62**] – [**63**].

There are two major types of the intrinsic strain acting in the thin (Ga,Mn)As samples. The first one is ***growth strain*** that occurs due to the lattice mismatch between the (Ga,Mn)As layer and the substrate – it is also referred to as a *biaxial pseudomorphic strain* e_0. It can be approximated in terms of the lattice constants of substrate (a_s) and relaxed epilayer (a_0) as $e_0 \approx (a_s - a_0)/a_0$ and its values range between $e_0 = 10^{-4} - 10^{-2}$.

As the total force acting on the system in equilibrium has to be zero, the in-plane compression leads to the expansion in the out-of-plane direction and vice versa (see Fig. 3.3). It gives rise to the uniaxial anisotropy in the [001] direction, described as:

$$F_{growth}\left(\hat{M}\right) = -K_{[001]} n_z^2 \qquad (3.3)$$

The *positive* value of the coefficient $K_{[001]}$ corresponds to the *tensile* biaxial strain and it thus describe the uniaxial anisotropy with the easy axis in the *out-of-plane direction*. The *negative* $K_{[001]}$

corresponds to the *compressive strain* and the easy axis lies *in the sample plane*. The latter one is also the more frequent case for (Ga,Mn)As grown on GaAs substrate.

The second type of "strain" in (Ga,Mn)As merely models the broken in-plane symmetry between the two crystallographic diagonals [110] and [-110] that are known to be non-equivalent from the experiments (for example [64], [65]). Such difference can be described by the ***effective shear strain*** $e^{int}_{xy} \approx 10^{-4}$, though the microscopic symmetry breaking mechanism still remains unrevealed. It is assumed that it occurs during the growth procedure and remains unaffected by any post-growth treatment [62]. In the standard strain formalism the corresponding contribution to the free energy takes the following form:

$$F_{sheer}\left(\hat{M}\right) = -\frac{K_{[110]}}{2}\left(n_y - n_x\right)^2 \tag{3.4}$$

If positive, the anisotropy constant $K_{[110]}$ favours the in-plane easy axis in [1-10] direction. This is also the most common case, though generally it depends on various parameters (hole and Mn concentration, temperature etc.), and the easy axis can even be rotated from [-110] to [110] by annealing. [64], [66].

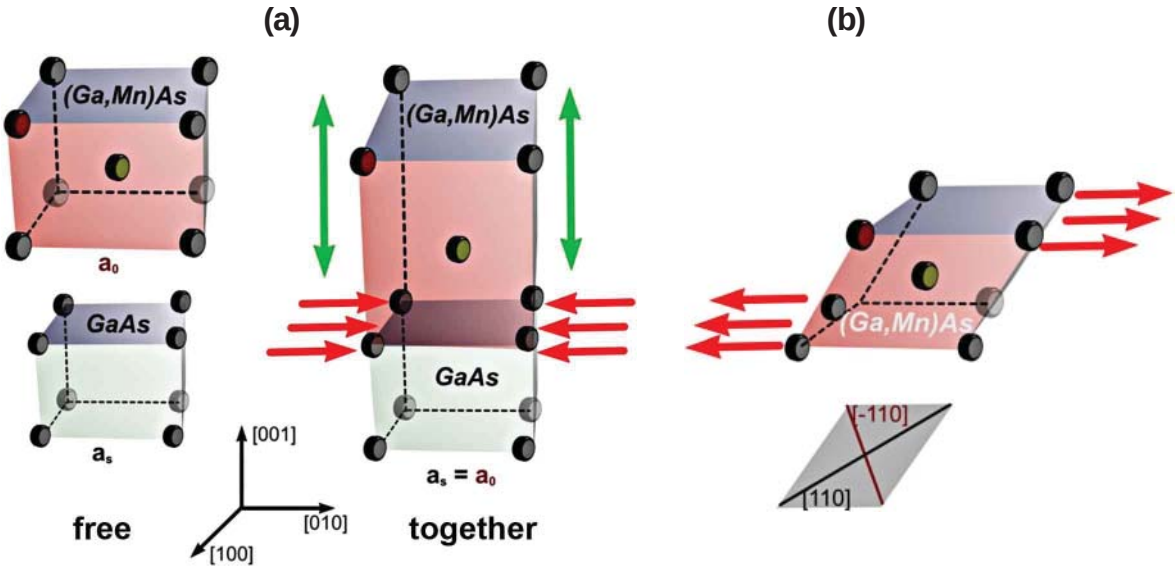

Fig. 3.3: Schematic illustration of the growth strain (a) and shear strain (b) that break the cubic symmetry of the (Ga,Mn)As when grown of GaAs substrate. Here a_0 represents the lattice parameter of the "free" (Ga,Mn)As layer, while a_s is the lattice parameter of the substrate (Ga,As in this case).

Shape anisotropy

The internal demagnetizing field that comes from the magnetic dipole-dipole interactions in the material results in another type of anisotropy that is connected with the shape of the sample. [67]. For thin layers with one dimension significantly smaller than the others, as is the case of all MBE grown (Ga,Mn)As samples, purely out-of-plane magnetic anisotropy occurs. The corresponding term has the form analogous to growth strain:

$$F_{shape} = 2\pi M_s^2 n_z^2 \tag{3.5}$$

where M_s denotes saturation magnetization. Due to the diluted nature of the ferromagnetism in (Ga,Mn)As and subsequent small magnitude of M_s, this type of the anisotropy is usually very small, and is either neglected or included into a much stronger out-of-plane growth anisotropy [**62**].

The resulting free energy functional that contains only the intrinsic magnetic anisotropy contributions is obtained by putting together the individual terms. To simplify the incorporation of external interactions it is more convenient to abandon the intuitive expressions given by equations (3.2)-(3.4) and to switch to spherical coordinates. The individual components of the unit vector $\hat{M} = (n_x, n_y, n_z)$ can be expressed as:

$$n_x = \cos\varphi \sin\theta\,,\ n_y = \sin\varphi \sin\theta\,,\ n_z = \cos\theta \tag{3.6}$$

where the angles θ and φ are polar and azimuthal angles measured from [001] and [100] directions (see Fig. 3.4), respectively.

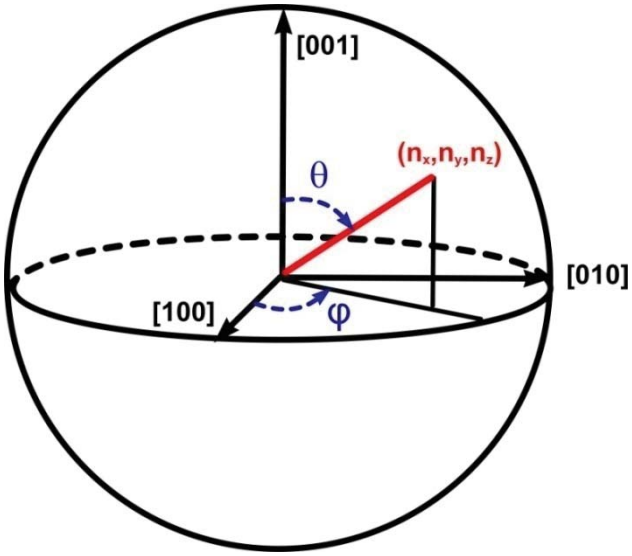

Fig. 3.4: Definition of the spherical coordinate system used in the text. The main axes correspond to the crystallographic directions [100], [010] and [110]. The magnetization unit vector M with the individual Cartesian components (n_x, n_y, n_z) can be described by the oriented azimuthal angle φ and polar angle θ

Furthermore, for the comparison with the experiments it is more convenient to use the anisotropy field convention, where the individual anisotropy fields are expressed as: $H_i = 2K_i/M_S$ [**62**], [**68**]. The total intrinsic free energy functional then goes to:

$$F_{\text{int}} = \frac{1}{2} M_s \left[H_c \sin^2\theta \left(\frac{1}{4}\sin^2 2\varphi \sin^2\theta + \cos^2\theta \right) - H_{[001]} \cos^2\theta + 2\pi M_s^2 \cos^2\theta \right.$$
$$\left. - \frac{H_{[110]}}{2} \sin^2\theta (1 - \sin 2\varphi) \right] \tag{3.6}$$

We will keep this notation in the further discussion.

B. Post-growth controlled strain

The connection between the strain and the magnetic easy axis provides a powerful tool for external manipulation of the magnetization. In the most common case, the uniaxial in-plane strain is generated by the nanopatterning or piezo stressing. If such strain is applied in-plane at

an azimuthal angle φ_{str} (as defined in Fig. 4), the uniaxial anisotropy with the easy axis aligned generally in a different direction Ω occurs. The contribution to the total free energy then takes the following form:

$$F_{\text{int}}(\hat{M}) = -K_{\Omega}\sin^2(\varphi - \Omega) \tag{3.7a}$$

$$F_{\text{int}}(\hat{M}) = -\frac{1}{2}H_{\Omega}M_s\sin^2(\varphi - \Omega) \tag{3.7b}$$

where K_{Ω} (H_{Ω}) is the corresponding uniaxial anisotropy constant (anisotropy field). If, however, the $\varphi_{tr} = n^*\pi/4$, where n is an integer, a special symmetrical case of $\varphi_{str} = \Omega$ occurs – as discussed with respect to the intrinsic shear strain in the previous section. For the out-of-plane strain component the situation becomes more complicated and it is described elsewhere [62].

C. External magnetic field

An interaction of the external magnetic field with the magnetized medium results in Zeeman contribution to the total free energy that depends on the direction in which the external field H_{ext} was applied. The corresponding term is:

$$F_{Zeeman} = -H_{ext}M_s\left[\cos\theta\cos\theta_H + \sin\theta\sin\theta_H\cos(\varphi - \varphi_H)\right] \tag{3.8}$$

where angles θ_H and φ_H indicate the polar and azimuthal angle of the external magnetic field (the same definition as in Fig. 4).

D. Total free energy functional

The general case of arbitrary (Ga,Mn)As layer in external magnetic field under an artificial uniaxial strain is then described by relatively complex free energy functional that comprises all the contributions given by equations (1.6)-(1.8).

$$F = \frac{1}{2}M_s\left[H_c\sin^2\theta\left(\frac{1}{4}\sin^2 2\varphi\sin^2\theta + \cos^2\theta\right) - H_{[001]}\cos^2\theta + 4\pi M_s\cos^2\theta - \right.$$
$$\left.\frac{H_{[110]}}{2}\sin^2\theta(1-\sin 2\varphi) - H_{ext}\left[\cos\theta\cos\theta_H + \sin\theta\sin\theta_H\cos(\varphi-\varphi_H)\right] - H_{\Omega}\sin^2(\varphi-\Omega)\right] \tag{3.9(a)}$$

Note that the demagnetization term that is small compared to the $H_{[001]}$ is often included into a single effective anisotropy field $H^{eff}_{[001]}$.

The position of the magnetization is given by a minimum of this functional, and with no external field applied, this minimum corresponds also to the position of the easy axis of magnetization. The anisotropy fields $H_{[110]}$ and H_c depend strongly on the parameters such as hole concentration and temperature. By their variation, the magnetization can be manipulated, as shall be shown in the experimental part of the thesis.

At this point we would like to stress that the set of the anisotropy fields H_c, $H_{[110]}$ and $H_{[001]}$ used to described the bare unpatterned (Ga,Mn)As sample is not the only possible choice. Especially the ferromagnetic resonance (FMR) experiments are typically analyzed by a different set of

constants corresponding to the projections of the magnetic anisotropy into certain directions. Assuming the same definition of the angles as in the previous sections (Fig. 3.4) the free energy takes in such notation the following form [**68**]:

$$F = \frac{1}{2} M_s \left\{ -2H_{ext}\left[\cos\theta\cos\theta_H + \sin\theta\sin\theta_H \cos\left(\varphi - \varphi_H\right)\right] + 4\pi M_s \cos^2\theta \right.$$
$$\left. - H_{2\perp}\cos^2\theta - \frac{1}{2}H_{4\perp}\cos^4\theta - \frac{1}{2}H_{4\parallel}\frac{1}{4}\left(3+\cos 4\varphi\right)\sin^4\theta - H_{2\parallel}\sin^2\theta\sin^2\left(\varphi - \frac{\pi}{4}\right)\right\}$$

(3.9(b))

Here the $H_{2\perp}$ and $H_{4\perp}$ represent the perpendicular uniaxial and cubic anisotropy fields, and $H_{2\parallel}$ and $H_{4\parallel}$ are the in-plane uniaxial and cubic anisotropy fields. Some pairs of the anisotropy constants used in the different notations – namely ($K_{2\perp}$, $K_{[001]}$) and ($K_{2\parallel,}$ $K_{[110]}$) – are identical. In order to convert the others, some neglecting is necessary, and the details can be found in [**62**].

3.1.4 Material fabrication

Some of the specific magnetic properties described in the previous chapters are connected with the fabrication procedure used for the thin (Ga,Mn)As layers, which we will now describe in more detail.

Growth

The (Ga,Mn)As layers are typically prepared by the method of molecular beam epitaxy (MBE) on two types of substrates – GaAs, that has a smaller lattice constant $a_{GaAs} < a_{GaMnAs,}$ and InAs, where $a_{InAs} > a_{GaMnAs.}$ The choice of the substrate is critical in terms of the magnetic anisotropy (see Fig. 3.3).

The solubility limit of Mn in GaAs is very low (around 0.1%) [**69**]. When grown under standard MBE conditions (temperature of 550-400 °C), higher doping leads to the segregation of Mn atoms on the surface and formation of MnAs inclusions instead of incorporation of Mn into the lattice. Therefore a non-equilibrium low temperature MBE (LT-MBE) method at approximately 200 °C has to be used to create the (Ga,Mn)As crystal [**49**]. The low temperature slows down the lateral diffusion of Mn atoms, thus preventing segregation and cluster formation and allowing for doping with as much 22% of Mn [**70**]. However, even the high doping level does not lead to an increase of the Curie temperature, as would be expected from Eq. (1.1). The highest $T_c = 185\ K$ ever achieved in GaMnAs was found in material doped by only 12% of Mn [**56**]. The reasons for the T_c boundary can be many. One explanation is based on the direct antiferromagnetic coupling between the neighbour Mn ions that are getting too close to each other with higher doping level. It can be the presence of defects, mainly Mn_I and $As_{Ga,}$ that compensate both the hole concentration and the magnetic moment of Mn. With higher doping level the amount of substitutional Mn_{Ga} is known to decrease compared to the interstitial $Mn_{I,}$ [**71**]. The defects can be partially removed by post growth treatment.

Annealing

The low binding energy of the Mn interstitials allows for their removing by annealing close to the growth temperature – e.g. ~ 230 °C. The defects diffuse thermally to the surface where they

are passivated and form a MnO layer. The ideal time and temperature of the annealing procedure has to be selected carefully for each doping and layer thickness in order to efficiently remove the majority of Mn_I from the whole sample volume and simultaneously avoid the formation of MnAs clusters [**69**]. The samples are optimized according to the highest $T_{C,}$ which has turned out to be a strong indicator of the sample quality [**20**]. It has been also shown that the annealing procedure leads to the layers of optimal properties only for samples of small enough thickness *d < 50 nm* [**69**]. In thicker layers, the defects cannot be efficiently removed from the whole sample volume which leads to their inhomogeneous distribution. The annealing process is schematically depicted in Fig. 3.5. This results in a gradient of magnetic properties that comes presumably from the gradient of hole concentration and/or magnetic momentum caused by the presence of gradient in Mn_I and which probably cannot be avoided. Note that even the as-grown thick samples contain certain magnetic inhomogeneity due to the annealing that occurs during the MBE growth. However, for the optimized thin layers (d < 50 nm), reproducible properties can be obtained by proper annealing.

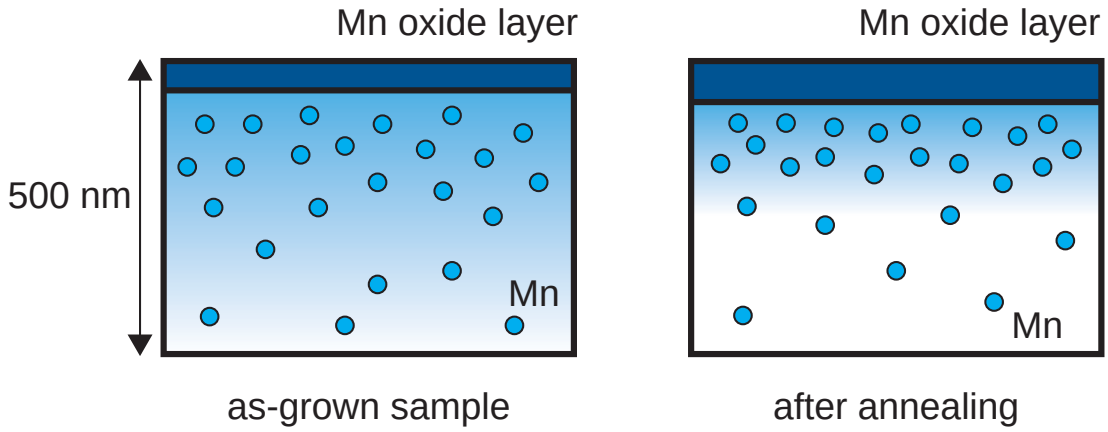

Fig. 3.5: Schematic depiction of the thick GaMnAs samples before and after the annealing process.

3.2 Magnetization dynamics in (Ga,Mn)As and other materials – published results

The speed of manipulation with magnetization direction and magnitude sets an intrinsic limit for the magnetic recording [**21**] and information processing technologies. The conventional way of recording by reversing magnetization with an external magnetic field is strongly limited by the length of the magnetic field pulses which hardly exceed a few nanoseconds. The electrical control of magnetization by the spin-transfer torque effect (STT) turned out to be one promising path to follow in order to increase the speed of magnetization switching [**72**], [**73**]. However, at the sub-picosecond timescale of an exchange interaction between magnetic moments, magnetization can be manipulated more easily by the ultrashort laser pulses [**74**] and traced using the magnetooptical effects (see **Chap. 2.1.2**) The laser light can trigger various processes in the material at such short timescales, from the ultrafast demagnetization [**74**]–[**76**], fast spin-reorientation [**77**] even to the modification of the magnetic structure [**78**], [**79**]. These highly non-equilibrium changes of magnetic properties and/or spin orientation cannot be explained in terms of the thermodynamic approach and the relevant physics, which is still not well understood [**21**], is beyond the scope of this thesis. Yet these effects manifest themselves in the macroscopic processes that can be

detected under quasi-equilibrium conditions. One of them is also the coherent laser-induced magnetization precession, which is the main objective of our work. In this chapter we would like to summarize some of the results that have so far been obtained in various materials on this topic. For the sake of clarity, we would first briefly introduce the standard description of the precession in a macroscopic approximation and its limitations.

3.2.1 Magnetization precession – general considerations [80], [81]

Description of the magnetization motion is based on an analogy to the standard motion of a single magnetic moment **m** subject to an external magnetic field **H**, which is given by the torque equation:

$$\frac{d}{dt}\frac{\vec{m}}{\gamma} = -\vec{m}\times\vec{H} \tag{3.10}$$

Here γ denotes the gyromagnetic ratio. If we assume the magnetic moments (i.e. spins) homogeneously distributed in a volume *V*, we can take them as a macroscopic quantity, the *net magnetization* $\boldsymbol{M} = n\boldsymbol{m}/V$, where *n* is the number of spins in volume *V*. Furthermore, the torque can have different origins than the external magnetic field – the change of material anisotropy, demagnetization field, etc. [**80**]. All of them are included into an effective magnetic field $\boldsymbol{H}_{eff}$, defined as:

$$\vec{H}_{eff} = -\frac{\partial F}{\partial \vec{M}} \tag{3.11}$$

where *F* represents the total free energy. Thus, Eq. (3.10) can be rewritten in the form of a *Landau-Lifshitz equation:*

$$\frac{d\vec{M}(t)}{dt} = -\gamma\left(\vec{M}(t)\times\vec{H}_{eff}(t)\right) \tag{3.12}$$

The $\boldsymbol{H}_{eff}$ term has to be derived for each system where the free energy *F* is known. If the viscous damping term (i.e. term linearly proportional to the magnetization change d**M**/dt) is introduced, Eq. 3.12 goes to the well known *Landau-Lifshitz-Gilbert (LLG)* equation [**80**]:

$$\frac{M(t)}{dt} = -\gamma\left[\vec{M}(t)\times\vec{H}_{eff}(t)\right] + \frac{\alpha}{M_s}\left[\vec{M}(t)\times\frac{d\,M(t)}{dt}\right] \tag{3.13}$$

where M_s stands for saturation magnetization, and α is a Gilbert damping parameter. The LLG equation can be rewritten in spherical coordinates [**80**].

$$M_x = M_S\sin\theta\cos\varphi$$
$$M_y = M_S\sin\theta\sin\varphi$$
$$M_z = M_S\cos\theta$$

The same convention is used for the angles θ, φ as in Fig. 3.4. Assuming the saturation magnetization remains constant, the equations of motion are [**80**]:

$$\frac{dM_s}{dt} = 0 \tag{3.14 (a)}$$

$$\frac{d\theta}{dt} = -\frac{\gamma}{\left(1+\alpha^2\right) M_s}\left(\alpha \cdot \frac{dF}{d\theta} + \frac{1}{\sin\theta}\frac{dF}{d\varphi}\right) \tag{3.14 (b)}$$

$$\frac{d\varphi}{dt} = \frac{\gamma}{\left(1+\alpha^2\right) M_s \sin\theta}\left(\frac{dF}{d\varphi} - \frac{\alpha}{\sin\theta}\frac{dF}{d\varphi}\right) \tag{3.14 (c)}$$

If the damping term can be neglected (i.e. $\alpha = 0$) and all the variations are small enough [**81**], the magnetization motion can be decomposed into small harmonic oscillations around the equilibrium position given by φ_0 and θ_0, with the amplitudes φ_0, θ_A, respectively:

$$\theta - \theta_0 = \theta_A e^{-i\omega t}\,,\ \varphi - \varphi_0 = \varphi_A e^{-i\omega t} \tag{3.15(a)}$$

The physical solution can be then taken as a real part of these expressions:

$$\theta - \theta_0 = \theta_A \cos(\omega t)\,,\ \varphi - \varphi_0 = \varphi_A \cos(\omega t) \tag{3.15(b)}$$

By solving the set of equations (3.14) with the above described harmonic motion taken into account, one obtains the following expression for the precession frequency ω [**81**]:

$$\omega = \frac{\gamma}{M_S \sin\theta}\sqrt{\frac{\partial^2 F}{\partial\theta^2}\frac{\partial^2 F}{\partial\varphi^2} - \left(\frac{\partial^2 F}{\partial\varphi\partial\theta}\right)^2} \tag{3.16}$$

This analytical formula relates the precession frequency with the effective magnetic fields in a given system and it can be derived with the proper free energy functional *F*. It is then sometimes referred to as the *Kittel formula.*

The LLG equation in its original form given by Eq. (3.13) describes the dynamics of a uniform magnetization precession, where all the spins behave as a one macrospin – so called *Kittel mode* [**81**]. In such case, the $\boldsymbol{H}_{eff}$ field contains only the contributions from the anisotropy field $\boldsymbol{H}_{anis}$, demagnetization field (shape anisotropy) $\boldsymbol{H}_{demag}$, and external magnetic field $\boldsymbol{H}_{ext}$ (**see Chap. 3.1.3** for details in GaMnAs). This mode is usually excited in homogeneous materials and in very small magnetized particles (21). In the case of macroscopic samples and for the samples that are magnetically inhomogeneous, the magnetization vector depends on the spatial coordinates, ***M = M (r,t)***. The magnetization precession is no longer uniform and higher excitations, so called "spin waves" (SW), appear.[1] There are various types of SW modes generated in laterally confined structures [**82**]. More details on the SW modes can be found in [**80**]. However, one type of SWs holds a special importance with respect to this work. These are the perpendicular SW resonances that occur in the sample with its thickness significantly smaller than the lateral dimensions. The SW propagating across the layer can be retro-reflected and create standing waves of different spatial profiles depending on the boundary conditions, inhomogeneity profiles etc. – SW resonance (SWR). These modes have been detected in a variety of materials [**83**], [**27**], [**84**].

[1] Note that the above described Kittel mode is just a special case of SW with **k** = 0.

The magnetization dynamics in the presence of SWRs can be obtained by solving the LLG equation, assuming that the magnetization $\boldsymbol{M = M(r,t)}$ and/or the effective field $\boldsymbol{H_{eff}}$ is spatially dependent. Furthermore, a special contribution has to be added to the effective field $\boldsymbol{H_{eff}}$. The modes of interest are typically dominated by an exchange interaction, and the corresponding term takes the following form [**81**], [**85**]:

$$\vec{H}_{exch} = \frac{D}{g\mu_0 M_s}\nabla^2 \vec{M} \tag{3.17}$$

Here D denotes the spin stiffness parameter. In order to obtain the spatial profile of the SW modes, boundary conditions to the LLG equation (3.13) have to be considered. An example of the simplest perpendicular standing SW modes of the order p, with open and fixed boundary conditions is shown in Fig. 3.6.

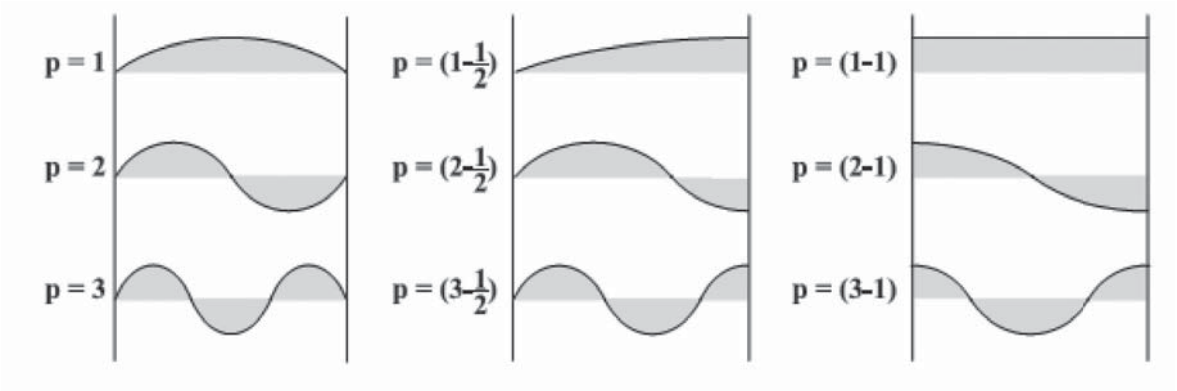

Fig. 3.6: Standing spin waves of different order p with open and fixed boundary conditions [**86**].

3.2.2 Magnetization precession in FMR

The above described magnetization precession can be induced by various experimental techniques, and detected both in time and frequency domains. In the frequency domain, ferromagnetic resonance (FMR) is the most commonly used method. In comparison, the laser induced magnetization precession observed by a time-resolved magnetooptics (**Chap. 2.1.2**) makes an important alternative to FMR in the time domain, where the damping and other parameters are more easily accessible [**27**]. Let us now briefly compare these two experimental techniques.

In FMR, the precession frequency ω is fixed by a microwave cavity, and the free energy F is tuned by an external magnetic field so that at a certain field H_{res} the resonance in the $\boldsymbol{\omega(H)}$ spectrum occurs [**87**]. The resonance field measured in different geometries is used in FMR to determine the equilibrium contributions to the effective fields and thus also the magnetic parameters, according to Eq. (3.16) with proper free energy functional [Eq. 3.9.(b)]. Information about the Gilbert damping parameter can be extracted from the variation of the FMR resonance linewidth with the microwave frequency ω [**88**], [**87**].

$$\Delta H_{pp} = \Delta H_{inho} + \frac{2}{\sqrt{3}} \frac{\alpha}{\gamma} \omega \tag{3.18}$$

Here ΔH_{pp} is the first derivative peak-to-peak linewidth of the Lorentzian lineshape, α the Gilbert damping factor and γ gyrromagnetic ratio. ΔH_{inhom} represents the inhomogeneous FMR linewidth which is generally of an extrinsic origin [**87**]. As the frequency ω is typically fixed by the resonance cavity, it is rather complicated to obtain the values of the intrinsic parameter α from the FMR measurements [**88**].

In the TRMO method, the situation becomes very similar to FMR if we consider time scales where the system already reaches quasi-equilibrium state that is observed in the FMR. The oscillatory signal measured in the TRMO on a relevant time scale (several ns) corresponds to the precession of magnetization and the precession frequency can be described by the same formula [Eq. (3.13)] as in the FMR [**81**], [**27**]. The same anisotropy constants can be obtained from both methods – see Fig.2 in [**27**]. In addition, the TRMO method offers several advantages, such as higher flexibility in terms of the external parameters, possibility to evaluate the Gilbert damping directly from the precession damping etc.

Despite all the similarities, there is a significant difference between the FMR and TRMO methods in the way the magnetization precession is excited. In the FMR, the torque on the magnetization is exerted by the external magnetic field which also imposes restrictions on the generation of different magnetic modes (spin-waves SW – see the previous section). On the other hand, laser light can trigger the magnetization precession by various effects and the SWs are excited with no *k*-selectivity [**83**]. According to [**21**], the effects responsible for the magnetization precession can be roughly separated into the *thermal* and *non-thermal* classes which we shall discuss separately.

A. Magnetization precession induced thermally

In an absorbing material, the impact of a laser pulse leads to a transfer of the photon energy to the electrons/hole pairs and consequently also to the phonons. Different types of interactions (electron-electron, electron-phonon or electron-spin) can lead to the changes of magnetization [**21**]. These changes result in a ultrafast modification of the sample magnetic anisotropy which exerts a torque on the magnetic moments and causes the magnetization to precess (see previous section), assuming the modification is faster than one precession period. The precession of magnetization around the new quasi-equilibrium position obeys the LLG equation (see section 3.2.1), and the subsequent return of the system to its initial state is then connected mainly with the heat transfer from the excited spot to the sample. *Ferromagnetic metals* represent an important example of the systems where the laser-induced heating causes strong changes of magnetic anisotropy [**75**], [**83**]. Furthermore, the precession of magnetization (MP) can provide information about various magnetic properties and interactions, which can depend significantly on the material or structure investigated. In *exchange-biased systems*, such as NiFe/NiO bilayer (ferromagnetic/antiferromagnetic) used in [**88**], the laser-induced heating drives MP in the ferromagnetic NiFe, as it modifies exchange coupling between the two layers. In *ferrimagnetic compounds,* with rare-earth–3d transition metal system as the typical example, the roles of individual sub-lattices and their mutual compensation of both the magnetization and in the angular momentum can be observed through MP [**89**], and singular point with an extremely

high precession frequency and damping can be found [**90**]. The higher spin wave modes were extensively studied particularly in artificial nanostructures, where the lateral confinement leads to much richer spin wave spectra [**84**], [**91**]–[**93**]. These cases are just a few examples of the observed phenomena, and more details can be found elsewhere [**80**]

B. Magnetization precession of non-thermal origin

The *non-thermal* class of effects that lead to the magnetization precession covers two major types of phenomena (according to [**21**]) – *photomagnetic* and *optomagnetic*. Unlike the thermal processes described in previous chapter, the major fingerprint of the non-thermal effects is a strong dependence on the polarization of the inducing light. Otherwise, there is a significant difference between the physics of the two classes. The *optomagnetic* effects do not require absorption of any photons; they rely solely on the coherent processes such as inverse magnetooptical (IMO) effects – a change of the magnetization that depends on the light *polarization.* The overall duration of the *optomagnetic* effects is thus connected with the coherence time in the material and it typically does not exceed 200 fs. The IMO represent an analogy to the standard MO effects (**Chap. 1.4.2**), and they can be described by the same MO constants of the material [**30**]. On the other hand, the *photomagnetic* effects are induced by a transient change of the magnetic properties (such as the magnetic anisotropy), caused by an *absorption* of the light. Their duration is thus given by a lifetime of the carriers in the corresponding energy levels [**30**].

The precession of magnetic moments induced by the *optomagnetic* effects has been so far extensively studied in magnetic oxides [**28**], [**94**] or metal compounds [**89**], where the inverse Faraday rotation (IFR) prevails. As such, the precession is induced only by circularly polarized light. The all-optical control of the magnetization precession induced by an IFR has also been demonstrated in magnetic garnets [**95**]. The corresponding theory has been elaborated to describe the IMO effects from a microscopic point of view [**21**]. In the case of the *photomagnetic* processes, several experiments showed the possibility to trigger the precession of magnetic moments by linearly polarized light [**96**], [**95**]. Changes of the magnetocrystalline anisotropy due to the light-induced carrier re-distribution turned out to be responsible for the magnetization precession in these materials. The possibility to directly transfer an angular momentum of the absorbed circularly polarized light to the magnetic moments of the material was theoretically proposed in [**97**] but it has never been proven experimentally. The experiments aiming to detect this phenomenon in (Ga,Mn)As form one of the cornerstones of this thesis, as shall be shown in **Chap. 3.4**. First, we would like to summarize the results already published on the magnetization dynamics in (Ga,Mn)As in general.

3.2.3 Magnetization dynamics in (Ga,Mn)As – published results

Since the first fabrication of the artificial magnetic semiconductor (Ga,Mn)As [**49**], [**50**] its material properties have been thoroughly investigated by a whole range of the experimental methods (more details in [**69**]) and the theory describing its unusual type of the ferromagnetism mediated by the itinerant holes was addressed [**61**], [**59**]. As a result of the carrier mediated ferromagnetism, the magnetic properties of the material are strongly carrier-concentration dependent, as was demonstrated directly in the experiments where the ferromagnetism was electrically gated [**31**], [**32**], [**136**].

In the frequency domain, an extensive FMR study was performed. The magnetic properties of the (Ga,Mn)As samples, where the number of itinerant carriers was changed by the manganese doping and annealing [**98**] or hydrogen passivation [**99**], [**100**], were addressed. The magnetic

anisotropy was found to be strongly correlated with not only with the carrier concentration, but also with the sample temperature and strain that was modified by using different substrates for the (Ga,Mn)As layers – for review see [**68**]. Furthermore, the exchange interactions in (Ga,Mn)As were investigated in detail by measuring the spin-wave resonance (SWR) spectra under different conditions, and the corresponding spin stiffness parameter D was extracted from the measurements (see [**101**], [**85**]). The experimental values of D as a function of Mn doping were further compared with the theory (see Fig. 12 in Ref. [**102**]). However, due to the influence of the sample homogeneity, which was found to cause deviations in the SWR spectra [**103**] – [**106**], the experimental values were rather scattered.

The strong dependence of the magnetic properties of (Ga,Mn)As on several parameters (e.g. carrier concentration, temperature etc.) makes it possible to induce fast changes [**76**] by the ultrashort laser pulses, as described in the previous chapter. The laser induced magnetization precession in the range of the FMR frequencies was reported in several works [**107**] – [**112**], and the influence of a Mn doping [**111**], [**112**] and thermal annealing [**111**] was investigated. Furthermore, a presence of non-uniform magnetization dynamics was reported in [**113**] where it was attributed to the hybrid bulk-surface spin wave modes. The standard bulk SWR, similar to those detected by the FMR, will be shown here in **Chap. 3.5.**

The reported laser-induced magnetooptical (MO) signals were independent of the polarization of the excitation light, and it is now generally accepted that the impulsive change of the magnetic anisotropy caused by the laser excitation is the origin of the precession. However, the exact mechanism is still under discussion [**108**], [**110**]. If the laser light is tuned above the band gap of the material, the absorption of the laser pulse leads to the transient change of the lattice temperature and of the hole concentration, both of which can strongly affect the anisotropy on the time scales relevant to the experiment. Thermal origin of the precession was concluded in [**111**]. On the other hand, the non-thermal *photomagnetic* processes were claimed to be responsible for the precession detected at very similar experimental conditions (pump power, temperature etc.) by in Ref. [**108**], [**109**]. Unlike the rather straightforward thermal change of the in-plane magnetic anisotropy, the non-thermal processes were explained using slowly varying out-of-plane anisotropy field caused by the photoinjected holes. The non-thermal *photomagnetic* origin of the precession was theoretically predicted in [**97**] and the corresponding experiments will be presented later in this work (**Chap. 3.8**).

From the technological point of view, the anisotropy related origin of the precession enabled an efficient control of the magnetization dynamics by the external means – either optically by the second time-delayed pump pulse [**114**] or by strain induced lithographically in patterned structures [**115**]. Moreover, the influence of the strain on the magnetization dynamics provides a powerful tool for its electrical control by piezo stressing, as shown in [**13**], [**116**], [**117**] and as will be demonstrated in the TRMO experiment in this work.

Before we illustrate the possibility to control the magnetization dynamic in (Ga,Mn)As, we will first show the basic results obtained from the TRMO measurements that lead to the detailed understanding of the laser-induced precession in our (Ga,Mn)As samples.

3.3 Laser-induced magnetization precession in (Ga,Mn)As – basic experiments

In this chapter we would like to summarize the results obtained by the methods of ultrafast laser spectroscopy in pure (Ga,Mn)As layers. We will show that the detected oscillatory time-resolved magnetooptical signal (TRMO) indeed reflects the laser induced magnetization precession. Only the magnetization dynamics that does not depend on the polarization of the excitation pulse, i.e. the one that results purely from a transfer of the excitation *energy* to the system, will be discussed in this section, while the processes connected with a transfer of the photon angular momentum will be analyzed later in **Chapters 3.6** and **3.7**. We will discuss the mechanism leading to the magnetization precession from the experimental point of view, while the theoretical model describing the phenomenon will be analyzed in detail in **Chapter 3.4**.

3.3.1 Samples

The samples studied within this work were (Ga,Mn)As layers, grown by low temperature molecular beam epitaxy (LT-MBE) at the Institute of Physics of Academy of Sciences in Cukrovarnická, Prague, where they were also characterized using a superconducting quantum interference device (SQUID). Fig. 3.7 shows a schematic depiction of the (Ga,Mn)As samples. A semi-insulating GaAs (SI-GaAs, *500 μm* thick) was used as a substrate on top of which first the pure GaAs buffer layer (thickness *~ 200-400 nm*, depending on individual sample) was deposited at *~ 570 °C.* Afterwards, the temperature in the MBE cell was lowered to *~ 230 °C* and the (Ga,Mn)As layer was grown.[2] The layers of (Ga,Mn)As with various thickness were fabricated, and all of them were treated by post-growth annealing in order to improve their magnetic properties (see **Chap. 3.1.4**).

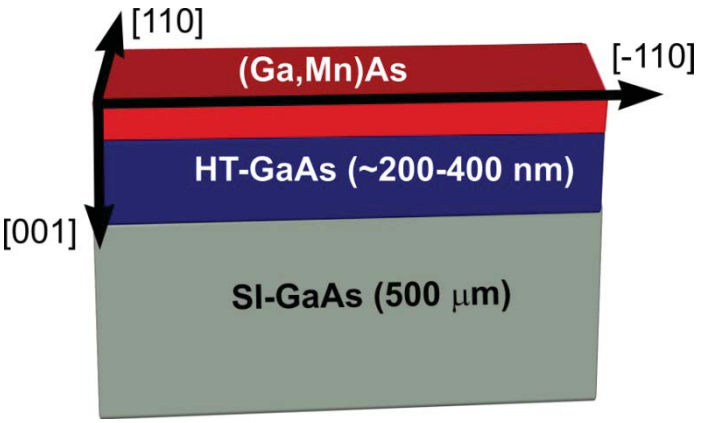

Fig. 3.7.: Schematic depiction of the samples with indication of the main crystallographic directions. Here HT-GaAs represents a pure GaAs grown by standard MBE at ~ 570° C on top of a semi-insulating GaAs substrate (SI-GaAs).

Generally, there are two types of (Ga,Mn)As layers used in this work. The individual (Ga,Mn) As samples and their properties are summarized in a Table 1.

sample	x_{nom} [%]	L [nm]	annealing	T_c [K]	p_0 [cm^{-3}]
C037#9	6	500	no	60	
C037#6	6	500	30 hours @ 200 °C	90	
D071#5	7	50	14 hours @ 200 °C	160	7 x 10^{20}

[2] In the beginning of the fabrication (the first generation of the samples), a 5nm thin layer of low temperature GaAs grown at ~230 °C was deposited before the actual growth of the (Ga,Mn)As started.

The first generation of samples contained 500 nm thick (Ga,Mn)As layers. In our work we used the samples ***C037*** with a nominal concentration of Mn atoms x_{nom} = *6 %***.** We denote the *as-grown* sample as ***C037#9*** and the *annealed* sample as ***C037#6***. The corresponding SQUID magnetic characterization is shown in Fig. 3.8. From the temperature dependence of the magnetization, the Curie temperature (T_c) for both layers is determined. From the SQUID magnetization measurement in different crystallographic directions (Fig. 3.8) it also directly follows that the magnetization easy axis (EA) lies in the sample plane[3]. In the case of the as-grown sample, the character of the magnetic anisotropy is more „cubic-like" – the EAs are located near the cubic [010] axis [(see Fig. 3.8. (c)], and they shift towards the [-110] direction with the annealing [Fig. 3.8. (d)].

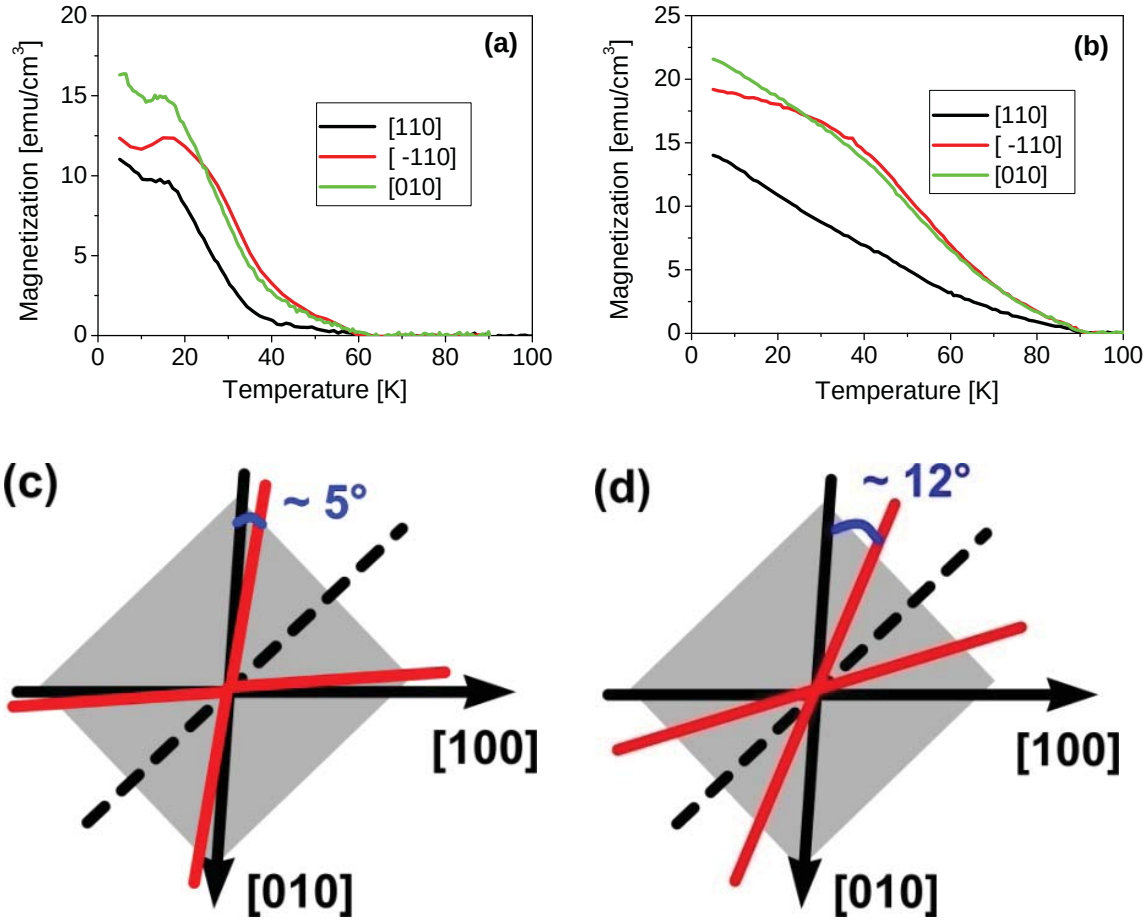

Fig. 3.8: Projections of the magnetization into different crystallographic directions, measured as a function of temperature by SQUID for the as-grown *C037#9* (a) and annealed *C037#6* (b) sample, respectively. The schematic cartoons (c) and (d) show positions of the easy axes (red lines) with respect to the main crystallographic directions (arrows) in the (c) as-grown and (d) annealed sample, as extracted from the SQUID measurements (a) and (b).

The 500 nm thick (Ga,Mn)As samples C037 encountered several problems connected with the reproducibility of the fabrication procedure, partial annealing during growth etc. [**69**]. As explained earlier (**Chap. 3.1.4**), the post-growth annealing can result in a magnetic inhomogeneity in the growth direction. Consequently, also their material properties were not reliably determined. The second generation layers were therefore only *50 nm* thick. We studied one specimen from this series, denoted as ***D071#5***, which was a 50 nm layer doped by x_{nom} = *7 %* of Mn, annealed for *14*

[3] For the (Ga,Mn)As layers grown on the GaAs substrate, the easy axis lies generally in the sample plane – see chapter 3.1.3 for the detailed description of the magnetic anisotropy.

hours at *200 °C*. The number of the Mn atoms incorporated into the lattice x_{eff} = *6.3 %* was calculated from the low temperature magnetization obtained by SQUID, and the hole concentration $p_0 \approx 7 \times 10^{20}$ cm^{-3} from the transport measurements [**69**]. The corresponding magnetic characterization by SQUID is presented in Fig. 3.9 (a). Clearly, the higher T_c = *160 K* in the sample ***D071#5*** with similar Mn doping than those of the ***C037*** samples (where T_c = *90 K*) indicates much better magnetic quality. In this sample, the magnetic easy axes are located near the [-110] direction in a "closed scissor like" formation [Fig. 3.9. (b)].

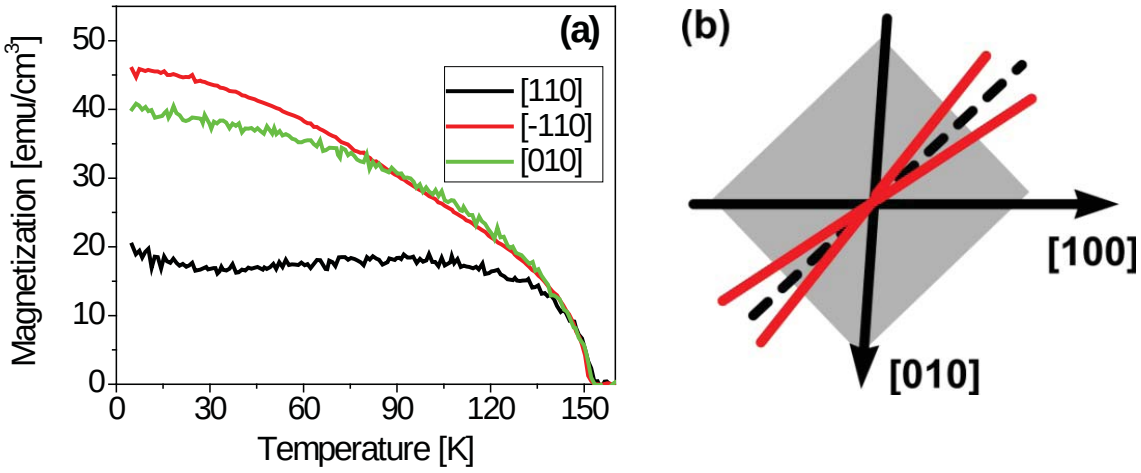

Fig. 3.9: (a) Projections of the magnetization into different crystallographic directions, measured as a function of temperature by SQUID for sample *D071#5*. (b) Schematic depiction of the easy axes (red lines) positions with respect to the crystallographic directions (arrows)

In order to complete the description of the samples used in this work, we would like to point out that there exists a whole set of *20 nm* thick layers, where the growth and post-growth treatment was independently optimized for each doping *x*, and very good fabrication reproducibility was achieved. A wide range of doping is accessible within this set [**20**]. These samples were used for the voltage control experiments, and details will be given in **Chap. 3.5**.

3.3.2 Experimental observation of laser-induced magnetization precession

The experiments presented in this section were carried out in standard pump-probe setup described in detail in Chap. 2.1. Unless noted differently, the data were measured at low temperature (15 K) and the wavelength used in the experiments was set to 758 nm. The angles of the probe beam polarization *(β)* and of the variable external magnetic field H_{ext} *(*φ_H*)* are defined as shown in Fig. 3.10. Typically, the field was applied along [010] direction *(*φ_H = *90°)* and polarization set to [010] *(β= 90°)*.

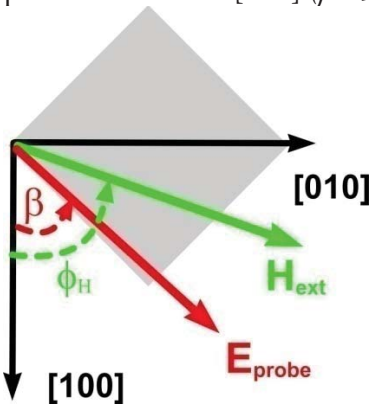

Fig. 3.10: Definition of the angles in the experiments. β denotes angle of the probe beam polarization $\boldsymbol{E}_{probe}$ and φ_H angle of the external magnetic field $\boldsymbol{H}_{ext}$

In Fig. 3.11 (a) we present typical transient rotation of the polarization plane of the annealed D071#5 sample, measured at low temperature (15 K) with excitation by laser pulses of different linear (*s* and *p*) and circular (σ^+ and σ^-) polarizations. Apparently, this oscillatory time-resolved magnetooptical (TRMO) trace does not depend significantly on the polarization of the excitation pulse. In the further analysis performed in this chapter we will, therefore, focus only on the polarization-independent part of the TRMO signals, which is obtained by averaging over the excitation polarizations [i.e. $(\sigma^+ + \sigma^-)/2$ or $(s+p)/2$]. The polarization-dependent signal that may occur under different experimental conditions will be discussed separately in **Chap. 3.6**.

The polarization-independent components of the TRMO trace measured below and above the sample Curie temperature are depicted in Fig. 3.11 (b) (T_c = 160 K for the sample D071#5). Apparently, the distinct oscillatory behavior occurs only if the sample is in a ferromagnetic state, while in a paramagnetic (Ga,Mn)As only a much weaker non-oscillating signal is present. This fact suggests that the signal results from a laser-induced change of the magnetization.

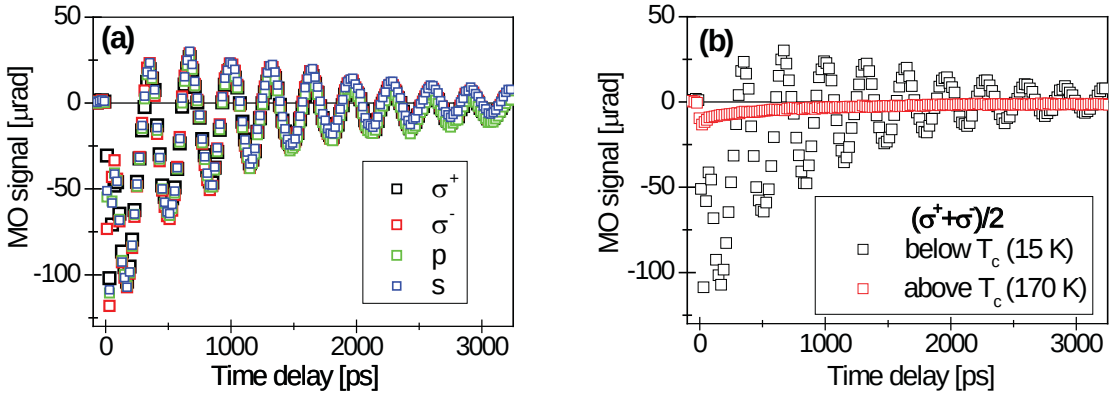

Fig. 3.11: Transient rotation of the polarization plane measured in the sample D071#5 (a) for different excitation polarizations at T = 15 K and (b) polarization-independent signal detected below and above T_c = 160 K. The magnetic field $\mu_0 H_{ext}$ = 10 mT, wavelength γ = 770 nm and pump fluence I = 21 μJ.cm^{-2}.

In order to confirm the magnetic origin of the oscillations, two different TRMO signals were recorded (Fig. 3.12). Generally, any magnetooptical (MO) signal of a magnetized medium has its "optical" and "magnetic" part. The rotation of the polarization plane (θ) and the change of the ellipticity (η) can be expressed in the following form [**118**]:

$$\Theta = f_\Theta \cdot M \quad , \quad \eta = f_\eta \cdot M \tag{3.19}$$

where M is magnetization and f_θ, f_η are functions that depend on the electronic properties of the material and that are connected with the index of refraction and absorption coefficients. The light-induced change of the MO signals detected in the TRMO experiments consists therefore of two components:

$$\Delta\Theta(t) \approx f_\Theta \cdot \Delta M(t) + M \cdot \Delta f_\Theta(t) \tag{3.20 (a)}$$

$$\Delta\eta(t) \approx f_\eta \cdot \Delta M(t) + M \cdot \Delta f_\eta(t) \tag{3.20 (b)}$$

where only the first term reflects the light-induced changes of the magnetization. Therefore, the two TRMO signal have to be measured simultaneously for a correct interpretation of the measured

signal (see Fig. 3.12). On nanosecond time scales the two TRMO traces are closely similar, and thus the majority of the signal is indeed of magnetic origin. In all the following data we will always present the pump-induced rotation of the probe polarization, denoted as "*MO signal*."

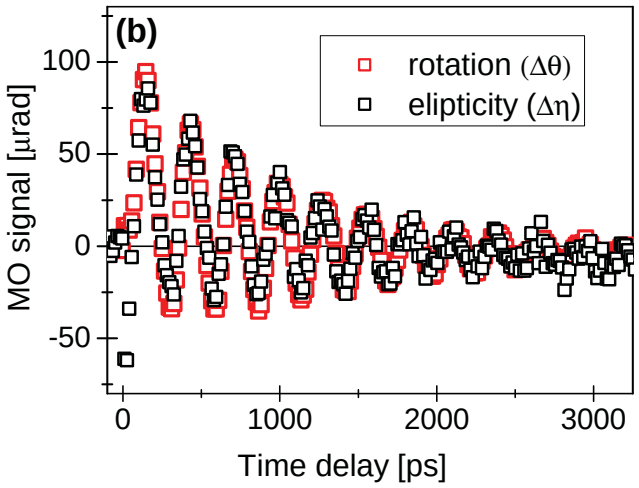

Fig. 3.12: Dynamics of the rotation of the polarization plane and change of ellipticity in sample D071#5, measured at T = 15 K. Probe beam polarization angle was set to β = 60°.
$\mu_0 H_{ext}$ = 17 mT, λ = 757 nm and I = 28 μJ.cm^{-2}.

The oscillatory TRMO trace can be fitted well [see Fig. 3.13 (a)] by a damped harmonic function superimposed on a pulse-like function that corresponds to a time-dependent background:

$$\delta MO(t) = A\cos(\omega t + \Delta)\exp\left(-\frac{t}{\tau_D}\right) + C\left[1-\exp\left(\frac{t}{\tau_1}\right)\right]\exp\left(-\frac{t}{\tau_2}\right) \qquad (3.21)$$

Here A, ω, Δ and τ_D are the amplitude, angular frequency, phase and damping time of the oscillatory part of the signal. The pulse-like background is characterized by its amplitude (C), rise time (τ_1) and damping time (τ_2).

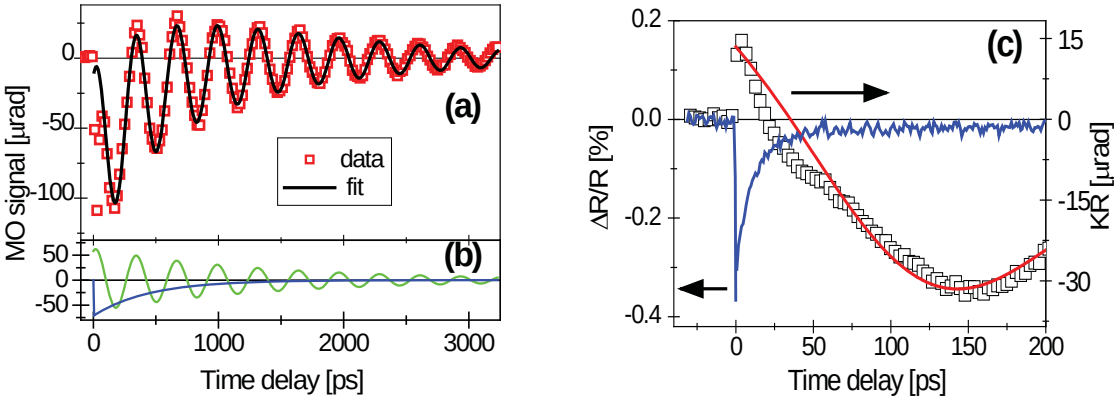

Fig. 3.13: (a) The polarization-independent part of the Kerr rotation signal shown in Fig. 3.12 (points) is fitted (solid line) by a sum of the exponentially damped sine harmonic oscillation [green line in part (b)] and the pulse-like KR signal [blue line in part (b)]. (c) Dynamics of the reflectivity change and the detail of the KR signal shown in part (a).

In Fig. 3.13(b) the TRMO data are shown together with the simultaneously detected dynamic of the reflectivity ΔR/R, which is connected with the transient change of the refraction index. At the short time-scales below 50 ps, where the ΔR/R has a significant contribution, the TRMO signal cannot be fitted properly by the phenomenological Eq. (3.21). Furthermore, the $\Delta\theta(t)$

and $\Delta\eta(t)$ traces also differ (see Fig. 2 in Ref. [119]), which indicates that the "optical" part plays a sizable role in this signal.

The detected $\Delta R/R$ provides us with information about the dynamics of the photoexcited electrons [**15**]. We can conclude that the majority of the electron population decays within ≈50 ps after the excitation. This result is in accord with the behavior observed in low-temperature GaAs [**23**], where the short electron life time is a consequence of the large concentration of the non-radiative recombination centers that arise during the LT-MBE growth.

In Fig. 3.14 (a) we show the dependence of the angular frequency ω on the external magnetic field H_{ext}, applied in the [010] direction. The angular frequency ω of the oscillations increases with the external magnetic field as predicted by the standard gyromagnetic theory (see **Chap.3.2.2**). The important point for the discussion is that the slope of the dependence corresponds to the g-factor of 2 for Mn^{2+} spins. This fact, together with the disappearance of oscillations for sample temperatures above T_C [see Fig. 3.11(b)] confirm that the oscillatory KR signal is connected with the precession of the *ferromagnetically coupled Mn* spins in (Ga,Mn)As. As these localized Mn moments form a net magnetization of the sample, the process can be regarded as a *light induced magnetization precession*.

The $\omega(H_{ext})$ dependence presented in Fig 3.14 (a) can be described well by the Kittel formula [red line in Fig. 3.14 (a)], derived for the free energy F of the (Ga,Mn)As sample (Eq. 8 in Ref. [**68**], assuming $H_{ext} \parallel$ [010] direction):

$$\omega = \gamma \sqrt{(H_{ext} + H_{4\parallel} + 4\pi M - H_{2\perp} + 0.5H_{2\parallel})(H_{ext} + H_{4\parallel})} \qquad (3.22)$$

$$\gamma = g \frac{\mu_B}{\hbar}$$

The $g = 2$ of Mn spins, and the corresponding anisotropy constants are: $\mu_0 H_{2\perp}$ = -395 mT, $\mu_0 H_{2\parallel}$ = 31.2 mT, $\mu_0 H_{4\perp}$ = 41.5 mT, $\mu_0 H_{4\parallel}$ = 22.5 mT. These constants are in good agreement with those measured independently by FMR on nominally the same sample [**121**]. We can thus conclude that the magnetization precession takes place in the *quasi-equilibrium* anisotropy field of the sample under the given experimental conditions. However, it is worth noting that the simple form of the Kittel formula (Eq. 3.22) describing the relation between H_{ext} and ω is valid only when the magnetization is aligned with the external field. This condition is fulfilled in FMR but not always in our TRMO experiments. For the external H_{ext} low enough[4] the shift of the easy axis (EA) has to be taken into account, and the solution of Eq. (3.16) becomes more complicated.

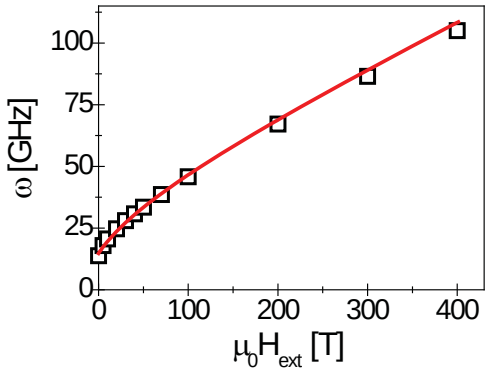

Fig. 3.14: (a) Dependence of the angular frequency ω on H_{ext}, applied in the [010] direction (points), measured at T = 15 K. The line is a fit with Eq. 3.22 and the following set of anisotropy constants: $\mu_0 H_{2\perp}$ = -395 mT, $\mu_0 H_{2\parallel}$ = 31.2 mT, $\mu_0 H_{4\perp}$ = 41.5 mT, $\mu_0 H_{4\parallel}$ = 22.5 mT; these are in agreement with the constants obtained by FMR.

[4] The exact value of the H_{ext} where the shift of the easy axis becomes sizable depends not only on the magnetic anisotropy of the sample but also on the orientation of H_{ext}

Let us now have a closer look at the processes leading to magnetization precession. It is generally accepted (see **Chap. 3.2.3** for the overview) that the precession is triggered by an impulsive change of the magnetic anisotropy. Yet the exact mechanism of such anisotropy change is still under discussion, as both the laser-induced transient heating (ΔT) [**110**] and the change of the hole concentration (Δp) [**109**], [**108**] have been so far considered as possible origins.

From the dynamics of $\Delta R/R$, shown in Fig. 3.13 (b) we can conclude that the population of photogenerated free carriers (electrons in particular) decays within ≈ 100 ps, which is accompanied by the emission of phonons (i.e., heating of the sample). This time corresponds to the rise time of the transient heating, while the holes are generated within the laser pulse duration, as schematically depicted in Fig. 3.15 (a). The non-equilibrium hole population decays within a nanonsecond time scale [**109**], as well as the excessive heat – Fig. 3.15 (b).

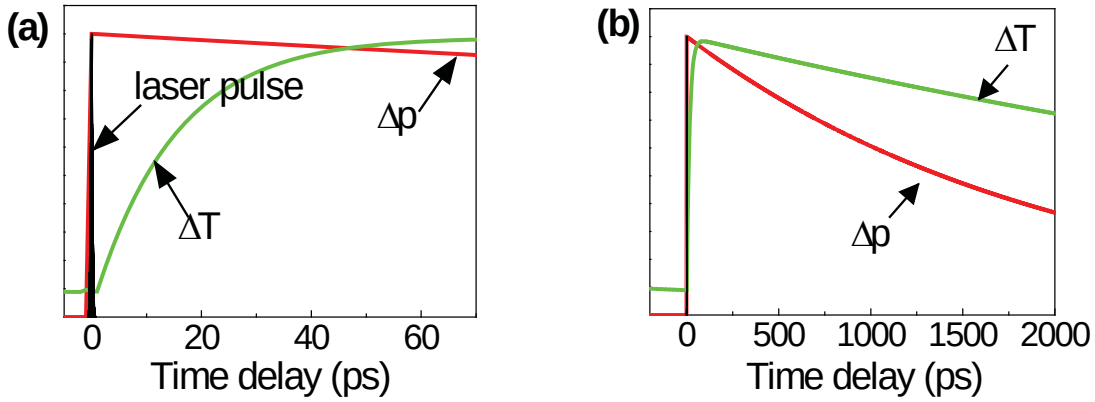

Fig. 3.15: Schematic depiction of the laser-pulse induced change of temperature (ΔT) and hole concentration (Δp) (a) on a time-scale shorter than the decay of photoinjected electrons (≈ 100 ps) (b) on a long time-scale.

The concentration of photoinjected holes Δp can be computed rather straightforwardly from the absorbed energy of laser pulses, if the absorption coefficient of a pure GaAs (15×10^3 cm^{-1}) is taken into account. The laser intensities used in our experiments range between $I_0 = 7\ \mu J.cm^{-2}$ and $30I_0 = 210\ \mu J.cm^{-2}$, and the corresponding laser-induced increase of the hole concentration varies between $\Delta p \approx 0.004 \times 10^{20}\ cm^{-3}$ and $30\Delta p \approx 0.12 \times 10^{20}\ cm^{-3}$. On the other hand, the transient heating of the sample ΔT is considerably more difficult to determine. The measured temperature and intensity dependences of ω, detected under the same experimental conditions, [Fig. 3.16 (a) and (b)] can be used for estimates of effective values of ΔT at various excitation intensities. As discussed above, when the sample temperature is increased the decrease of the anisotropy fields leads to the decrease of ω. Therefore, the measured intensity dependence of ω can be regarded as a consequence of sample heating. By careful comparison of these two dependencies we can deduce the overall laser-induced heating of the sample, which is depicted in Fig. 3.16. (b), assuming the base temperature (i.e. with no light) of $T_0 = 7\ K$. The intensity dependence of ΔT is very similar for all the investigated samples, which confirms the reliability of this procedure.

As a result, we found out that within the intensity range of our experiments, the laser-induced increase of the temperature (ΔT) ranges from $\Delta T_0 = 3\ K$ (for $I_0 = 7 \mu J.cm^{-2}$) to $\Delta T_0 = 17\ K$ (for $30I_0 = 210\ \mu J.cm^{-2}$).

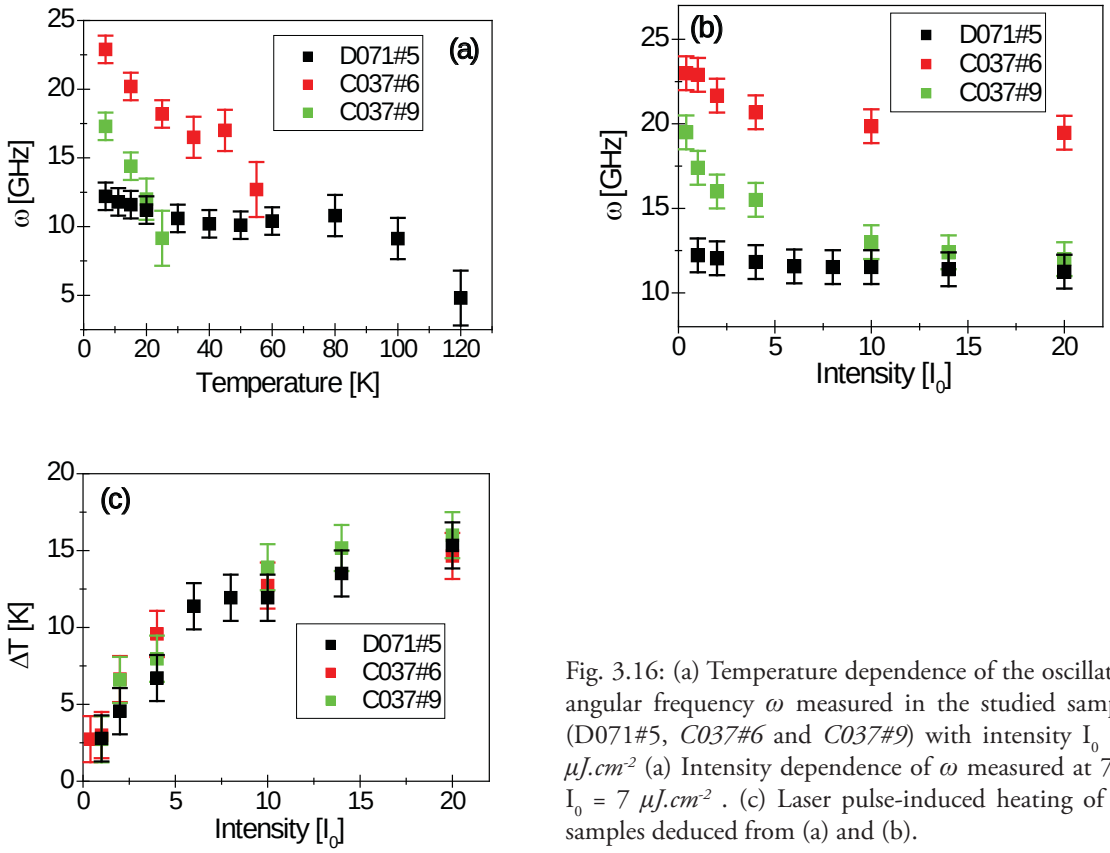

Fig. 3.16: (a) Temperature dependence of the oscillation angular frequency ω measured in the studied samples (D071#5, *C037#6* and *C037#9*) with intensity I_0 = 7 $\mu J.cm^{-2}$ (a) Intensity dependence of ω measured at 7 K, I_0 = 7 $\mu J.cm^{-2}$. (c) Laser pulse-induced heating of the samples deduced from (a) and (b).

The values of equilibrium hole concentration in the ferromagnetic (Ga,Mn)As samples with a nominal Mn concentration spanning from x_{nom} = *1.5%* up to *13%* (the "*optimized set*") cover a range of p_0 = *1.5…18x10*^{20} *cm*$^{-3}$ (see [**20**] – Supplementary material). Hence it immediately follows that the maximum relative change of the sample temperature achieved within our experimental limits is $\Delta T/T_0 \approx 200\,\%$, while the $\Delta p/p_0 \approx 8\,\%$ under the same conditions[5]. Consequently, the *thermal* origin of the magnetization precession typically prevails. However, we would like to point out that the laser-induced change of the hole concentration can under certain specific experimental conditions (i.e. strong excitation of the samples with low p_0) also trigger the magnetization precession, as demonstrated in Ref. [**120**].

In order to complete the picture of the observed phenomenon, it is necessary to address the optical aspects of the TRMO signal detected in our experiments. In the very beginning of this chapter we showed that the TRMO traces directly reflect the magnetization changes (Fig. 3.12). At the wavelengths used in the experiments, the penetration depth of the laser light (≈ 600 nm) is considerably larger than the thickness of majority of the samples (≈ 20 nm in the optimized set), and the carriers generated in the GaAs substrate can thus, in principle, contribute to the signal as well. The set of control experiments [**121**] showed that the oscillatory signal assigned to the magnetization precession comes solely from the (Ga,Mn)As epilayer.

In the TRMO experiments we aimed at studying the transient rotation of the polarization plane Δθ(t) (see Fig. 3.12). In (Ga,Mn)As there are two MO effects that are responsible for Δθ(t). The Polar Kerr effect (PKE), which is sensitive to the out-of-plane component of magnetization

[5] For example, in the sample D071#5 (p_0 = 7x10^{20} cm^{-3}) measured under typical conditions (I = 42 μJ.cm^{-2}, T_0 = 15 K), the $\Delta p/p_0 \approx 0.3\,\%$, while $\Delta T/T_0 \approx 85\%$.

M, and magnetic linear dichroism (MLD), which is sensitive to the in-plane component **M** (see **Chap. 1.4.2**). Relative strength of these effects is given by their MO coefficients P^{PKE} and P^{MLD}. The corresponding spectral dependence of the MO coefficients, measured in the sample *D071#5*, is presented in Fig. 3.17 (see ref. [**120**]).

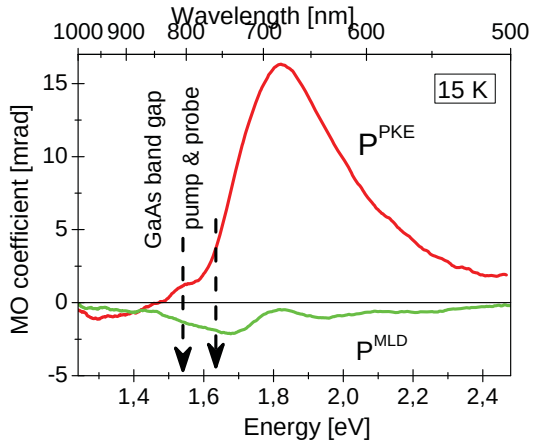

Fig. 3.17: Spectral dependence of magneto-optical coefficients P^{PKE} and P^{MLD} measured in the sample D071#5 at temperature 15 K; the vertical arrow shows schematically the spectral position of laser pulses used for the pump & probe experiment, and the position of the GaAs band gap at the relevant temperature (120)

In comparison, in Fig. 3.18 (a) we show TRMO traces detected at different wavelengths in the vicinity of the band gap of GaAs, and Fig. 3.18 (b) represents the corresponding spectral dependence of the precession amplitude *A*. From Fig. 3.17 it immediately follows that the MO coefficients have opposite signs in the relevant spectral range, and their magnitude increases with increasing excitation photon energy. For excitation energies above the GaAs band gap ($E^{pump}>E_g^{GaAs}$) the TRMO signal follows the same trend as the MO coefficients which indicates that the magnetization dynamics does not change significantly with the wavelength. However, for $E^{pump}<E_g^{GaAs}$ the TRMO signal amplitude drops sharply to zero, while P^{PKE} and P^{MLD} remain virtually constant. This observation is in accord with the mechanism leading to the magnetization precession as presented earlier that requires *absorption* of the laser light, and therefore becomes inefficient below the semiconductor band gap. The non-zero precession signal at λ = 815 nm (i.e. below GaAs bandgap: λ_{GaAs} = 805 nm) can be understood as resulting from the absorption of light on defects present due to the low-temperature growth mode of MBE.

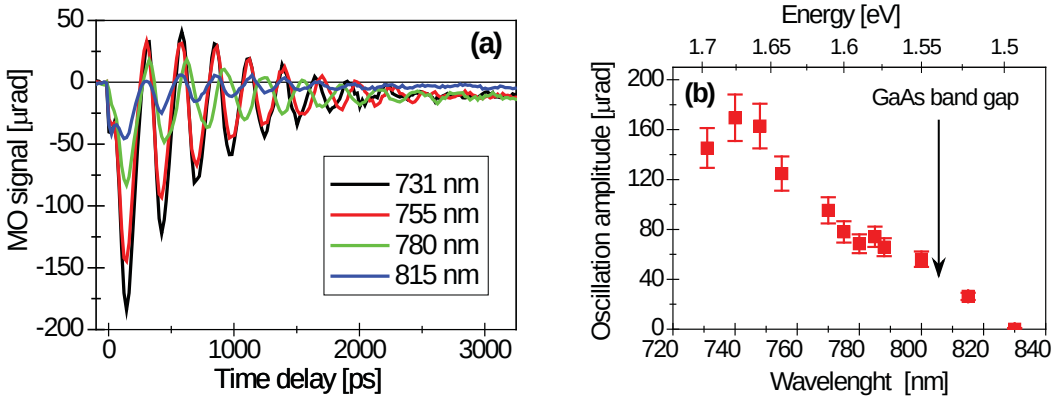

Fig. 3.18 : (a) Transient rotation of the polarization plane measured in the sample *D071#5* at different wavelengths at T = 15 K and (b) corresponding spectral dependence of the amplitude A of the oscillatory signal. Position of the GaAs band gap at T = 15 K is indicated by an arrow. The magnetic field was $\mu_0 H_{ext}$ = 10 mT, pump fluence I = 21 µJ.cm^{-2}, probe polarization along [100] direction.

Due to the fact that the MO coefficients of PKE and MLD are comparable, the MO measurement provides information about both in-plane and out-of-plane components of magnetization **M**. In the near-perpendicular incidence geometry used in our experiments the PKE, sensitive to the out-of-plane projection **M**, is independent of the linear polarization of the probe pulses chosen for the detection. On the other hand, MLD, sensitive to the in-plane component of **M**, has to vary with the angle between polarization plane and magnetization (**Chap. 1.4.2**). In Fig. 3.19 (a), the TRMO traces detected with different polarization of the probe light are depicted, and in Fig. 3.19 (b), the amplitudes of the corresponding oscillatory part (*A*) and time-dependent background (*C*) are presented as a function of the polarization angle β taken from the [100] direction. Clearly, the oscillatory part of the signal contains both the probe polarization-dependent and polarization-independent parts, and it is connected with both in-plane and out-of-plane projections of the magnetization precession, as expected. Moreover, the amplitude *C* varies significantly with *β* which indicates that the time-dependent background is connected with a non-oscillatory change of magnetization *in the sample plane*.

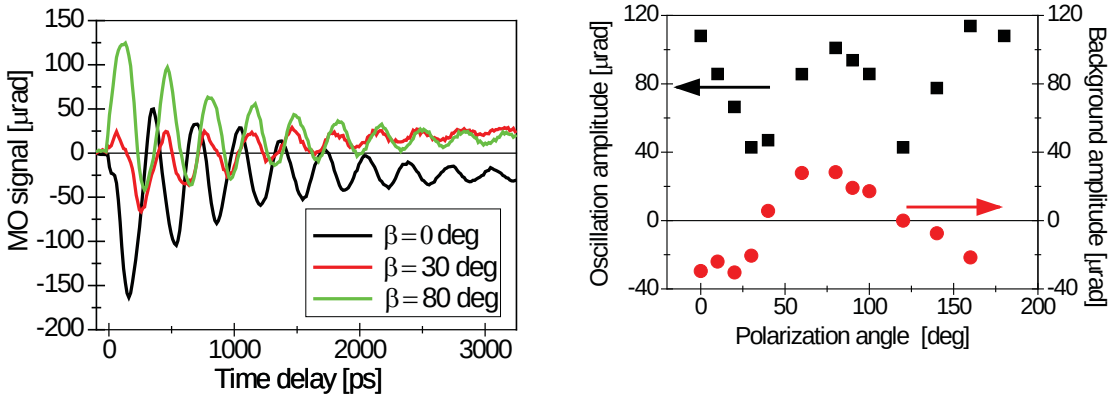

Fig. 3.19 : (a) Transient rotation of the polarization plane measured in the sample *D071#5* with different probe beam polarization angles *β* and (b) corresponding dependence of the oscillation amplitude *A(β)* and background amplitude *C(β)*. The magnetic field $\mu_0 H_{ext}$ = 10 mT, T = 15 K, I = 21 μJ.cm^{-2}

3.3.3 Conclusion

In this chapter we showed experimentally that the time-resolved magnetooptical signal reflects a laser-induced magnetization precession. Due to the contribution of two different MO effects (PKE and MLD), the detected TRMO trace provides information about the motion of magnetization both in plane and out of the sample plane. The most probable origin of the precession is a change of the sample anisotropy triggered by a transient heating by the laser pulses.

3.4 Our model of a helicity-independent signal

Here we present our model of the time-resolved magnetooptical (TRMO) signals detected in the (Ga,Mn)As due to the pump-helicity independent phenomena. Our understanding of the signal is based on the observations described in the previous chapter. However, a much more extensive work was performed on an "optimized set" of (Ga,Mn)As samples [**120**], which is covering a whole range of Mn doping. The corresponding experiments exceed the scope of this thesis and they will be published elsewhere [**122**].

The description of the helicity-independent magnetization precession is based on pump-pulse induced changes of the magnetic anisotropy. Under equilibrium conditions and with no external magnetic field $\boldsymbol{H}_{ext}$ applied, the magnetization $\boldsymbol{M}$ is aligned with the easy axis see Fig. 3.20 (a). The absorption of a laser pulse leads to photoinjection of electron (Δn) and hole (Δp) populations. The subsequent fast (≈ 30 ps) non-radiative recombination of Δn results in a transient increase of temperature ΔT [see Fig. 3.15 (a)]. Both changes in ΔT and Δp cause a reorientation of the easy axis (EA). The magnetization is forced to precess around the new quasi-equilibrium EA – see Fig. 3.20 (b). As the EA returns adiabatically to its former state due to the decay of the excess holes Δp and cooling of the sample [see Fig. 3.15 (b)], the magnetization follows its local position – see Fig. 3.20 (c). The overall trajectory of $\boldsymbol{M}$ therefore consists of two parts – precessional motion and in-plane shift.

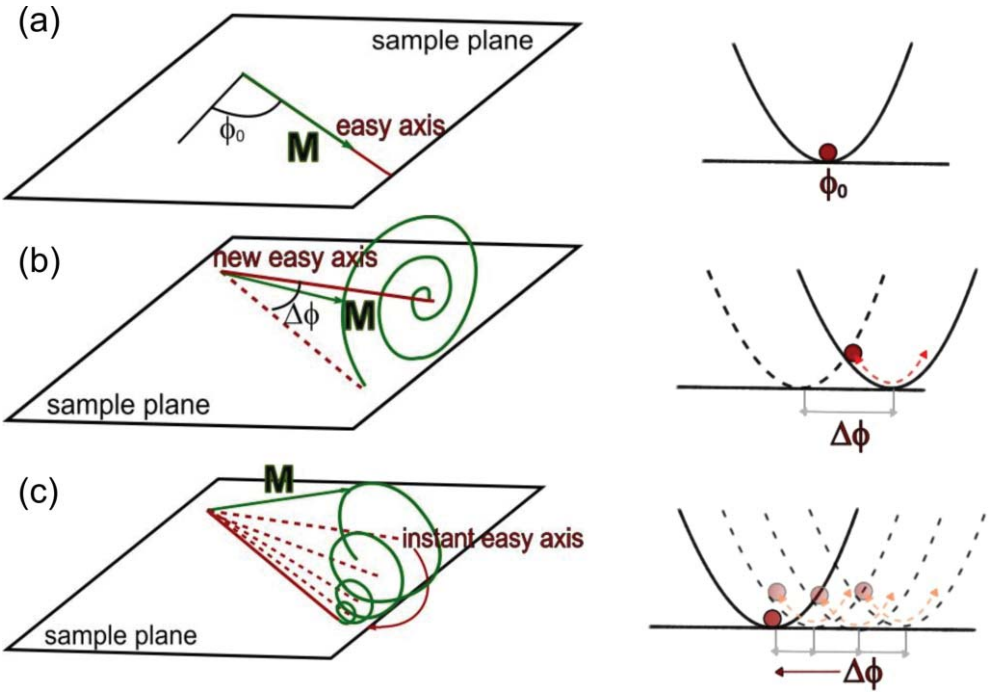

Fig. 3.20: Schematic illustration of the helicity-independent laser pulse-induced precession of magnetization. (a) In equilibrium, the magnetization is oriented along the easy axis at an azimuthal angle $\varphi_{0,}$ which is reoriented by an angle $\Delta\varphi$ after the impact of the laser pulse (b) The magnetization starts to precess around a new quasi-equilibrium easy axis that slowly returns to its former position (c).

Let us now briefly mention the conditions under which the precession can be observed. Clearly, the position of the easy axis (EA) has to be sensitive to small changes ΔT, Δp – in other words, competition among individual contributions to the free energy F [Eq. (3.9)] has to exist which leads to an "instability" of the EA. The precession is therefore not observed in the samples where uniaxial or cubic anisotropy dominates (see [**119**], [**120**]). Even in the samples where the oscillations are typically quite pronounced, such as *D071#5* described in the previous chapter, their amplitude can be manipulated by varying the ratio between the individual contributions to F. This can be done by changing external conditions, such as temperature or external magnetic field, which "stabilizes" or "destabilizes" the EA position. As an example, in Fig. 3.21 the amplitude of the oscillatory signal ascribed to the magnetization precession is depicted as a function of $\boldsymbol{H}_{ext}$ applied in two different crystallographic directions – [110] near the hard axis, and [010] closer to the easy axis. The field $\boldsymbol{H}_{ext}$ acts as an additional uniaxial anisotropy, which

in one case ([010]) helps to "stabilize" the EA thus quenching the oscillations, while in the other case ([110]) the "destabilization" results in amplification of the precession. More details can be found in [**119**]. Here we would like only to present the importance of the EA "stability" with respect to the magnetization precession which will be crucial for the analysis of the signal observed in the hybrid piezo/(Ga,Mn)As structures (see **Chap. 3.7**).

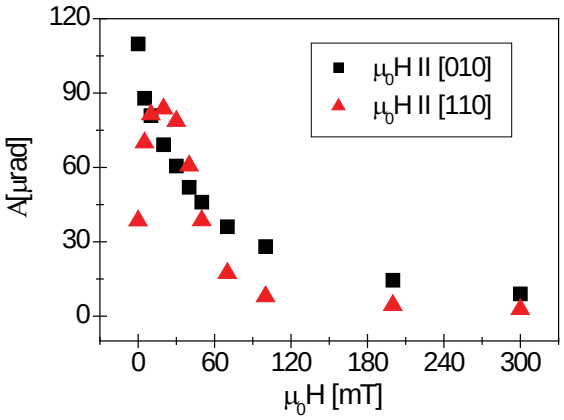

Fig. 3.21: Amplitude of the oscillations as a function of the external magnetic field Hext, extracted from the TRMO signal detected at T = 15 K in the sample D071#5. The field was applied along [010] and [100] directions, and the probe beam polarization was oriented at β = 0°

The above-described process of laser-induced magnetization precession manifests as an oscillatory signal in the TRMO measurements, as was shown experimentally in the Chap. 3.3. From the magnetooptical (MO) point of view, there are two effects responsible for the detected rotation of the polarization plane ($\Delta\beta$) in (Ga,Mn)As in the near-normal incidence geometry of the beams (see **Chap. 1.4.2**) – *polar Kerr effect (PKE)*, where the rotation of probe beam polarization $\Delta\beta$ is proportional to the projection of magnetization ***M*** to the direction of light propagation, and *magnetic linear dichroism (MLD),* which occurs when the light propagates perpendicular to the direction of ***M.*** The important difference between these two MO effects lies in their symmetry with respect to ***M.*** While *MLD* is linear in magnetization (i.e., the sign of $\Delta\beta^{MLD}$ is changed when the direction of ***M*** is reversed), the value of $\Delta\beta^{PKE}$ due to *PKE* does not dependent on the initial probe beam polarization β. Hence two conclusions directly follow. First, our detected TRMO trace contains information about both in-plane and out-of-plane motion of ***M.*** Second, these two parts of the magnetization dynamics can be separated by the probe-beam polarization dependence of the corresponding parts of the TRMO signal.

The measured TRMO trace, $\delta MO(t)$, can be fitted well by the phenomenological Eq. (3.21). We remind that there are two terms in Eq. (3.21) – a damped harmonic function with amplitude A and a pulse-like function with amplitude C. These two signal components can be directly related to the magnetization motion by their probe beam polarization β dependence. The following expressions describe the corresponding $A(\beta)$ and $C(\beta)$ dependences ([**125**] – Supplementary material). The definition of the coordinate given in Fig. 3.22 is used in these relations.

$$A(\beta) = \sqrt{\left[\delta\varphi\, P^{MLD}\, 2\cos 2\left(\varphi_M - \beta\right)\right]^2 + \left[\delta\theta \cdot P^{PKE}\right]^2} \tag{3.23}$$

$$C(\beta) = -\delta\theta\, P^{PKE} + \delta\varphi\, P^{MLD}\, 2\cos 2\left(\varphi_M - \beta\right) - \delta p\, P^{MLD}\, \sin 2\left(\varphi_M - \beta\right) \tag{3.24}$$

Here $\delta\varphi$ and $\delta\theta$ represent the in-plane and out-of-plane tilt of the magnetization ***M*** from the quasi-equilibrium position of the easy axis φ_M. Furthermore, P^{MLD} and P^{PKE} denote the

corresponding MLD and PKE magnetooptical coefficients, and the parameter δp describes a reduction of the magnitude of $\boldsymbol{M}$ due to the laser-induced *demagnetization* [**25**].

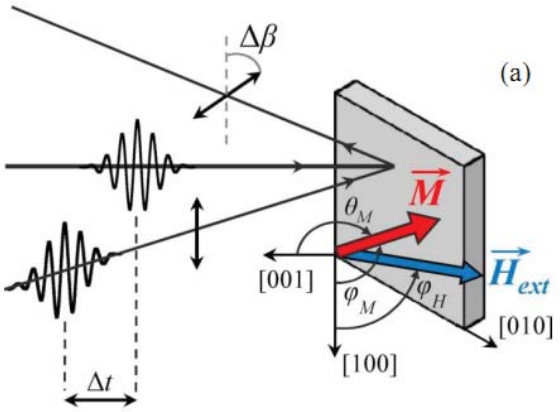

Fig. 3.22: The coordinate system used in the experiments. The orientation of magnetization in the sample is described by the polar angle φ_M and azimuthal angle θ_M. The external magnetic field H_{ext} is applied in the sample plane at an angle φ_H. The rotation of the polarization plane of the probe beam is denoted as $\Delta\beta$. From Ref. [120].

Detailed derivation of the relations is beyond the scope of this work and it will be published elsewhere [**126**]. Here we only point out some of the important conclusions. Equations (3.23) and (3.24) can be used to fit the measured dependences $A(\beta)$ and $C(\beta)$, respectively. As an input to the fitting procedure we take the *independently measured* values of the MO constant P^{PKE} and P^{MLD} that can be directly obtained from static MO experiments [**126**].[6] This is an important difference to the procedures used in other works where the MO constants are taken as fitting parameters (see Ref. [**109**] for comparison). Consequently, by the simultaneous fitting of $A(\beta)$ and $C(\beta)$ we can determine the magnitude and the sign of the easy axis tilt $\delta\varphi$, and also the position of the magnetization φ_M under the quasi-equilibrium conditions that corresponds to the maximum in the dependence $A(\beta)$ [see Eq.(3.23)]. These parameters are crucial for the reconstruction of the real magnetization motion by simultaneous fitting and modeling by the Landau-Lifshitz-Gilbert equation [Eq. 3.14(a)-(c)]. This modeling procedure is presented in [**125**] and it was successfully used for the helicity-independent TRMO signals detected on a whole range of samples from the "optimized set". In addition, it was also extended to account for the helicity-dependent TRMO traces that will be discussed in Chap.3.8.

3.5 Spin-wave resonances in MO signal of (Ga,Mn)As

In the previous sections we were dealing with a spatially uniform magnetization precession. But the precession amplitude can vary also as a function of the position in thin-film magnets, and consequently magnetic excitations with a nonzero wave vector k, so called *spin waves* (SWs) or *magnons,* are generated. These SW modes are typically studied by the ferromagnetic resonance (FMR), where the resonantly amplified SW modes – spin wave resonances (SWRs) – are detected as the multiple absorption peaks (See Chap. 3.2.1 and 3.2.3 for results in (Ga,Mn)As). The SWRs were detected also by a time-resolved magnetooptics where they manifest themselves as additional harmonic components in the oscillatory signal [**83**]. In (Ga,Mn)As, a presence of SWRs in the TRMO signal has so far been reported only by Wang et al. [**113**], [**127**]. In this chapter we would like to show that the study of SWRs in the optical signal provides important information about the sample homogeneity and more importantly, they also represent a tool for the exact estimation of the crucial micromagnetic parameter *spin stiffness*.

[6] This procedure was used also for obtaining the MO spectra presented in the previous chapter in Fig. 3.17.

3.5.1 Spin wave resonances in (Ga,Mn)As

Before we present the experimental results obtained in the different (Ga,Mn)As layers, let us briefly discuss the origin and phenomenology of the spin wave resonances (SWRs) in this material. As already described in the introduction, SWRs are usually detected as multiple absorption peaks in the FMR spectra. In order to obtain the corresponding resonant fields for the *n*-th mode (H_n), the Landau-Lifsitz-Gilbert (LLG) equation with a term corresponding to exchange interactions has to be solved and the appropriate boundary conditions have to be considered (see **Chap. 3.2.1**). As a solution in *homogeneous thin films* of thickness *L,* the modes fulfilling a resonant condition $kL = n\pi$ are obtained. Depending on the exact form of the boundary conditions, two major types of these modes can occur (see Fig. 3.23). If the precession is "frozen" at the film interfaces, the Kittel type [**85**] of SWRs is generated [Fig. 3.23 (a)]. On the other hand, "free" motion of magnetization at the boundaries results in perpendicular standing SWs (PSSWs) [**83**] depicted in Fig. 3.23 (b). Though it is not possible to reliably distinguish these two SWR types from our experiments, the n = 0 mode always corresponds to the uniform precession described in the previous chapters. The position of the *n*-th SWR mode in the FMR spectrum H_n with respect to the uniform resonance field H_0 is given by the Kitell relation [**85**], [**105**]:

$$\Delta H_n \equiv H_0 - H_n = n^2 \frac{D}{g\mu_B}\frac{\pi^2}{L^2} \tag{3.25}$$

where n is an integer mode number, D denotes the exchange spin stiffness constant, μ_B the Bohr magneton, g the g-factor, and L stands for the sample thickness.

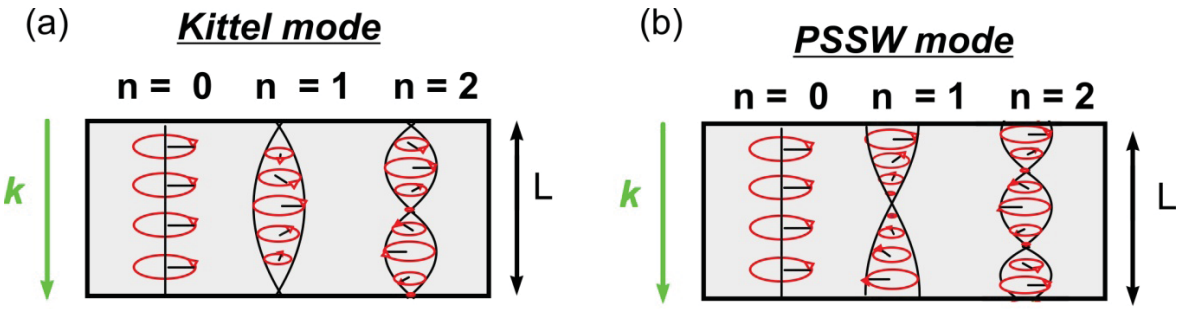

Fig. 3.23: Schematic representation of the spin-wave (SW) resonance modes with the wave vector ***k*** in magnetically homogeneous films with (a) fixed boundary conditions for magnetization motion – *Kittel mode* and (b) open boundary conditions – perpendicular standing SW modes (PSSW). The local phase and amplitude of the dynamical magnetization is marked.

For a magnetically *inhomogeneous film*, a spatial variation of the magnetic anisotropy and/or of the magnetization magnitude has to be taken into account. The solution of the LLG equation is different, as well as the positions of SWRs. For example for the parabolic profile of the bulk inhomogeneity in the growth direction *z,* the spacing of the modes becomes linear [**85**], [**101**]:

$$\Delta H_n = \left(n - \frac{1}{2}\right)\frac{4}{L}\sqrt{4\pi M_{eff}^{0}\varepsilon\frac{D}{g\mu_B}} \tag{3.26}$$

where ε is the distortion parameter of the film and $4\pi M^0_{eff}$ corresponds to the magnetic properties in the sample center ($z = 0$).

In the previous chapter we have shown that the precession of magnetization is described by the LLG equation. For the external magnetic field H_{ext} applied in the sample plane, the angular frequency of the n-th SWR mode ω_n is given by [**68**], [**113**][7]:

$$\omega_n = \gamma \sqrt{\left[H_{ext}\cos(\varphi-\varphi_H) + 4\pi M^0_{eff} + H_{4\parallel}\frac{3+\cos(4\varphi)}{4} + H_{2\parallel}\sin^2\left(\varphi-\frac{\pi}{4}\right) + \Delta H_n \right] \times \left[H_{ext}\cos(\varphi-\varphi_H) + H_{4\parallel}\cos(4\varphi) - H_{2\parallel}\cos\left(2\varphi-\frac{\pi}{2}\right) + \Delta H_n \right]} \tag{3.27}$$

where γ is the gyromagnetic ratio, φ_H and φ are the azimuthal angles that describe the positions of H_{ext} and M (see Fig. 3.22), $4\pi M^0_{eff} = 4\pi M - H_{2\perp}$ (where $4\pi M$ represents the shape anisotropy), and $H_{4\parallel}$, $H_{2\parallel}$ and $H_{2\perp}$ are the corresponding FMR anisotropy constants (see Eq. 3.9 (b) for definition). Note that in FMR, the corresponding fields $H_n < H_0$ (unless the surface evanescent mode is observed – see ref. [**85**]). On the other hand, the external magnetic field is kept constant during the measurement of any dynamical MO trace. Consequently, the SWRs are apparent as additional *frequencies* in the oscillatory signal that are *larger* than that of the uniform magnetization precession.

3.5.2 Samples and experimental details

The majority of the results presented in this chapter were measured on the two distinct types of samples, described in the **Chapter 3.3.1**. The first type is represented by the 500 nm thick layers (*C037#6, C037#9*), where bulk magnetic inhomogeneity is expected. The second type are the "optimized thin samples", where the 50 nm thick layer *D071#5* belongs as well.

Nominal thickness of the layers, which is a crucial parameter for the SWR study, was controlled by the growth time; typical inaccuracy of this nominal value is +/-3%. In a short time after exposing the layer to the atmosphere a native oxide arises which reduces the epitaxial film thickness, and further oxidation takes place during the sample annealing. Based on the controlled oxidation and annealing experiments [**69**] one can expect that the most probable total loss of the active layer thickness is 2.5 nm, with a systematic uncertainty of +/-1 nm equal for all samples.

In addition to the simple (Ga,Mn)As epilayers, we investigated also a step-like structure prepared from the sample *D071#5* by optical lithography and wet etching – see Fig. 3.24. The steps "height" of the 50 nm to 39, 29 and 15 nm was measured by a STM profile meter with the precision of +/- 1.5 nm, and the layer thickness L is the only parameter that varies among the individual "steps".

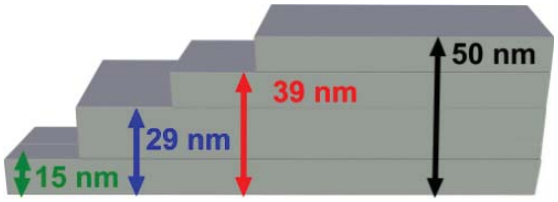

Fig. 3.24.: Schematic illustration of the step-like structure prepared by a wet etching from the sample D071#5.

[7] In this chapter we used the free energy functional F in the common FMR notation in order to maintain compatibility with the previously published results obtained by the FMR technique.

The experiments were carried out by the standard TRMO method under similar conditions as those used in the basic magnetization precession experiments (i.e. fluence of pump pulses was 42 μJ. cm^{-2}, wavelength 770 nm, temperature 15 K). The TRMO data reported here correspond again to the polarization-independent part of the pump-induced rotation of probe polarization, which was computed by averaging the signals obtained for the opposite helicities of circularly polarized pump pulses. Penetration depth of the laser (≈ 600 nm) was larger than the thickness of all the (Ga,Mn)As epilayers. The external magnetic field H_{ext} ranging from ≈ 0 mT (i.e., smaller than 50 μT) to 550 mT was applied in the sample plane along [010] or [110] crystallographic directions.

3.5.3 Influence of magnetic homogeneity

In the previous chapters we described in detail how laser pulses trigger the uniform magnetization precession which is detected as an oscillatory TRMO signal. In Fig. 3.25 we present such a TRMO trace of as-grown *C037#9* (a) and annealed *C037#6* (b) samples of the same thickness (500 nm), with $\mu_0 H_{ext} = 10\ mT$ applied in the [010] direction. In the annealed sample, the improved magnetic quality leads to a strong suppression of the magnetization precession damping with respect to that observed in the as-grown sample ($\tau_D \approx 210$ ps and $\tau_D \approx 460$ ps for the annealed and as-grown samples) – note the different timescales of Fig.3.25 (a) and (b). On the other hand, the anisotropy reflected in the precession frequency is less affected.

In the presence of SWRs, the TRMO trace contains more harmonic components, and thus it is described by a superposition of harmonic functions:

$$MO(t) = \sum A_n \cdot \cos(\omega_n \cdot t + \Delta_n) \cdot \exp\left(-\frac{t}{\tau_{Dn}}\right) + C\left[1 - \exp\left(\frac{t}{\tau_1}\right)\right]\exp\left(-\frac{t}{\tau_2}\right) \qquad (3.28)$$

where A_n, ω_n, Δ_n and τ_{Dn} describe the amplitude, frequency, phase and damping time for the individual precession modes (with n = 0, 1, ...), and C and τ_1, τ_2 are the amplitude, rise and damping time of the background. The lower panels of Fig. 3.25 (a) and (b) show a decomposition of the TRMO traces into individual components according to Eq. (3.28). It is apparent that the sample annealing not only decreases damping but also leads to a considerable increase of the number of SWR modes observed in the TRMO signal.

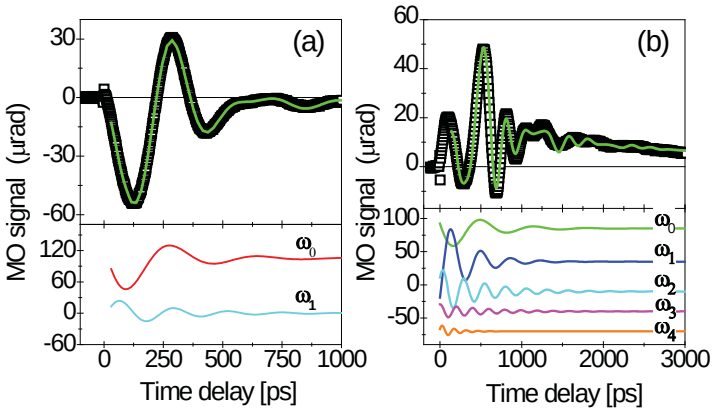

Fig. 3.25.: Time-resolved magneto-optical (MO) signals (points) measured in as-grown (a) and annealed (b) sample *C037*; note the different *x*-scales in (a) and (b). The lines in the upper parts of the figures are fits by Eq. (3.28) and the corresponding precession modes are plotted in the lower parts of the figures.
External magnetic field of 10 mT was applied in the [010] crystallographic direction, probe pulses were linearly polarized along [010].

In Fig. 3.26(a) we show the fast Fourrier transform (FFT) of the oscillatory TRMO signal that was measured in the annealed sample C037. The FFT spectrum can be fitted by a sum of five Lorentzian peaks and the corresponding frequencies ω_n depend linearly on the mode number [see Fig. 3.26(b)]. If we take into account that ω_n is approximately a linear function of H_n [cf. Eq. (3.27)], this result clearly shows that this annealed epilayer is not magnetically homogeneous [Eq. (3.26)]. Recently, it was reported by H. Son *et al.* that there exists a sizable vertical gradient of the magnetic anisotropy in their as-grown (Ga,Mn)As sample with x = 5% and L = 480 nm, which was attributed to the fluctuation of Mn composition and carrier density along the growth direction [**123**]. From our experience, this inhomogeneity of magnetic properties could not be avoided for films with a thickness of more than ≈ 100 nm, and the annealing can also lead to a more pronounced vertical gradient of magnetic properties than in the as-grown films (see **Chap. 3.1.4**), which is reflected by the measured non-quadratic spacing of SWRs.

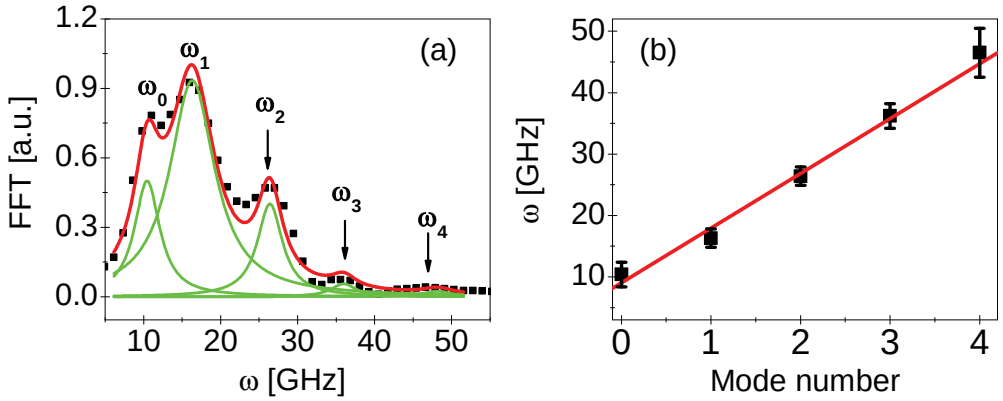

Fig. 3.26.: (a) Fourier spectrum of the oscillatory part of the MO signal measured in the annealed sample (points) that was presented in Fig. 3.25; the line is a fit by a sum of Lorentzian peaks and the arrows indicate positions of the peak frequencies, which are plotted in (b) as a function of the mode number together with a linear fit.

3.5.3 Magnetically homogeneous samples and spin stiffness

Let us now turn to the results obtained on the 50 nm sample D071 that are depicted in Fig. 3.27. We identified three frequencies in the TRMO signal [see inset of Fig. 3.27 (a)], whose relative amplitude depends strongly on the orientation of the probe beam linear polarization [see the lower panel in Fig. 3.27 (a)]. This phenomenon will be discussed in detail in the next chapter.

In Fig. 3.27 (b) we show the dependence of the precession frequencies ω_0, ω_1 and ω_2 on H_{ext} for two different orientations of H_{ext}. For a sufficiently high H_{ext}, which is about 70 mT in this sample, the quasi-equilibrium position of magnetization is oriented in the direction of H_{ext} (i.e., $\varphi = \varphi_H$) and Eq. (3.27) can be used to fit the data. We note that all the six measured dependences $\omega_n = \omega_n (H_{ext}, \varphi_H)$ (where n = 0; 1; 2 and φ_H = 45°; 90°) can be fitted well with a single set of constants: γ = 2.2 x 10^5 $mA^{-1}s^{-1}$ (g-factor of 2), $\mu_0 H_{2\|}$ = 13 ± 2 mT, $\mu_0 H_{4\|}$ = 15 ± 2 mT, $\mu_0 4\pi M^0_{eff}$ = 440 ± 20 mT, $\mu_0 \Delta H_1$ = 90 ± 10 mT and $\mu_0 \Delta H_2$ = 350 ± 15 mT, which confirms the credibility of this fitting procedure. The $\omega_n = \omega_n (H_{ext})$ relations enable us to convert the observed frequency spacing of individual SWRs to the field differences ΔH_n. In Fig.3.27 (c) we show that in this 50 nm thick epilayer ΔH_n depend linearly on n^2 as expected for a homogeneous film. From the slope of this dependence we can determine the value of the exchange spin stiffness D [see Eq. (3.25)].

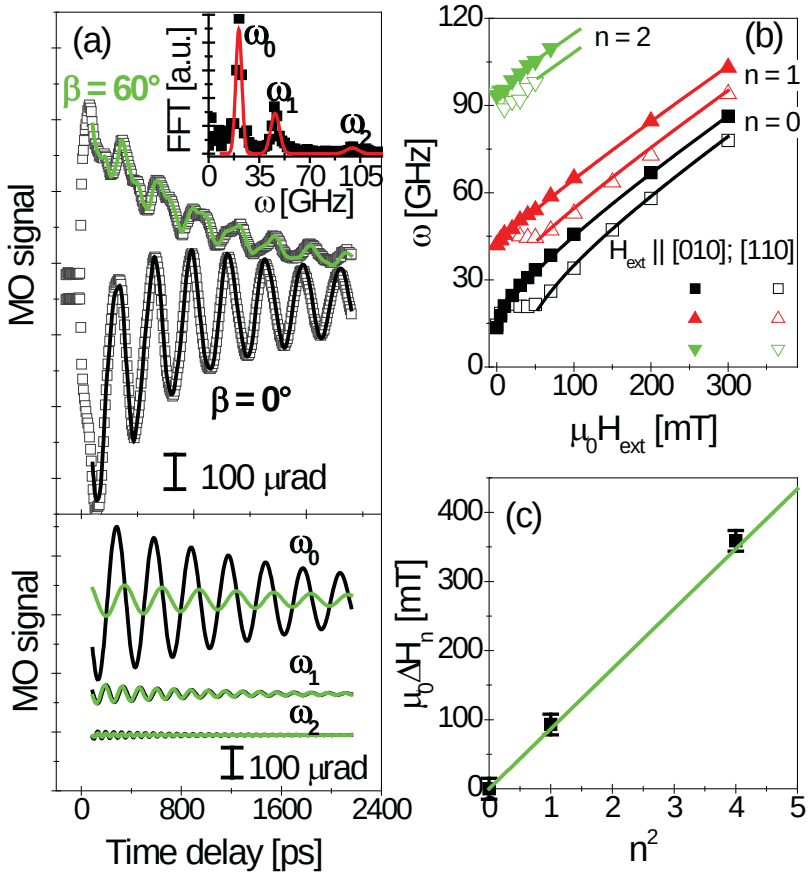

Fig. 3.27.: (a) TRMO signal measured in 50 nm thick sample D071 (points) for two different probe beam linear polarizations *(β)* at external magnetic field $\mu_0 H_{ext}$ = 20 mT applied in the [010] direction; the curves are vertically shifted for clarity. The lines in the upper part of the figure are fits by Eq. (3.28) and the corresponding components are plotted in the lower part of the figure. Inset: Fourier spectrum of the oscillatory part of the MO signal measured for β = 60° (points); the line is a fit by a sum of Lorentzian peaks. (b) Dependence of the precession frequency ω_n on H_{ext} for two different orientations of the field (points), lines are fits by Eq. (3.27) (c) Dependence of mode spacing ΔH_n on n^2 (points); the line is a fit by Eq. (3.25) with $D = 2.55$ *meV.nm*^{2}.

The homogeneous properties of this epilayer were further confirmed by additional experiments performed on the step-like structure that was prepared from the 50 nm sample (see Fig. 3.24). The selected TRMO signals measured in the individual "steps" are presented in Fig. 3.28 (a) and in Fig. 3.28 (b) the corresponding FFT spectra are displayed. Clearly, the frequency ω_0 of the lowest SWR does not depend on the film thickness. This means that the lowest observed SWR is indeed the uniform precession of magnetization and, moreover, that this particular film is magnetically homogeneous. The spacing ΔH_1 shows the expected [see Eq. (3.25)] linear dependence on $1/L^2$ [Fig. 3.28 (c)] from which the value of D can be again obtained. Both the above described methods of experimental evaluation of D [i.e, the mutual SWR spacing – Fig. 3.27(c) and its dependence on the film thickness – Fig. 3.28(c)] give the same value $D = 2.55 \pm 0.10$ *meV.nm*^{2}.

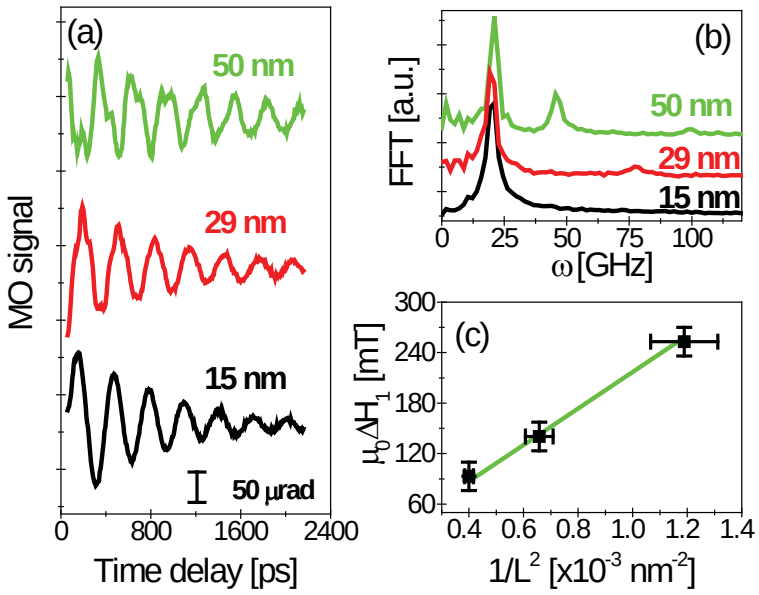

Fig. 3.28.: (a) Oscillatory parts of MO signals measured in a sample prepared by etching from sample D071; the curves are labeled by the film thicknesses L and are vertically shifted for clarity. External magnetic field $\mu_0 H_{ext}$ = 20 mT was applied along the [010] direction (b) Fourier spectra of the MO signals shown in (a). (c) Dependence of the spacing between the two lowest modes (ΔH_1) on the film thickness (points), the line is a fit by Eq. 3.35 with D = 2.55 meV.nm^2.

Finally, we note that the above described procedure provides a powerful method to determine the spin stiffness constant rather precisely from the TRMO experiment and it can be used to extract this crucial parameter for a whole range of samples with different Mn content. The corresponding experimental results will be published in [**126**].

3.5.4 Spatio-temporal evolution of the SWR modes

In **Chap. 3.4** we explained how the presence of the two MO effects – PKE and MLD – reflects in the probe polarization dependence of the precession amplitude, namely that the polarization-dependent part of the signal (sensed by MLD) corresponds to the in-plane motion of magnetization, while the polarization-independent part (sensed by PKE) is connected with the out-of-plane motion. Here we would like to address the spatio-temporal evolution of the magnetization in the presence of SWR modes. We detected a dependence of the TRMO signals in the 50 nm sample D071 at H_{ext} = *40 mT* on the probe polarization angle β, and the corresponding precession amplitudes of the first two SWR modes (A_0 and A_1) are depicted in Fig. 3.29 (a). The corresponding MO coefficients of PKE and MLD are 4.1 mrad and -1.6 mrad, respectively. In Fig. 3.29 (b) we show the amplitude A_0 and A_1 as a function of H_{ext} applied in [110] and [010] directions.

The strong dependence of the amplitude A_0 on β apparent in Fig. 3.29 (a) is a clear signature that in this sample the uniform precession of magnetization leads to a larger time-dependent change of the in-plane component of magnetization than that of the out-of-plane component. The magnetization trajectory in the sample is given by its magnetic anisotropy. Larger in-plane tilt is fully in accord with the smaller in-plane anisotropy constants ($H_{2\|}$ and $H_{4\|}$) compared to the out-of-plane anisotropy ($4\pi M_0^{eff}$), and the strong dependence of A_0 on the direction of $\boldsymbol{H_{ext}}$

also confirms this conjecture (see **Chap. 3.4**). The corresponding magnetization trajectory is schematically depicted in Fig. 3.30, upper part.

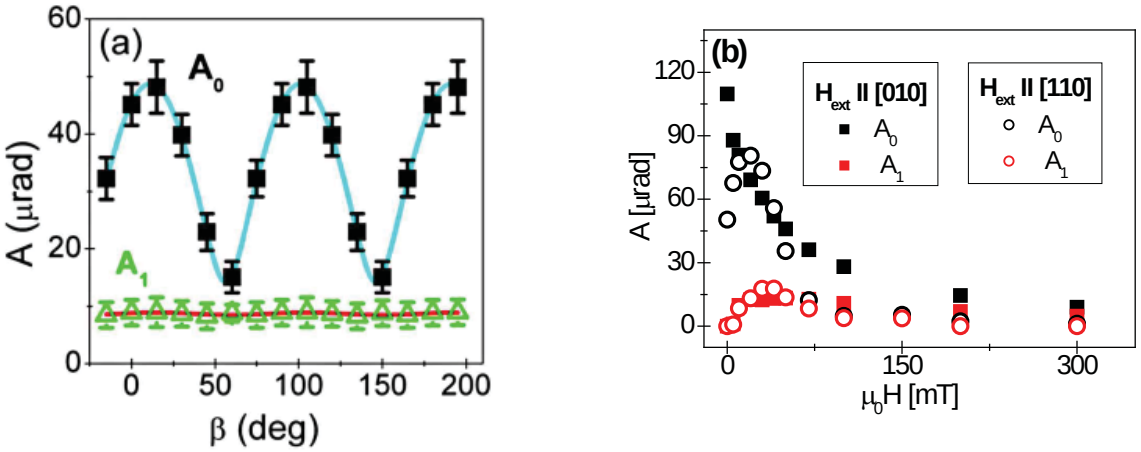

Fig. 3.29: (a) Dependence of the precession amplitude An on the probe-polarization orientation (β) for modes with n = 0 and 1 measured in sample D071 (points); the lines represent a harmonic function of β (see Chap. 3.4). External magnetic field $\mu_0 H_{ext}$ = 40 mT was applied in the [010] direction. (b) Dependence of the precession amplitude An on the external magnetic field Hext applied along [010] and [100] directions for modes with n = 0 (black symbols) and 1(red symbols) ; The probe beam polarization was oriented along [100] direction.

The situation is markedly different for the higher SWR mode where the dependence of amplitude A_1 on β was found to be much weaker [see Fig. 3.29(a)]. Therefore, for this precession mode the change of the out-of-plane component of the magnetization is comparable to that of the in-plane component, as is schematically shown in the lower part of Fig. 3.29(b). This experimental observation can be qualitatively explained as follows. The exchange interaction, which is described by the exchange energy associated with the twist of the spins, leads to the energy difference between the spatially uniform precession and the SWR mode with n = 1 [see Eq. (3.25)]. This term can be viewed as an additional magnetic anisotropy in the sample that acts both in the in-plane and in the out-of-plane directions [see Eq. (3.27)]. Consequently, the relative enhancement of the in-plane anisotropy is considerably stronger than that of the out-of-plane anisotropy. This in turn suppresses the in-plane movement of magnetization more than that in the out-of-plane direction (see lower part of Fig. 3.30). This is also in accord with the fact that the precession amplitude A_1 of the n= 1 mode depends only weakly on the direction of the external magnetic field applied during the experiment [see Fig. 3.29 (b)].

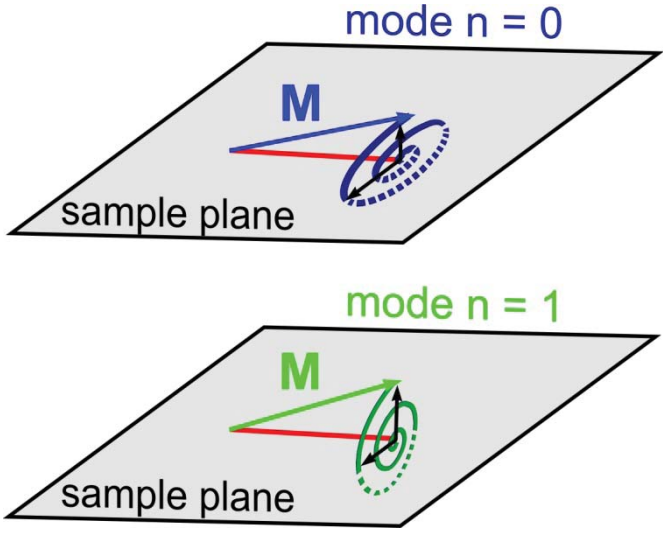

Fig. 3.30: Schematic illustration of the magnetization precession in the two SWR modes (n = 0,1) – the overall magnetization dynamics is a superposition of several precession modes from which the lowest two are shown in the upper and lower parts of this figure, respectively; the depicted tilt of magnetization is highly exaggerated for clarity and also the relative magnitude of these two modes is not to scale

3.5.5 Conclusions

In conclusion, we observed spin-wave resonances in time-resolved magneto-optical signals in several (Ga,Mn)As samples. We illustrated that the mutual spacing between SWRs can be used to discriminate between magnetically homogeneous and inhomogeneous samples. We also determined the value of the spin-wave exchange stiffness constant in the magnetically homogeneous sample from the TRMO experiments, which represent a powerful tool to precisely determine this important micromagnetic parameter. In addition, we demonstrated that the probe-polarization dependence of the measured TRMO signals can be used for a reconstruction of the magnetization spatio-temporal evolution.

3.6 All-optical coherent control of magnetization precession in (Ga,Mn)As

In this chapter we present a scheme that leads to controlling the magnetization precession described in the previous sections. In the all-optical experiment the sample is excited by pairs of pump pulses. Each pump pulse generates a transient precession of magnetization vector and their temporal separation (i.e., the mutual phase difference between the corresponding magnetization precessions) determines if they superimpose constructively or destructively. The all-optical control has so far been demonstrated in a variety of materials [**30**], [**26**], [**126**] and it is a straightforward path to follow also in (Ga,Mn)As [**114**].

3.6.1 Experimental

Our measurements were performed on the annealed sample D071 ($x = 7\%$, $T_c = 160\ K$ – see **Chap. 3.3.1**) in the double-pump extension of a standard pump-probe experimental setup – see Fig. 2.1. (b). The external magnetic field of $\mu_0 H_{ext} = 10\ mT$ was applied in the [010] direction and linear polarization of the probe beam was set to [100]. We detected time-resolved magnetooptical signals (TRMO) which reflect the pump-pulse induced magnetization precession independent of the pump pulse polarization. The data can again be fitted by the phenomenological Eq. (3.21) – We recall that the parameters A and C describe amplitudes of the oscillatory and pulse-like components of the signal. Simultaneously, we recorded also the transient change of the sample reflectivity.

The coherent control of magnetization precession is illustrated in Fig. 3.31. The top trace in Fig. 3.31(a) shows how pump pulse 1 arriving at zero time delay triggers precession of magnetization, as described in detail in **Chap. 3.3.2**. The time delayed pump pulse 2 *alone* has exactly the same influence on the magnetization, as can be seen on the second trace from the top in Fig. 3.31(a). When *both* pulses excite the sample, the situation changes significantly. If a time delay between pulses 1 and 2 (Δt_{12}) is equal to an *odd* multiple of a half of the precessional period T_{osc}, the magnetization precession is *suppressed*. On the contrary, if the second pump pulse arrives at an *integer* number of *full* periods, the subsequent precession is *enhanced.* In comparison, in Fig. 3.31 (b) we show the transient change of the sample reflectivity $\Delta R/R$, which monitors the photoinjected carrier (electron) dynamics.

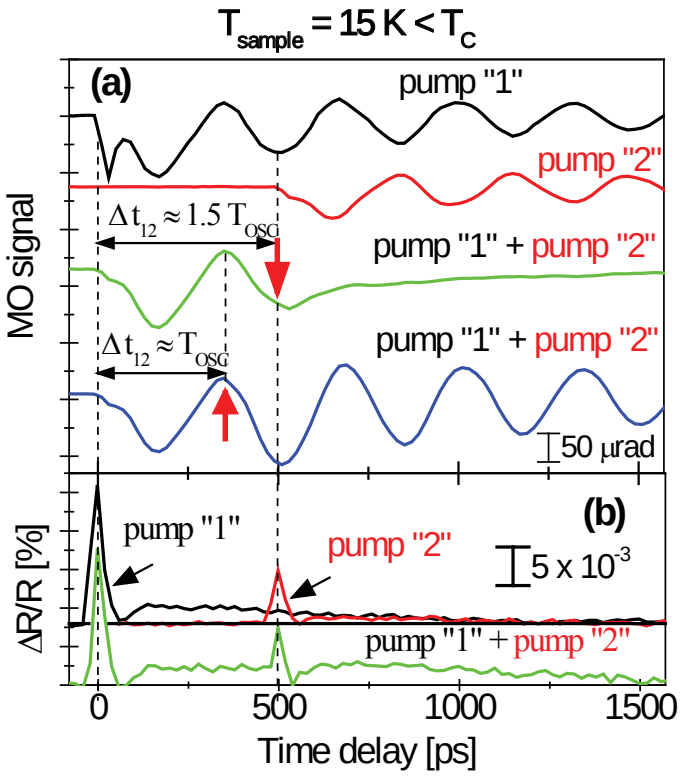

Fig. 3.31 (a) Double-pump TRMO experiment below the Curie temperature, the experimental parameters are: T = 15 K, $\mu_0 H_{ext}$ 10 mT (along [010] direction), probe polarization along [100]. Each pump pulse alone triggers precession of magnetization with a precessional period T_{osc}, as shown by the top and the second from top traces for pump pulses 1 and 2, respectively. If pump pulse 2 excites the sample 500 ps≈1.5 T_{osc} after pulse 1 (vertical arrow), the magnetization precession is stopped. If the time delay between the pulses is 340 ps≈T_{osc}, the magnetization precession is amplified (the bottom trace). The curves are vertically shifted for clarity. (b) Simultaneously, the measured dynamics of the reflectivity change. The horizontal line corresponds to ΔR=0; the bottom curve was vertically shifted for clarity.

The dynamics of $\Delta R/R$ induced by pump pulses 1 and 2 are very similar. The only difference is in the signal magnitude as a consequence of the lower intensity of pump pulse 2. When both pump pulses excite the sample, the signals simply add up [see bottom trace in Fig. 3.31 (b)] with no significant dependence on Δt_{12}. Similarly to the reflectivity signal, the non-oscillating TRMO trace detected above Curie temperature (Fig. 3.32) is also independent of Δt_{12} in the presence of both pump pulses, which confirms its purely "optical origin", with no connection to the change of the magnetic order (see **Chap. 3.3.2**). This conjecture is also supported by the observed suppression of the TRMO signal induced by pump pulse 2 in the double-pump experiment compared to that caused by pump pulse 2 in the single-pump experiment (see Fig. 3.32). The available defect states are probably already partially filled by carriers photoexcited by pump pulse 1 and, therefore, pump pulse 2 can induce only a smaller change of the complex index of refraction.

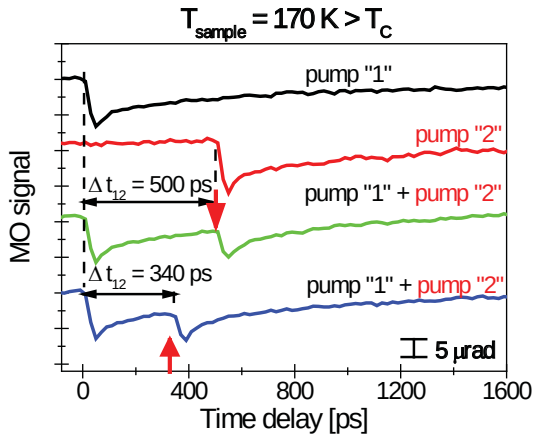

Fig. 3.32 Double-pump TRMO experiment above the Curie temperature; the experimental parameters are: T = 170 K, $\mu_0 H_{ext}$ 10 mT (along [010] direction), probe polarization along [100]. The notation is the same as in Fig. 3.31. Note a reduction in the signal amplitude with the sample temperature.

Let us now analyze the data measured below Curie temperature demonstrating the coherent control in more detail (Fig. 3.33). If only pump 1 excites the sample, the precession amplitude A_1 is slowly damped in time (black solid line in Fig. 3.33). When both pump pulses excite the sample, the resulting precession amplitude is very sensitive to the value of Δt_{12} (solid points). In the vicinity of $\Delta t_{12} = 1.5\ T_{osc}$, which corresponds to the mutual phase difference between the oscillations $\Delta\Phi=3\pi$, this dependence can be approximated by the function $1+\cos\Delta\Phi$ (dashed line in Fig. 3.32), as expected for the sum of two mutually phase shifted harmonic functions. The amplitude of the pulse-like background C (open points in Fig. 3.32) is only weakly dependent on Δt_{12}. We should also mention that for efficient coherent control of the magnetization dynamics, the amplitudes of the precessions induced by pump pulses 1 (A_1) and 2 (A_2) have to be the same in the moment of the impact of pump pulse 2. Consequently, due to the damping of A_1 in time, the intensity of pump pulse 2 had to be lower than that of pump pulse 1.

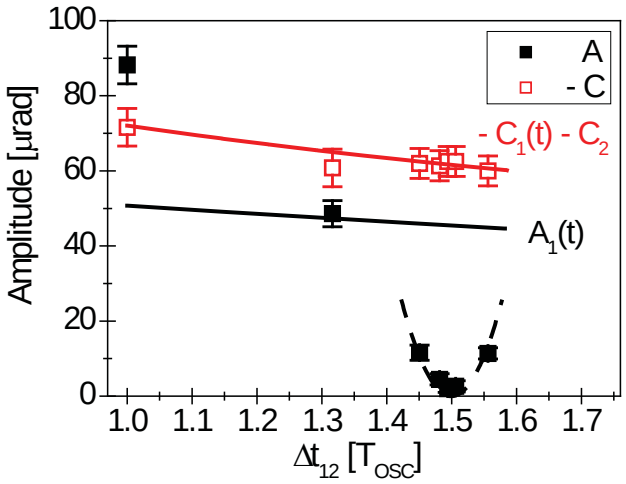

Fig. 3.33: Dependence of A and –C on the time delay Δt_{12} between pump pulses 1 and 2 in the double-pump TRMO experiment (points); the time delay is expressed in multiples of the precession period T_{osc} = 323 ps. The black solid line shows the evolution of A1 in time and the red line corresponds to $-C=-C1\ \exp(-\Delta t_{12}\ T_{osc}\ /\tau 2)-C2$, where the values of all parameters were obtained from the single-pump experiments with pump pulses 1 and 2. The dashed line depicts the function $1+\cos 2\pi\Delta t_{12}$

3.6.2 Phenomenological model

In view of the magnetization precession model presented in Chap. 3.4., the evolution of magnetization ***M(t)*** after the coherent control can be understood as follows. Before the impact of any laser pump pulse *(t = 0)*, the magnetization **M** is aligned with the easy axis (*EA*) which is given by the free energy *F* minimum – as schematically depicted in Fig. 3.34 (a). Note that the functional *F* presented in the picture is valid for an arbitrary set of the anisotropy parameters. The impact of *pump 1* (at $t > 0$) causes a shift of the EA and consequently, the magnetization starts to precess to follow the new EA [Fig. 3.34 (b)]. *Pump 2*, which arrives time-delayed by Δt_{12} with respect to *pump 1*, causes the same shift of the EA axis. Therefore, the resulting ***M(t)*** dynamics depends strongly on Δt_{12}. If *pump 2* hits the sample at $\Delta t_{12} = 3/2\ T_{osc}$, (i.e. at the time when ***M*** lies exactly in the position of the new EA shifted by the pump 2), the precession is stopped – see Fig. 3.34 (c). In the opposite case, when $\Delta t_{12} = T_{osc,}$ the ***M*** vector is as far as possible from the new position of the EA, and thus the precession is amplified – i.e. amplitude *A* increases [Fig. 3.34 (d)]. Amplitude *C* of the non-oscillating background, on the other hand, is connected with the in-plane shift of the EA caused by the energy transfer from the both pump pulses. Consequently, it does not depend significantly on the time-delay between the two pump pulses.

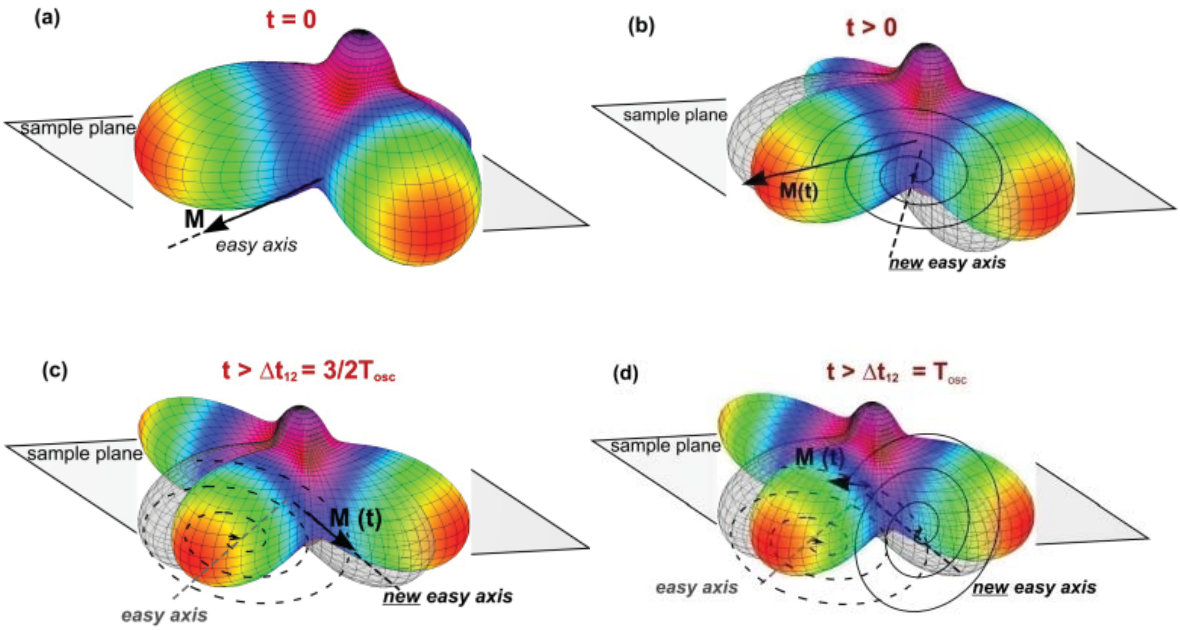

Fig. 3.34: Schematic depiction of the coherent control of magnetization precession. (a) Before the impact of pump 1 pulse the magnetization M (indicated as arrow) is aligned with the easy axis EA (dashed line) given by the minimum of free energy functional. We show an energy functional of an arbitrary (Ga,Mn)As sample. (b) The impact of pump 1 causes reorientation of the EA and subsequent precession of **M** with a period T_{osc}. If pump 2 arrives with a time delay $\Delta t_{12} = 3/2\ T_{osc}$ (c), **M** lies in the position of the new EA and the precession is stopped. For $\Delta t_{12} = T_{osc}$ (d) **M** is far from the new EA and the precession is amplified.

3.6.3 Conclusions

We used double-pump time-resolved magnetooptical (TRMO) experiment to demonstrate the possibility of an all-optical coherent control of magnetization. The magnetization precession induced by a laser pulse was either suppressed or amplified by a second pump pulse, depending on their mutual time delay. Simultaneously, by comparison with the transient reflectivity measurement and TRMO experiments above the sample Curie temperature we showed that such coherent behavior is unique for the processes connected with magnetization dynamics.

3.7 Voltage control of magnetization precession in hybrid structures with (Ga,Mn)As

The possibility to manipulate the magnetization direction and/or magnitude is crucial with respect to spintronics applications. The concept of an all-optical control presented in the previous chapter is, however, not directly suitable the spintronics components where the electrical functionality is required. A direct electrical control of ferromagnetism in (Ga,Mn)As by gating was demonstrated in several works [**31**], [**127**], [**128**] but with a relatively low efficiency which results from the necessity of a relatively high equilibrium hole concentration in ferromagnetic (Ga,Mn)As. Therefore, another approach has been developed that uses the sensitivity of magnetic anisotropy of this material to strains as small as 10^{-4} [**12**], [**62**]. The additional strain can be inserted during the growth by the lattice parameter engineering [**61**], [**62**], by the postgrowth lithographic patterning [**129**], [**12**] or by attaching the samples to a piezo-stressor [**11**], [**117**], [**13**], [**130**]. It is the latest technique that is an important step towards the hybrid multiferroic

devices [**116**] as it represents an extremely efficient though indirect form of electrical gating of the magnetic properties in semiconductors.

In order to control the laser-induced magnetization dynamics by strain, post-growth lithography has been used so far [**115**]. Otherwise, only the position of the magnetization under the equilibrium conditions (i.e. the magnetization easy axis) was modified by the external strain. In this chapter we present the results of the time-resolved magnetooptical experiments performed on hybrid structures consisting of a (Ga,Mn)As sample and a commercial piezo-stressor. We show that the laser-induced precession of magnetization induced by the energy transfer from the laser pulses (see **Chap. 3.3**) can be efficiently controlled by inserting additional uniaxial strain that affects the sample magnetic anisotropy. However, before we proceed to the actual TRMO experiments, we would like to explain some of the basic technological issues encountered in strain generation and detection.

3.7.1 Hybrid structures

Fabrication

Our hybrid multiferroic structures consist of the commercial lead-zirconium-titanate (PZT) piezo transducers from *Piezomechanik Gmbh* [**131**] and the (Ga,Mn)As/GaAs samples (see **Chap. 3.3.1**). The substrate of the samples was first thinned to ~ 200 μm by wet abrasion on the 2500 grit sand paper in order to improve the strain transfer from the transducer to the (Ga,Mn)As layer [**11**], and the thinned layers were then glued on top of the piezo-transducers. Different types of glue were tested to ensure proper homogeneity and thermal conductivity[8]: two component epoxy UHU Plus Endfest 300 kg epoxy (UHU epoxy in further), silver epoxy EPO TEK E4110, and standard GE varnish. The corresponding experimental results concerning the homogeneity will be presented in **Chapter 3.7.2**.

The commercial transducers used in our experiments are formed by a large number of piezo ceramic/electrode layers that are electrically isolated from each other, and biased independently. The direction of the multilayer piling determines the main axis along which the device expands/compresses. The expansion in the major direction is naturally accompanied by a compression in the two minor directions whose magnitude scales approximately with the ratio of the transducer dimensions (Fig. 3.35) – for more details see [**131**]. We used PZT *piezo stacks Pst150/2x3x9 mm* (9 mm long, 2x3 mm cross section), suited for a semi-bipolar operation – i.e. positive/negative voltage results in the expansion/compression of the transducer in the direction of the main axis. At low temperatures, the overall size of the piezo effect is comparable for both voltage polarities. When the temperature is increased, the strain becomes larger for positive voltage. This feature is natural for the "semi-bipolar" action and it was also observed during our experiments (see the next chapter). The *piezo stacks Pst* are utilized to induce predominantly *uniaxial* strain in the attached sample in the main axis along which they expand/compress (Fig. 3.35). In further work they will thus be referred to as "*uniaxial stressors*". For the maximum voltage of U = ± 150 V achievable in our experimental setup, the uniaxial tensile/compressive strain $\varepsilon_{xx} \approx \pm 10^{-4}$ is generated. In the perpendicular direction, the strain $\varepsilon_{yy} \sim \mp 10^{-5}$ arises simultaneously. The strain level can be further detected by strain gauges attached to the piezo stressors (see **Chap. 3.7.2**).

[8] This fabrication technique is suitable only for the low-temperature measurements. As follows from the additional strain gauge and X-ray measurement, at room temperature the tested types of glue are not stiff enough and the strain generated by the piezo transducer relaxes fully in the glue layer.

In addition to the strains generated by the piezo transducer a *tensile biaxial strain ~ 10^{-3}* and an *uniaxial strain ~ 10^{-4}* in the major axis of the stressor occur in the sample during the cooldown [**11**], [**13**]. These strains result from different thermal contraction coefficients of the PZT and the GaAs substrate and as such they cannot be accurately measured.

The overall effects of the piezo stressor on the (Ga,Mn)As sample then depend on the magnitude of the induced strain compared to the inherent strains of the sample (see **Chap. 3.1.3**). Therefore, the choice of the proper native (Ga,Mn)As sample and its orientation is crucial with respect to the efficiency of piezo control.

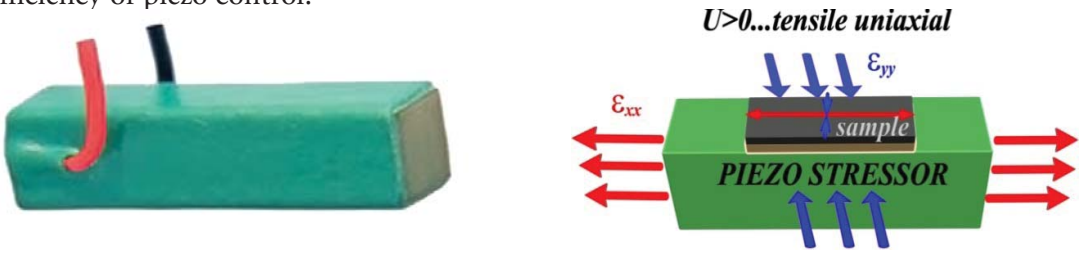

Fig. 3.35: Photo [**131**] and schematic illustration of the working principle of the uniaxial piezo stressor for the applied positive voltage U > 0 (U < 0 results in the opposite effects). The red arrows indicate expansion of the stressor along the main axis while the blue ones show compression for the minor axes. The positive voltage leads to the uniaxial tensile strain, negative to the uniaxial compressive strain.

Samples

In order to establish suitable conditions for the piezo-gating experiments we used two (Ga,Mn)As samples for the hybrid structure fabrication. The first one was the annealed **D071** sample with $x = 7\,\%$ that was studied in the previous chapter, and whose properties were already described in detail (**Chap. 3.3.1**). Here we would like to stress that this sample is characterized by its relatively soft in-plane anisotropy. The corresponding anisotropy constants obtained from SQUID measurement are: $K_c = 10.4\ mT$, $K_u = 9.4\ mT$, $K_z = -253\ mT$.

The second sample *F016* belongs to the "optimized set" of (Ga,Mn)As samples described in [**20**]. The 20 nm thick layer contains $x_{nom} = 3.8\,\%$ of nominal Mn doping and after the post-growth annealing (12 hours at 200 °C) its Curie temperature reaches $T_c = 96\ K$. Similarly to the *D071* layer, a competition between the in-plane uniaxial and biaxial anisotropies exists in the sample, but the lower doping level leads to a stronger cubic anisotropy [see Fig. 3.8 (c)] : $K_c = 48\ mT$, $K_u = 28\ mT$, $K_z = -104\ mT$ [**122**].

In Table 2 we summarize the (Ga,Mn)As/piezo stressor hybrid structures studied in our work.

structure name	***(Ga,Mn)As layer***	***glue***	φ_{str}	φ_H
D071_P1	D071	UHU	45°	90°
D071_P2	D071	UHU	45°	45°
D071_P3	D071	GE varnish	45°	45°
F016_P1	F016	EPO-TEK	115°	115°
F016_P2	F016	UHU	115°	115°
F016_P3	F016	EPO-TEK new gluing	115°	115°

Table 2: Hybrid structures (Ga,Mn)As/piezo stressor used in the work. The azimuthal angles of the major uniaxial strain generated by the stressor (φ_{str}) and of the external magnetic field (φ_H) used in the experiments are defined from the [100] crystallographic direction.

For all the studied (Ga,Mn)As samples, the in-plane internal *shear strain* $e_{xy} \sim 2\text{-}3\times10^{-4}$ and the growth strain is $e_0 \sim 10^{-3}$ [**62**]. The value of e_{xy} is comparable to the strain generated by the commercial piezo stressors, as published in the literature [**13**], [**130**], [**116**]. Therefore, it is necessary to detect the strain generated by the stressors used in our experiments.

3.7.2 Strain measurement

We detected the strain generated by the piezo stressors in the two perpendicular directions (e_{xx} and e_{yy}, see previous chapter) by two *strain gauges* (SG) – thin metallic wires whose resistances change as functions of their relative prolongation/contraction [see Fig. 3.36 (a)].

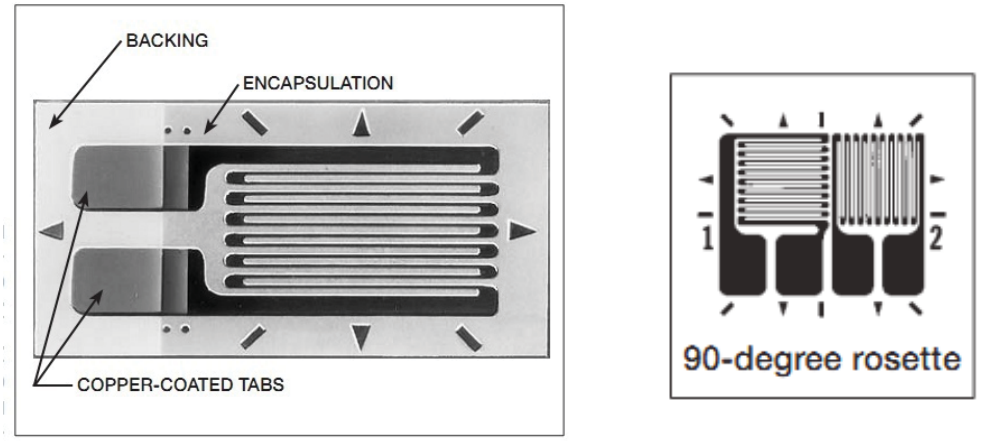

Fig. 3.36: (a) Metallic strain gauge with encapsulation and (b) tee-rosette two strain-gauge scheme [**132**]

The wires are usually mounted on a plastic backing, which provides means of manipulation with the gauge and simultaneously an electrical insulation, and the copper tabs enable wire bonding. The encapsulation layer protects the thin wires from mechanical damage. We used Karma alloy (Ni: 74%, Cr: 20%, Al: 3%, Fe: 3%) strain gauges from *Vishay Micromeasurements Group*, part number *WK-06-062TT-350*. These SGs are formed by two independent foils wired perpendicular to each other ["rosette" geometry, see Fig. 3.36 (b)], thanks to which both components of the strain can be detected simultaneously. In our TRMO experiments the in-situ strain measurement was not possible due to geometrical restrictions. Therefore, the strain was measured on a testing piezo stressor/GaAs hybrid structure prepared in the same manner as the "real" structures with (Ga,Mn)As, and the experiment was repeated in order to test the reproducibility. The SG was attached to the GaAs layer by an UHU epoxy and cured at 80 °C for 40 minutes.

Despite the simple working principle of the gauges, several technical issues have to be met in real applications. Besides the problems with proper bonding, gluing etc. (details in [**132**]) two aspects of the strain measurement are of special importance in our experiments performed at cryogenic temperatures, where the strains of the order of 10^{-5} are recorded.

First, we have to account for the mismatch between the thermal expansion coefficients of the *SG* and the explored material (GaAs in our case) which manifests as a false output signal during the cooldown. For certain types of SG alloys it is possible to minimize such thermal output in a wide temperature range by choosing a properly processed type of alloy that matches the material for which the SG is intended [**132**]. This process is called *self-temperature-compensation* (S-T-C). The *Vishay* SGs are denoted by the S-T-C number that indicates the nominal thermal expansion coefficient of the detected material (the "06" in our case). Nevertheless, the S-T-C procedure

has its limitations as the alloys are typically characterized in a "conventional" temperature range (-50 °C...+ 250 °C). This problem can be circumvented to some extent by deliberately mismatching the S-T-C number and the thermal expansion coefficient so that it fits the particular temperature range – hence the STC = 06 in our SGs (which corresponds to steel – details in [**132**]). As we measured the strain *variation* after piezo-stressing at a given temperature in our experiments, the exact STC matching was not crucial. However, if the information about the strain thermally induced in the (Ga,Mn)As/PZT structure is to be accessed (see the previous chapter), the exact correction for the thermal output of the SGs [**132**] has to be taken into account.

The second technical challenge of the strain detection lies in a reliable measurement of the small resistivity changes resulting from the extremely low strain levels of interest. The static resistance of the SG is $R_0 = 350\ \Omega$ (at a room temperature) and a resistivity variation of the order of 10^{-6} has to be recorded. For this purpose, we used a sensitive home-made Wheatstone bridge circuit (see Fig. 3.37 (a) for a simplified scheme)[9] which was supplied by a constant current $I = 1\ mA$. In the equilibrium state (i.e. with no voltage applied to the piezo stressor) we balanced the bridge with a potentiometer. As the SG was strained, its resistance changed and we detected a small voltage drop ΔU across the bridge, from whence the resistivity change ΔR = ΔU/I can be calculated. The strain ε is then related to ΔR through a gauge factor G, provided by the manufacturer. Thus the following expression can be derived for the strain measurement using a Wheatstone bridge [**132**].

$$\varepsilon = \frac{\Delta R}{R_0}\frac{4}{G} \tag{3.29}$$

where R_0 is the static SG resistance. In our particular setup, Eq. (3.29) becomes:

$$\varepsilon = \frac{\Delta U}{AM \cdot I \cdot R_0}\frac{4}{G} \tag{3.30}$$

Where $AM = 5600$ is the amplification of the circuit, $G_1 = 1.9$ for channel *1* (detecting ε_{xx}) and $G_2 = 2.01$ for channel *2* (detecting ε_{yy})

The bridge was placed in a box kept at a constant temperature in order to achieve the best stability possible. The results of a time-stability test performed at low temperature (~ 35 K, see the next chapter) are shown in Fig. 3.37 (b). For clarity reasons, the voltage change ΔU was converted to strain according to Eq. (3.30). The two channels represent two independent bridge circuits detecting signals from the two parts of the tee-rosette SG. Clearly, the time stability of the circuit sets a limit to the precision of the strain measurement. Channel 2, better in terms of stability, enables to detect strains larger than ~ $1\text{x}10^{-5}$ and it was used for the smaller transverse ε_{yy} strain component, while channel 1 recorded the larger ε_{xx} strain.

[9] The tee rosette SG scheme that we used was composed of two independent parts. Therefore also our measurement setup contained two equivalent bridge circuits, and the resistivity change was detected separately in each of the tee-rosette SG parts.

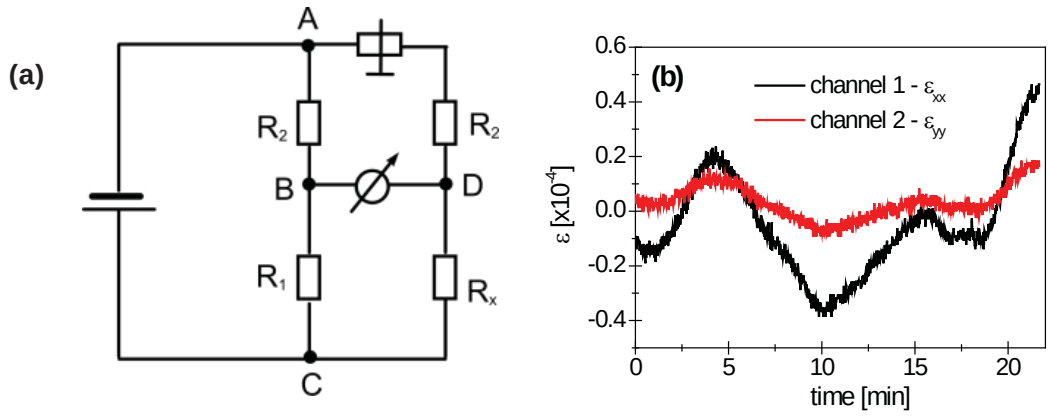

Fig. 3.37: (a) Schematic diagram of the Wheatstone bridge circuit used for the strain measurements. R_2 and R_1 are fixed resistors, where $R_1 = R_2 = 350\Omega$. R_x represents the actual resistivity of the SG under given conditions. In the equilibrium state, the bridge is balanced using a potentiometer, and the imbalance during the experiment is detected as a voltage drop ΔU between points B and D (b) Spontaneous bridge imbalance and corresponding "false" strain signal as a function of time.

3.7.3 Technological aspects of piezo-voltage gating

Before we proceed to the results on piezo-induced gating of magnetization precession, several issues concerning the behavior of the hybrid structures have to be addressed. As has already been stressed in the previous chapters, the laser-induced magnetization precession is connected with the changes of the magnetic anisotropy and, therefore, it is also extremely sensitive to external conditions – especially strain and temperature of the (Ga,Mn)As sample. Both of these parameters can differ markedly when working with the hybrid piezo/(Ga,Mn)As structures compared to the experiments performed on the plain (Ga,Mn)As/GaAs layers (see **Chap. 3.3**) that were not subject to any significant external strain. In this section we present the results of a set of simple control experiments that enabled us to estimate some of the relevant parameters.

Thermal conductivity and stressor attachment

The first parameter in question when dealing with the hybrid (Ga,Mn)As/piezo structure is the actual temperature of the (Ga,Mn)As sample during the measurement. The time-resolved magnetooptical (TRMO) experiments were performed in the same setup as those described in **Chap. 3.3–3.6**. However, in the previous measurements the thin (Ga,Mn)As/GaAs samples were simply glued to the cold finger (CF) of a closed cycle cryostat by a conductive silver-deck which provided excellent heat transfer from the sample. The situation becomes different with the piezo stressors made out of thermally insulating PZT ceramics. In order to obtain a rough estimate of the real temperature on the sample surface we attached a testing GaAs/piezo structure (see the previous section) to the CF by different types of adhesives (*GE varnish* and grease *Apiezon N*). A silicon diode thermometer which detected the temperature T_{piezo} was mounted on top of the structure by using another adhesive layer. Another Si diode measured the temperature T_{CF} of the cold finger. The corresponding results are shown in Fig. 3.38. Clearly, at low T_{CF} the temperature difference between the CF and the (Ga, Mn)As sample (ΔT_{piezo}) is enormous – the lowest temperature that can be obtained in this kind of experiments is $T_{piezo} \approx 40$ K. This value can be regarded as an upper limit for the lowest temperature achievable in our TRMO experiments. In addition, we see that the proper choice of the adhesive plays an important role

– each layer of the insulating GE varnish adds *~7 K* to the difference ΔT_{piezo}, and we, therefore, used mostly Apiezon N in the real experiments.

In addition to the heat transfer, there is another issue connected with the proper attachment of the stressor to the CF. The piezo stressor has to be fixed to the CF but, simultaneously, it has to have a possibility of free expansion/compression. If the latter condition is not fulfilled (for example when the bottom side is covered by the glue-line), a "*d_{31} clamping effect*" [**131**] occurs – the stressor is blocked, starts to bulge and it can even break. A typical example of such behavior is shown in the next chapter, in the section describing the preliminary TRMO experiments. The best attachment in terms of the thermal conductivity and free motion was achieved by clamping the stressor with thin copper wires directly to the CF. We used this method in all the final TRMO measurements.

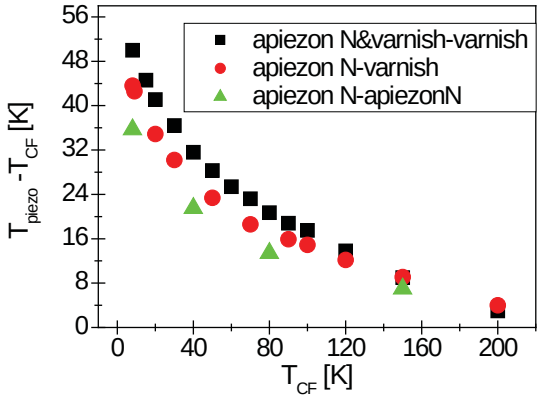

Fig. 3.38: Test experiments showing the difference between the temperature of the cryostat cold finger TCF and the piezo stressor T_{piezo}. The individual dependencies correspond to different adhesives used to attach the stressor to the CF (first layer) and a diode thermometer to the stressor (second layer).

Influence of the cooldown strain

Besides the sample temperature, the second important parameter affecting the magnetic properties of the (Ga,Mn)As layer is the external strain. Before we proceed to a measurement of the strain generated by applying voltage to the piezo stressor we discuss the influence of the strain induced by an unbiased stressor during the cooldown. As was already mentioned, it originates in different thermal expansion of the GaAs substrate (from 5.7 to 7.2x10^{-6} K^{-1}) and PZT (not tabled, depends on the direction of poling), and it has a *tensile biaxial component* (*~10^{-3}*) and a *uniaxial component* (~ 10^{-4}) in the main axis of the piezo stressor [**13**]. Though the cooldown strain could not be detected by our strain gauges (see **Chap. 3.7.2**) its presence is obvious when comparing magnetization dynamics induced by laser pulses in the native (Ga,Mn)As and in the hybrid structures with the same (Ga,Mn)As layer – see Fig. 3.39. Clearly, the same cooling down procedure can lead to a significant increase of the precession frequency ω and amplitude A [see Fig. 3.39 (a)] but also to their decrease [see Fig. 3.39 (b)].

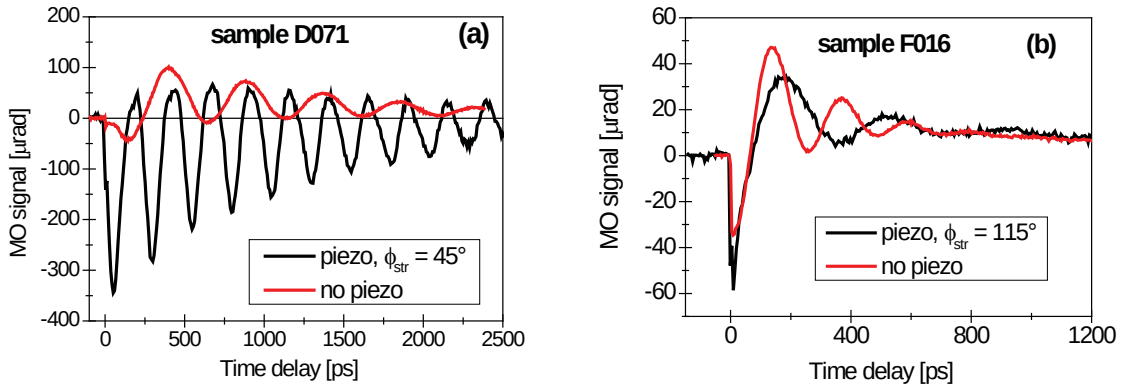

Fig. 3.39: Magnetooptical signal detected on hybrid (Ga,Mn)As/piezo structures and the corresponding native samples. (a) The D071 (x = 7%, Tc = 160 K) and structure D071_P2 (φ_{str} = 45°). Corresponding frequencies are ω_{native} = 13 GHz, ω_{piezo} = 25.4 GHz (b) sample F016 (x = 3.8 %, Tc = 96 K) and structure F016_P1 (φ_{str} = 115°). ω_{native} = 27.2 GHz, ω_{piezo} = 17.8 GHz
$\mu_0 H_{ext}$ = 0 mT, temperature: T ≈ 15 K in native sample, T ≈ 40 K in hybrid structure, NO voltage applied to the stressor

More effects can be responsible for such a distinct behavior. The inherent in-plane anisotropy of the D071 sample is relatively weak and therefore any additional in-plane strain (biaxial and uniaxial) would affect its properties more than in the case of the *F016* sample with stronger anisotropy. On the other hand, the higher temperature of the hybrid structure (~ 40 K, see the previous section) can explain the lower ω compared to the native *F016* sample (see **Chap. 3.3** and **3.4**). Furthermore, the *biaxial tensile strain* that manifests in the same manner as the growth strain (**Chap. 3.1.3**) favors the out-of-plane EA position, which results in weakening of the inherent out-of-plane hard axis. This feature is of particular importance with respect to the strong photomagnetic effects observed in the hybrid structures (see **Chap. 3.8**).

Finally, we would like to show the importance of the orientation of the magnetic easy axis in the sample with respect to the stressor main axis (SMA) for the thermally induced strain. The frequency ω is related to the sample anisotropy through Eq. (3.16). Assuming the free energy in the form of 3.9.(a), we obtain [133]

$$\omega = \gamma\left[\left(H_{ext}\cos(\varphi-\varphi_H)-2K_{[001]}+\frac{K_c(3+\cos 4\varphi)}{2}+2K_{[110]}\sin^2\left(\varphi-\frac{\pi}{4}\right)+2K_\Omega\sin^2(\varphi-\Omega)\right)\right.$$
$$\left.\times\left(H_{ext}\cos(\varphi-\varphi_H)+2K_c\cos 4\varphi-2K_{[110]}\sin(2\varphi)-2K_\Omega\cos 2(\varphi-\Omega)\right)\right]^{1/2} \qquad (3.42)$$

here H_{ext} stands for the external magnetic field, $K_{[001]}$, $K_{[110]}$, K_c are the anisotropy constants defined in Chap. 3.1.3 and K_Ω denotes the constant describing the uniaxial anisotropy in a direction Ω, generated by an additional uniaxial strain applied in the direction φ_{str}. Let us assume that $\Omega = \varphi_{str}$ for simplicity (**Chap. 3.1.3**). In the first hybrid structure (*D071_P2*) the *D071* sample is glued in such a way that the SMA lies approximately in the direction of the hard axis – i.e. φ-$\varphi_{str} \approx 90°$. On the other hand, in the *F016_P1* structure, the sample *F016* is attached so that the easy axis is aligned with the SMA – i.e. φ-$\varphi_{str} \approx 0°$. The overall contribution of K_Ω to ω can, therefore, be negative in one case and positive in the other one.

The importance of the alignment of the (Ga,Mn)As layer with respect to the stressor is also suggested by the difference in behavior of the TRMO signal detected in the two hybrid structures *D071_P2* and *P3* (see Fig. 3.40). These structures should, in principle, be identical but for the imprecise alignment. However, the difference in the adhesives used for the sample gluing can also play some role.

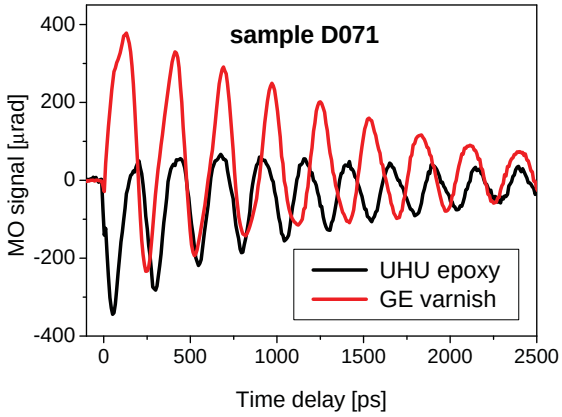

Fig. 3.40: Magnetooptical signal detected on two nominally identical hybrid (Ga,Mn)As/piezo structures D071_P2 and D071_P3.

$\mu_0 H_{ext}$ = 0 mT, T ~ 40 K, φ_{str} = 45° NO voltage applied to the stressor

The complexity of thermally induced strain effects makes it difficult to characterize the hybrid structures in an "equilibrium" state – with no voltage applied to the stressor, as the thermal strain can vary even within different cooldown cycles. On the other hand, the strain generated by piezo-stressing can be estimated properly by the strain-gauge measurement.

Strain generated by the piezo stressors

The strain-gauge (SG) experimental setup described in **Chap. 3.7.2** was used to characterize the influence of the piezo-voltage on the GaAs test layer. The strain generated by the uniaxial stressor ($T \approx 40$ *K*) in the two perpendicular directions at different voltages U is depicted in Fig. 3.41.

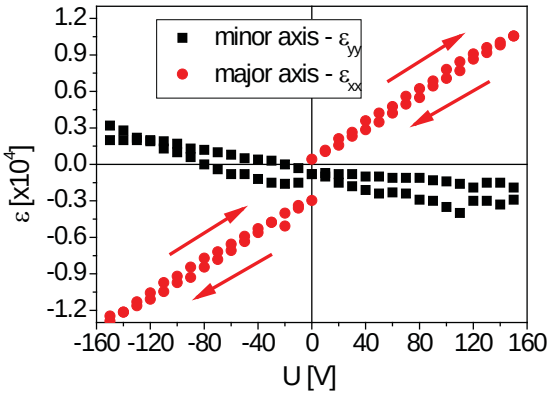

Fig. 3.41: Measurement of the strain generated by a uniaxial piezo stressor at T ≈ 40 K along its major (ε_{xx}) and minor (ε_{yy}) axes by using strain gauges. The individual parts of the hysteresis loops were measured by applying the voltage as follows (indicated by arrows):

"positive branch":

+150 V…0V…+150V,

"negative branch":

-150 V … 0 V…150 V

Here, ε_{xx} corresponds to the main axis of the stressor, ε_{yy} to the minor axis. We see that both strains increase linearly with U and have opposite signs. The strain ε_{yy} is roughly 5x smaller than ε_{xx}, as expected from the piezo stressor geometry [**131**]. The maximum uniaxial strain $\boldsymbol{\varepsilon_{xx}} \approx \pm 1.2x10^{-4}$ for U = ± 150 V can be generated in our experimental setup at T ≈ 40 K, symmetrically for both voltage polarities. This symmetry is typical for the low-temperature operation of the stressor but it is broken when reaching higher T, as demonstrated also in Fig. 3.42 (a) where the absolute

value of the strain ε_{xx} is depicted as a function of T. The same dependence is presented in Fig. 3.42 (b) for the ε_{yy} strain. Furthermore, we see that the magnitude of the piezo-strain increases at elevated temperatures. Both these features follow from the fact that the stressors are suited for a semi-bipolar operation at room temperature [**131**], and the PZT ceramics loses efficiency after cooling down [**131**].

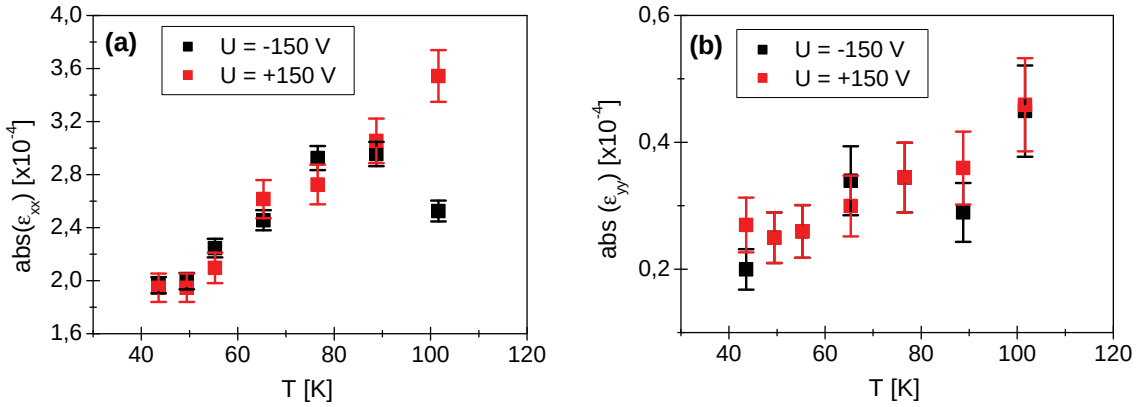

Fig. 3.42: Temperature dependence of strain generated by a uniaxial piezo stressor along (a) major (εxx) and (b) minor (εyy) axis, detected by a strain gauge. The stressor was biased by a voltage of ± 150 V, and the absolute value of ε is depicted. Clearly, the piezo effect increases with increasing temperature.

Finally, we would like to comment on the observed hysteretic nature of the *ε(U)* function (Fig. 3.41). Such behavior is typical for the complicated stacked PZT structures [**131**] and cannot be easily avoided [**134**], [**11**]. The equilibrium "zero-voltage" state is, therefore, not properly defined.

Having characterized the influence of the piezo stressor on the (Ga,Mn)As layers in the hybrid structures we can now present the actual results of the time-resolved magnetooptical (TRMO) experiments.

3.7.4 Piezo-voltage gating – experimental results

In this chapter we will summarize the results concerning piezo-voltage control of the laser-induced magnetization precession described in **Chap. 3.3** and **3.4**. We would like to stress once more that all the TRMO traces presented here are pump-polarization independent signals, and the observed magnetization dynamics is connected solely with a transfer of the energy from the pump pulses to the (Ga,Mn)As samples – either by heating or by the increase of the hole concentration, which modifies the magnetic anisotropy.

In the experiments presented in this chapter we used the above-bandgap wavelength of the pump and probe beams (λ = 757 nm). The notation is equivalent to the **Chap. 3.3** – i.e., azimuthal angles of the external field φ_H, uniaxial piezo strain φ_{str} and probe polarization β are defined from the [100] crystallographic direction. We will limit our discussion to the influence of the uniaxial strain along the major axis of the stressor, further denoted simply as *uniaxial strain ε*.

Proof of principle experiments

The first preliminary TRMO measurements were performed on the hybrid structure *D071_P1* that was attached to the cryostat cold finger by a solid thin layer of GE varnish. The main axis of

the stressor is aligned with the [110] direction (φ_{str} = 45°) and the external magnetic field $\boldsymbol{H}_{ext}$ is applied along the [010] direction (φ_H = 90°) in this structure.

The strain-induced control of the magnetization precession is demonstrated in Fig. 3.43. The TRMO traces were recorded for three different piezo voltages and no external magnetic field applied. Obviously, the TRMO signal is amplified for negative voltage *U = -150 V* with respect to the one detected on the „unstrained" *(U = 0 V)* sample. In contrast, *U = + 150 V* applied to the stressor can cancel out the magnetization precession.

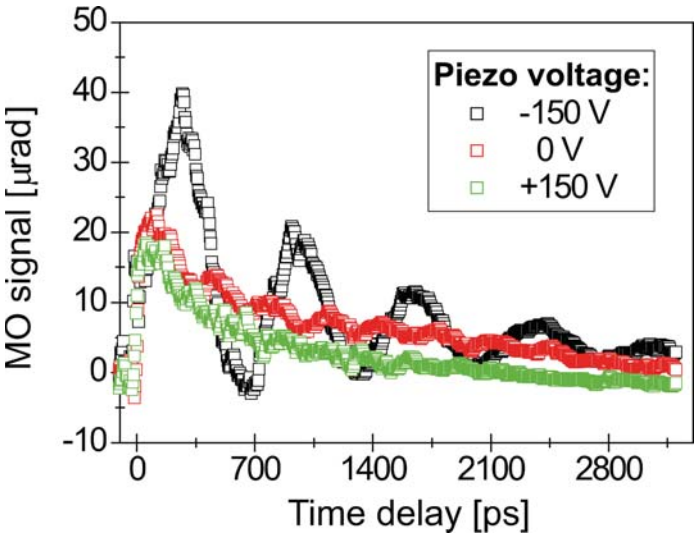

Fig. 3.43: Magnetooptical signal detected on the hybrid structure D071_P1 for different voltages applied to the stressor: U = -150 V, 0 V, +150 V. For U < 0 the TRMO signal is amplified, while for U > 0 the signal is cancelled out.

The sample temperature was T ≈ 40 K, probe beam polarization β = 0° and no external field was applied.

In Fig. 3.44 we present a dependence of (a) the precession amplitude A and (b) the frequency ω on the external magnetic field (H_{ext}). Surprisingly, the $A(H_{ext})$ function shows the shape typical for the Hext aligned with the hard axis (see Fig. 3.21 – native (Ga,Mn)As sample), or for the out of plane contribution to the magnetic anisotropy (see Fig. 3.31 (b) – spin-wave resonances in D071 sample). Furthermore, both the overall precession amplitude and the frequency [Fig. 3.44 (b)] are strongly modified by the strain generated by the piezo stressor – the increase of *A* at *U = -150 V* is accompanied by the decrease in ω and vice versa.

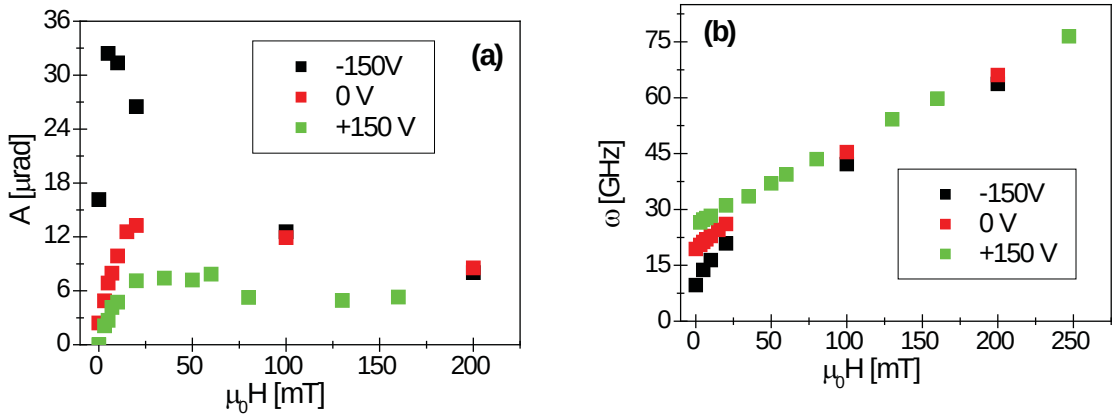

Fig. 3.44: Dependence of (a) the precession amplitude *A* and (b) frequency ω on the external magnetic field $\boldsymbol{H}_{ext}$ applied in the [010] direction, detected for different voltages applied to the piezo stressor: U = -150 V, 0V, +150 V. The corresponding data were extracted from the TRMO signals measured at T ≈ 40 K, probe polarization β = 0°, and pump fluence I_0 = 21 μJ.cm^{-2} by fitting to Eq. (3.21).

In Fig. 3.45 we show the amplitudes *A* and *C* [defined in Eq. (3.21] as functions of the probe beam polarization *β*. Clearly, the position of the maximum in the *A(β)* function shifts when ± 150 V is applied to the stressor which means that the easy axis is rotated (see **Chap. 3.4**) by the piezo-stressing. By fitting the data to Eq. 3.24 and Eq. 3.23 we obtain the easy axis (EA) position which goes from $\varphi_{M-} = 67°$ for $U = -150\,V$ to $\varphi_{M+} = 34°$ for $U = +150\,V$. Simultaneously, the ratio between out-of-plane (A^{PKE}) and in-plane (A^{MLD}) component of the precession motion changes from $(A^{PKE}/A^{MLD})_- \approx 1.4$ to $(A^{PKE}/A^{MLD})_+ \approx 2.1$. While the shift of the EA is an expected phenomenon that has been observed in several works [**117**], [**13**], [**130**], the change of the A^{PKE}/A^{MLD} that results from the modification of the out-of-plane anisotropy (see Chap. 3.5.) is quite striking.

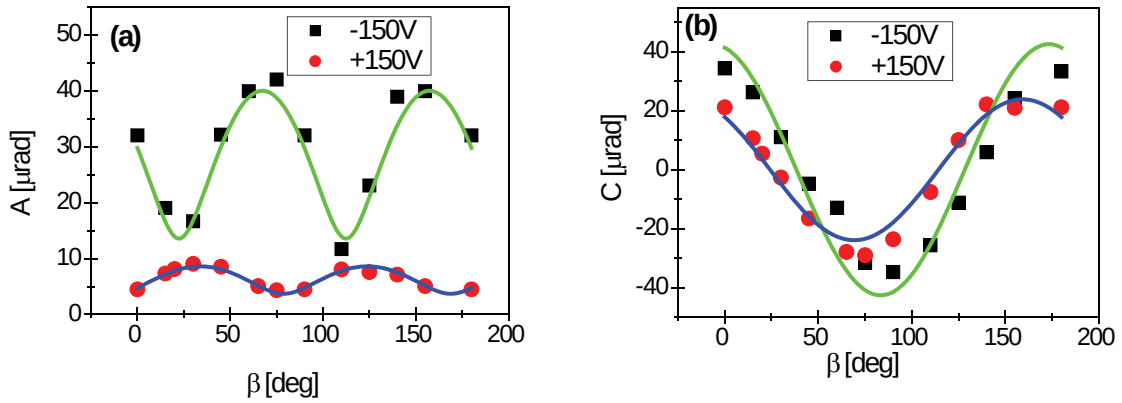

Fig. 3.45: Probe-beam polarization dependence of (a) precession amplitude *A* and (b) pulse function amplitude *C*, detected for U = ± 150 V applied to the piezo stressor. The corresponding data (points) were obtained by fitting to Eq. 3.21. The lines are fits of the A(β) and C(β) to Eq. 3.29 and 3.32 with the following parameters:

For U = +150 V: $r = 0.9982$, $\boldsymbol{\varphi_M = 33.8°}$, $\delta\varphi_M = 0.25°$, $A^{PKE} = 3.7$ *and* $p = 2.51$

For U = -150 V: $r = 0.9982$, $\boldsymbol{\varphi_M = 67.3°}$, $\delta\varphi_M = 1.15°$, $A^{PKE} = 13.6$ *and* $p = 2.51$

The TRMO signals were measured at T ≈ 40 K, pump fluence I_0 = 21μJ.cm^{-2} and external field $\mu_0 \boldsymbol{H}_{ext} \approx 0$ mT

All the above described features can be understood if we assume that the effect of "d_{31} *clamping*" has appeared in the stressor as a result of the firm gluing to the cryostat cold finger. In such case, biasing of the piezo causes "bulging" of the structure which leads to the generation of the strain in the (Ga,Mn)As sample both in-plane and out-of-plane, as schematically depicted in Fig. 3.46. If a motion of the stressor is completely blocked the "*clamping*" effect can be extremely strong [**131**] and even the hard out-of-plane anisotropy of the sample D071 ($K_{001} = 253\,mT$) can be modified.

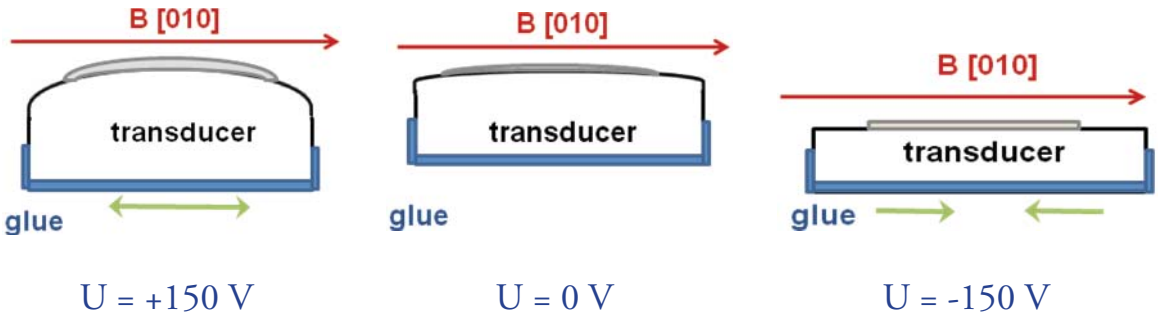

Fig. 3.46: Schematic depiction of the blocked piezo transducer motion. In U = 0 V state, the transducer is already partially deformed due to the thermal expansion during the cooling. If a positive voltage U is applied, the blocked expansion of the piezo stressor leads to a "bulging" which generates in plane and out of plane strain in the (Ga,Mn)As sample (grey layer in the cartoons). For U < 0 V, the shrinking of the stressor compensates partially the deformation and causes in-plane strain.

The results obtained on the *D071_P1* structure demonstrate the importance of the proper attachment of the hybrid structure to the cryostat. TRMO signal detected on the structure *D071_P3* which was designed in the same manner as the *D071_P1* (i.e. sample D071, strain $\varphi_{str} = 45°$) are shown in 3.49. Unlike D071_P1, this structure was fixed "properly" by copper wires. The behavior in terms of polarization and magnetic field dependence was very similar to the one observed in the native D071 sample (not shown here). However, the piezo-voltage has very little impact on the laser-induced precession of magnetization, as follows from Fig. 3.47. The reason for such invariance lies probably in the strong influence of the cooldown strain on the sample with a weak in-plane anisotropy which makes the effect of the piezo-voltage strain negligible. Therefore, for an efficient voltage control of the magnetization precession it is favorable to look for (Ga,Mn)As layer and hybrid structure geometry which will be less sensitive to the cooldown strain.

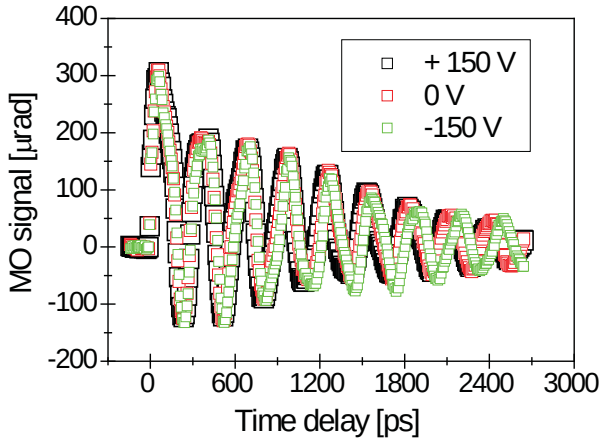

Fig. 3.47: Magnetooptical signal detected on the hybrid structure D071_P3 (native sample D071, $\varphi_{str} = 45°$) for different voltages applied to the stressor : U = -150 V, 0 V, +150.

The sample temperature was T ≈ 40 K, external field $\mu_0 H_{ext} = 0$ mT and probe beam polarization $\beta = 0°$.

Final experimental results

The *F016* layer (*x = 3.8 %, T_c = 96 K*) turned out to be the most promising (Ga,Mn)As sample for the piezo-stressing experiments. The magnetic anisotropy of this sample is strong enough to be comparable with the additional cooldown anisotropy but it can still be modified by the additional piezo-induced strain.

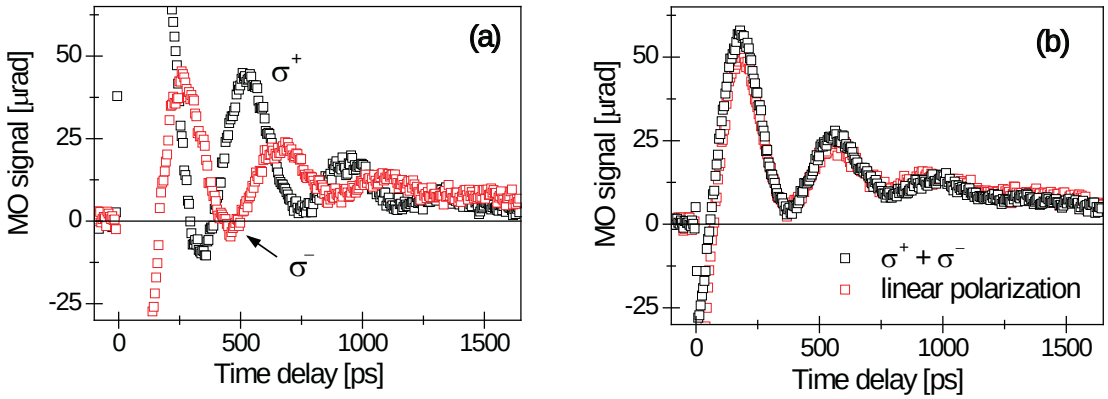

Fig. 3.48: (a) Magnetooptical signal detected on the hybrid structure F016_P1 with circularly polarized σ^- and σ^+ pump pulses and piezo voltage U = +150 V. (b) Helicity-independent part of the signal shown in panel (a) together with data measured with linearly polarized pump pulses.
The data were taken at temperature T ≈ 40 K, external field $\mu_0 H_{ext} = 30$ mT applied at $\varphi_H = 115°$, and probe beam polarization $\beta = 25°$.

A typical time-resolved magnetooptical signal excited in the hybrid structure *F016_P1* by the two helicities of circularly polarized (CP) light is presented in Fig. 3.48 (a). There is a clear phase shift between the signals of opposite helicities which will be discussed in detail in the next chapter. Here we address the helicity-independent part of the TRMO traces for which we take an average over the CP of the excitation – see Fig. 3.48. Such a signal is equivalent to that excited by a linearly polarized (LP) light [see Fig. 3.48 (b)] and it reflects the magnetization precession that was interpreted in terms of a magnetocrystalline anisotropy change by the energy transfer from the pump pulses (see **Chap. 3.2***).*

In the previous section we showed that the magnetization precession is sensitive to the external strain that modifies the sample anisotropy. This enables us to control the magnetization precession by a piezo-voltage. The possibility to manipulate the precession is a general, sample-independent phenomenon, as demonstrated in Fig. 3.49 where the TRMO signal in the *F016_P1* structure is depicted for $U = \pm 150\ V$ applied to the stressor. In contrast with the *D071_P1* structure, the main axis of the stressor (SMA) in *F016_P1* is aligned at jstr = 115°, close to the easy axis of the native *F016* layer. The application of -150 V which generates a compressive strain of (-1.5 ± 0.5) x 10^{-4} along the major axis and a tensile strain of (0.3 ± 0.1) x 10^{-4} along its minor axis (see Chap.) is sufficient to completely cancel out the laser-induced magnetization motion.

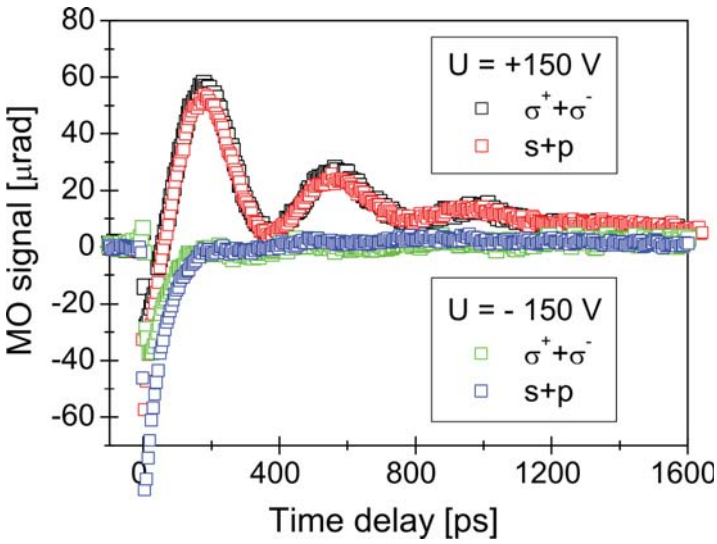

Fig. 3.49: Pump-polarization independent magnetooptical signal detected on the hybrid structure F016_P1 for two different piezo voltages U = +150 V and U = -150 V. The data were measured at T ≈ 40 K, external field $\mu_0 H_{ext}$ = 30 mT applied at φ_H = 115°, and probe beam polarization β = 25°.

In Fig. 3.50 we show the magnetic field dependence of (a) the amplitude *A* and (b) frequency ω of the oscillations for positive and negative piezo-voltages. The field was applied in the same direction as the main axis of the stressor, $\varphi_H = 115°$. At $U = +150\ V$, the amplitude shows the expected gradual decrease with increasing magnetic field (see Fig. 3.21 and **Chap. 3.4**). At $U = -150\ V$, however, the decrease is much more rapid and the polarization-independent oscillations are effectively quenched at 20 mT, and for sufficiently high $\boldsymbol{H_{ext}}$ the amplitudes *A* merge for both of the piezo voltages. In contrast, there is almost no effect of the piezo stressing on the precession frequency.

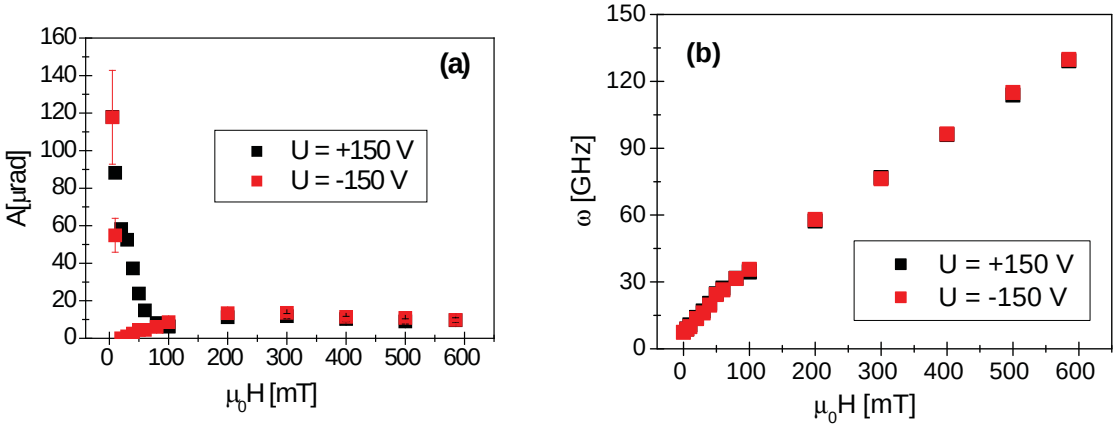

Fig. 3.50 Magnetic field dependence (φ_H = 115°) of the MO signal (a) amplitude A and (b) frequency (b) in the structure F016_P1, which were obtained by fitting to the data measured for the piezo voltage U = ± 150 V applied at φ_{str} = 115°, for T = 40 K, I = 70 μJ.cm-2 and β = 25°.

In further experiments, we set the $\mu_0 H_{ext} = 30\ mT$, which is close to the point where the oscillations are quenched, and we observe how A [Fig. 3.51 (a)] and ω [Fig. 3.51 (b)] develop as a function of the variable U at two different temperatures ($T \approx 40\ K$ and $60\ K$). The behavior differs for the low and higher temperature. At 40 K, the amplitude A gradually increases for positive voltages but for the opposite polarity its behavior becomes non-monotonous, similarly to the magnetic field dependence [Fig. 3.50 (a)]. The exact voltage where the precession is completely suppressed is strongly temperature dependent. In addition, at the elevated temperature (60 K), the frequency, which remained unaffected by the piezo voltage at 40 K, also starts to change – see Fig. 3.51 (b).

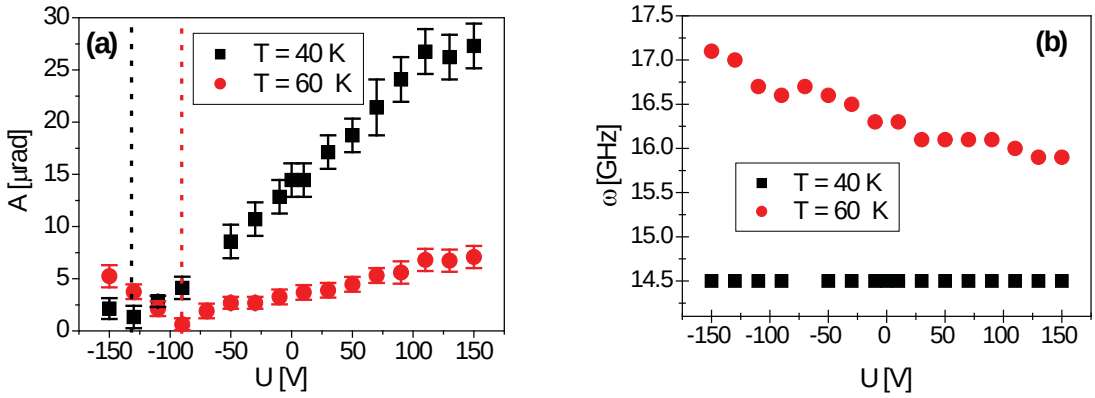

Fig. 3.51: Piezo-voltage dependence (φ_{str} = 115°) of the MO signal (a) amplitude A and (b) frequency, which were obtained by fitting to the data measured with the structure F016_P1 for the field $\mu_0 H_{ext}$ = 30 mT applied at φ_H = 115°, for T = 40 K, I = 70 μJ.cm-2 and β = 25°.

In Chap. 3.4 we showed that the TRMO technique provides information both about the "*stability*" of the easy axis – its sensitivity to the external modification of the equilibrium conditions in the sample, and also about its *position*. For this purpose, we detected the TRMO signal at varied probe polarizations (β) at $U = +150\ V$ and $-70\ V$, and $\boldsymbol{H}_{ext} = 30\ mT$, where the precession is still reliably observable. The corresponding variations of the amplitudes A and C [Eq. (3.21)] are depicted in Fig. 3.52 (a) and (b), respectively. By fitting of the data to Eq. (3.24) and Eq. (3.23) we found out that the voltage-induced shift of the EA is smaller than 3°. On the other hand, the EA tilt δφ that triggers the precession increases from $\delta\varphi_- \approx 0.8°$ (at -70 V) to $\delta\varphi_+ \approx 1.5°$ (at -150 V). Apparently, the position of the EA which corresponds to the maximum

in the *A(β)* dependence is not significantly affected by the piezo-strain. This behavior is in contrast with what has been observed so far – both in literature, [**117**], [**13**], [**130**] and in our experiments (see the previous section) where the EA shift was the dominant effect of interest.

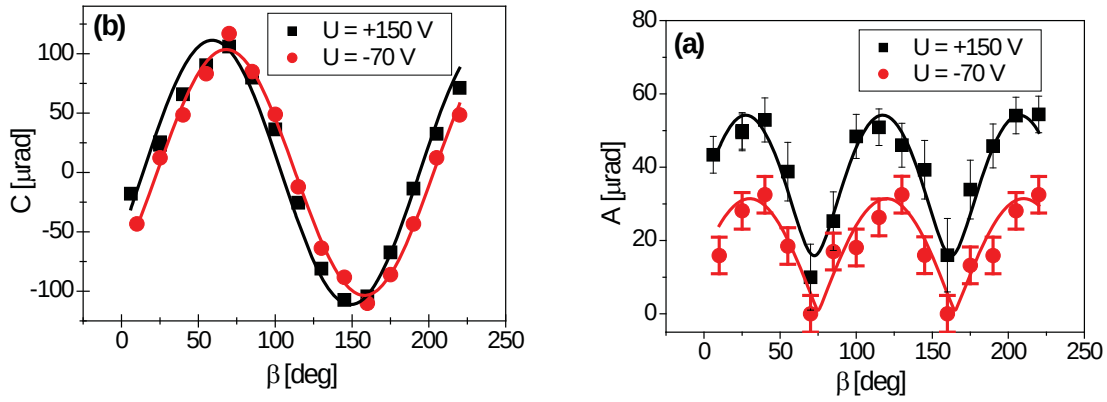

Fig. 3.52: Probe polarization dependence of the MO signal (a) precession amplitude *A* and (b) pulse function amplitude *C*, which were obtained by fitting to the data measured at the structure *F016_P1* at piezo voltage *U = +150 V* and *-70 V*. The lines are fits of the A(β) and C(β) to Eq. 3.29 and 3.32 with the following parameters:

For U = +150 V: *r = 0.998*, φ_M **= 117.4°**, *δφ = 1.48°*, $P^{PKE} \approx 5$ *and p = 10%.*

For U = -70 V: *r = 0.998*, φ_M **= 120°**, *δφ = 0.8°*, *PPKE ≈ 15 and p = 10%.*

The experimental conditions were as follows: T = 40 K, $\mu_0 H_{ext}$ = 30 mT applied at φ_H = 115°, I = 70 μJ.cm^{-2}.

Proposed explanation

The experimental observations presented above can be explained if we realize how the piezo-strain contributes to the total free energy *F* of the system. The original free energy of a (Ga,Mn)As sample with competing inherent cubic (K_c) and uniaxial anisotropies (K_{110}) [10] and no piezo-voltage applied, is denoted as F_0. According to Eq. (3.7), the piezo stressing gives rise to an additional uniaxial anisotropy F_Ω (described by K_Ω) which generally occurs in a different direction than that of the applied strain [**62**]. A negative voltage $U < 0$ creates *compressive strain* ($K_{\Omega C} > 0$), and consequently, F_Ω has its minimum at the position of Ω. On the other hand, U > 0 results in *tensile strain* ($K_{\Omega T} < 0$), and it has exactly the opposite effect.

Let us first assume that the direction *Ω* of the new anisotropy is parallel to the EA (φ_0) of the structure with no voltage applied ($\varphi_0 = \Omega$). Furthermore, the size of K_Ω is significantly smaller than the inherent anisotropies of the sample ($K_\Omega << K_c, K_{110}$). Such a situation is depicted in Fig. 3.53(a). Clearly, the presence of a new piezo-induced anisotropy modifies the depth of the free energy minimum [Fig. 3.53 (b)] and thus also the "*stability*" of the EA which in turn causes a change of the laser-induced magnetization precession amplitude (Chap. 3.4). For $U > 0$ ($K_{\Omega T} < 0$), the shallower minimum leads to precession amplification while $U < 0$ ($K_{\Omega T} > 0$) causes its quenching (see Fig. 3.49). As the minimum of F_Ω is aligned with a minimum of the original F_0, there is no piezo-voltage induced EA shift – see Fig. 3.52 (b). Furthermore, the small contribution of F_Ω cannot modify significantly the overall shape of *F*. This also means that the precession frequency *ω* remains unaffected by piezo stressing. This situation describes properly the behavior of the hybrid structure *F016_P1* at a low temperature (40 K) presented in this

[10] Though we do not know exactly the anisotropy constants of the F016 sample attached to the stressor, the free energy F_0 presented in Fig. 3.56 corresponds to any (Ga,Mn)As layer with comparable inherent anisotropies, which is a reasonable assumption for the F016 sample at 40 K (T_c = 96 K)

chapter (see Fig. 3.49-3.51). However, the assumption of the small K_Ω compared to the inherent anisotropies is crucial in this case. If it were not fulfilled, the modification of the shape of F and subsequent change of ω would follow – consistently with Eq. (3.32). This happens at elevated temperatures where the inherent anisotropies of the sample are weakened – see Fig. 3.51. (b)

The behavior of the hybrid structure becomes significantly different when the direction Ω does not correspond to the original EA of the (Ga,Mn)As layer ($\varphi_0 \neq \Omega$), even though K_Ω remains the same – see Fig. 3.53 (c). In this case, piezo-stressing leads not only to the change of the EA "*stability*" and corresponding amplification/quenching of the magnetization precession, but also to the overall modification of the shape of F, including a shift of its minimum – see Fig. 3.53(d). Consequently, both the position of the EA and ω is modified by piezo stressing. This more general situation arises typically in various experiments [117], [13], [130] and it was observed also in our TRMO signals – see Figs. 3.43-3.45.

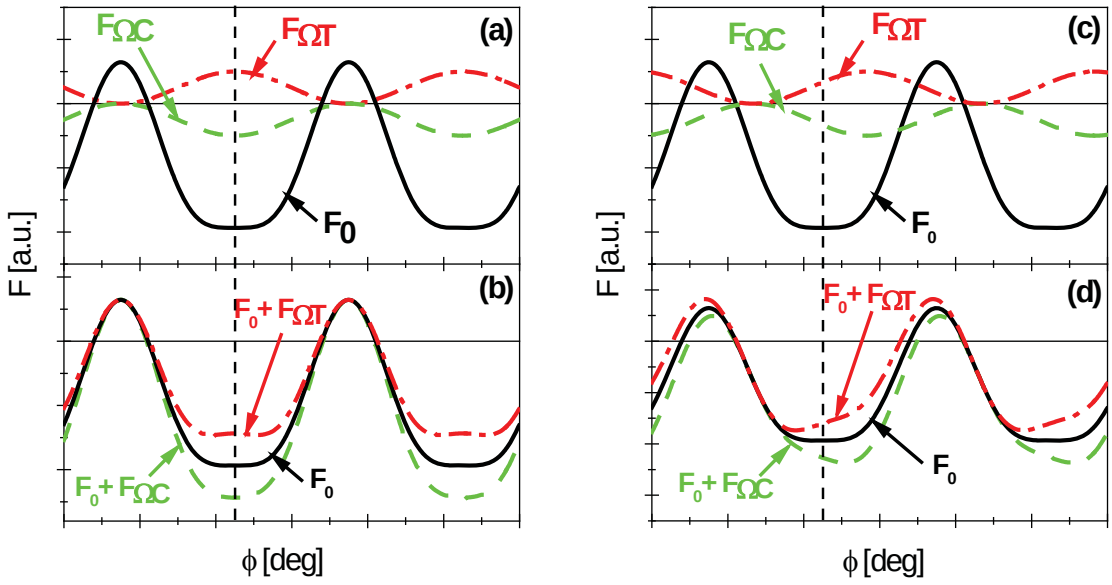

Fig. 3.53: Schematic depiction of the free energy F as a function of the orientation φ in the (Ga,Mn)As/piezo hybrid structure assuming (a), (b) the piezo-induced anisotropy (F_Ω) minimum oriented in the direction of the original easy axis of the structure (EA) and (c),(d) F_Ω is misaligned with respect to the original EA.
F_0 stands for the free energy of an arbitrary (Ga,Mn)As sample with competing inherent cubic and uniaxial anisotropies which corresponds to a hybrid structure with NO piezo voltage U applied, $F_{\Omega T}$ and $F_{\Omega T}$ denote contributions from the piezo-stressing: $F_{\Omega T}$ corresponds to a tensile strain (U > 0 V) and $F_{\Omega C}$ to a compressive strain (U < 0 V).

By adding the external magnetic field $\boldsymbol{H}_{ext}$ [described by Eq. (3.8)] to the system, the problem becomes more complex. Generally, at large negative piezo-voltages the internal anisotropy field forcing magnetization to align with the stressor axis (which is set close to the easy-axis of the unstressed epilayer) is significantly strengthened. With only a relatively weak additional external field, the changes in the magnetic anisotropy induced by the laser pulse are then not sufficient to trigger measurable spin precession. However, the direction of $\boldsymbol{H}_{ext}$ plays a crucial role. During our experiments $\boldsymbol{H}_{ext}$ was aligned with the sample easy axis ($\varphi_H = \varphi_0$). The non-monotonic behavior of $A(\boldsymbol{H}_{ext})$ [Fig. 3.50 (a)] and $A(U)$ (Fig. 3.51 (a)] which occurs solely for U < 0 could be then understood in terms of the misalignment between the strain direction φ_{str} and the external field φ_H. Furthermore, the small strain generated in the minor axis of the stressor (see the technological

section) that was omitted in the discussion can in principle have some influence on the $A(\boldsymbol{H}_{ext})$ and $A(U)$ dependencies.

Reproducibility

At the end we would like to briefly mention a problem connected with the reproducibility of the measurements described in the previous sections. In Fig. 3.54 we show the TRMO signals detected with $U = \pm 150\ V$ applied to the hybrid structure *F016_P3* which is nominally identical to the *F016_1* sample used in the previous section. All the other experimental conditions ($\boldsymbol{H}_{ext}$, β, I) were also the same as in the previous experiments, and the TRMO traces depicted in 3.54 (a) and (b) differ only by the position on the sample. We see that both the character of the magnetization precession, and thus also the sample magnetic anisotropy, can be strongly position-dependent. Consequently, the influence of the piezo-strain also varies as a function of position. The reason for this inhomogeneity lies probably in a local variation of the thermally-induced strain and/or additional strain induced by gluing. As follows from the previous results, even small changes in the strain can lead to a significant modification of the magnetization precession.

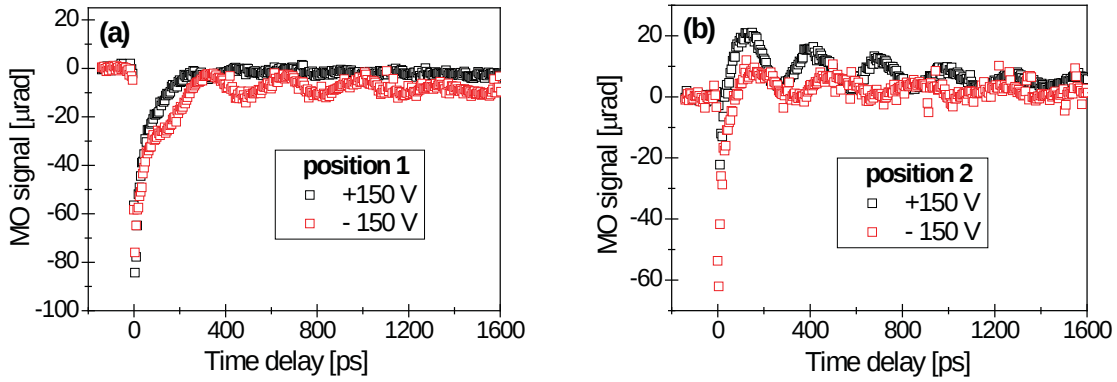

Fig. 3.54: Magnetooptical signal detected on the hybrid structure F016_P3 at two different positions (a), (b) for piezo voltages U = ± 150 V. The data were measured at T ≈ 40 K, external field $\mu_0 H_{ext}$ = 30 mT applied at φ_H = 115°, and probe beam polarization β = 25°.

In order to test the homogeneity of the (Ga,Mn)As layers, we performed a 2 dimensional spatial scan on two pieces of the *F016* samples attached to the same stressor by different adhesives. The first one is the above described *F016*_P3, glued by *EPO-TEK silver epoxy*, the second one is *F016_P2* glued by *UHU epoxy*. In Fig. 3.55 the spatial variation of the precession frequency which is a good indicator of the local magnetic anisotropy [see Eq. (3.32)] is depicted for the structure *F016_P2* (a) and *F016_P3* (b). The data were extracted from the TRMO traces detected under the same conditions as the signals presented in Fig. 3.54. Apparently, there is a significant local variation of the precession frequency for both samples. *F016_P3* glued by *EPO-TEK* seems to display better properties in terms of the homogeneity but the mechanical properties of the UHU epoxy make it preferable for practical use.

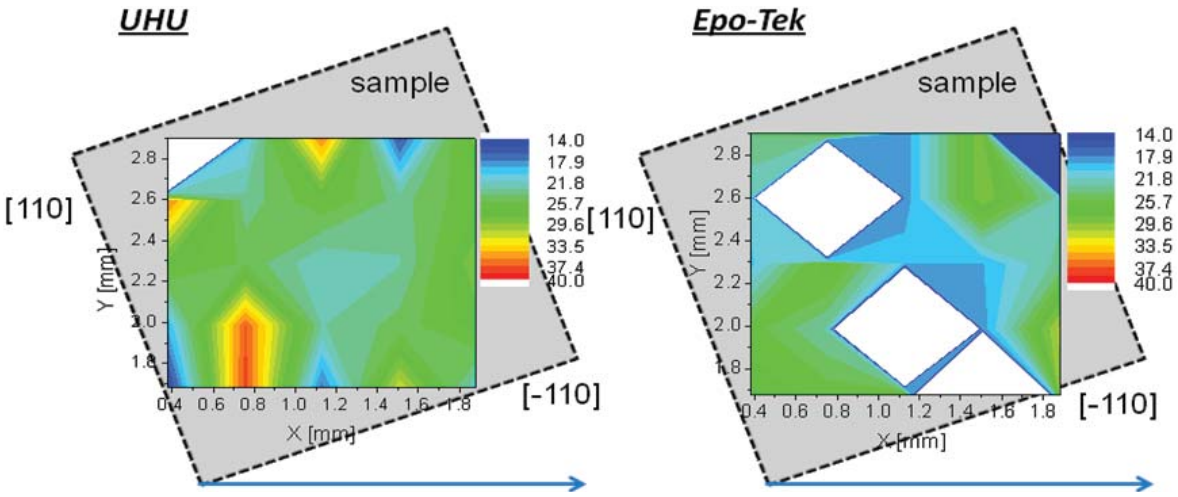

Fig. 3.55: Two-dimensional scan of the precession frequency, obtained from the TRMO signals detected on the hybrid structure (a) F016_P3 glued by UHU epoxy and (b) F016_P2 glued by EPO-TEK silver epoxy at U = + 150 V. The experimental conditions were identical to Fig. 3.54.

Finally, we would like to stress that despite the above described variation of the local magnetic anisotropy, the general character of our results, i.e. the possibility to efficiently control the magnetization precession by piezo-stressing, still remains unaffected. The problem of the sample homogeneity is of a purely technological nature, and it probably can be solved by better processing of the surfaces, using different stressors etc. However, such technological issues are beyond the scope of this work.

3.7.5 Conclusions

In this chapter we demonstrated an efficient voltage control of the laser-induced magnetization precession by using a piezo-stressing technique. It was shown that such control of the magnetization dynamics can be achieved not only by a manipulation with the easy axis direction, which is an already reported phenomenon, but also by the relative change of the free energy minimum depth ("*weakening/strengthening*" of the EA). The change of the magnetization precession amplitude is thus not accompanied by any EA shift, and the precession frequency remains also unaffected by piezo-stressing. This effect has not been observed so far and it demonstrates also the sensitivity of our magnetooptical detection method.

3.8 Photomagnetic processes and optical spin transfer torque

The experimental results that have been presented so far were dealing with various aspects of the magnetization precession that was induced by an energy transfer from the laser pulses that in turn affected magnetic anisotropy of the (Ga,Mn)As samples – either thermally or by the "*optomagnetic*" effects (see **Chap. 3.2**). However, there has so far been no evidence about the magnetization precession triggered solely by a direct transfer of the angular momentum of photoinjected carriers to the localized magnetic moments. In this part of the thesis we present the experimental results that clearly show the observation of this "*photomagnetic*" process in our TRMO experiments that manifest as a signal connected with the helicity of the excitation laser pulses. Furthermore, we also provide an explanation of the effect by means of the optical spin-transfer-torque theory that was recently published [135], [97].

3.8.1 Pump-helicity dependent magnetization precession – experimental results

The time-resolved magnetooptical (TRMO) measurements presented within this part of our work were performed on the hybrid (Ga,Mn)As/piezo structure *F016_P1*, described in detail in **Chap. 3.7.1**. In fact, the results in this chapter represent only different aspects of the TRMO measurement that were already shown in the **Chap. 3.7.4**. Therefore, the experimental conditions remain the same.[11]

The key results of this part of the work are presented in Fig. 3.56. In Fig. 3.56 (a) and (b) we plot separately the measured signals at two different piezo voltages U = ± 150 V for the σ^+ and σ^- circularly polarized pump pulses, detected with magnetic field $\mu_0 \boldsymbol{H}_{ext} = 30\ mT$. We observe a clear phase shift between σ^+ and σ^- that depends on the voltage applied to the piezo-stressor – it is exactly π for U = -150 V but different for U = +150 V. By subtracting the TRMO signals excited by circularly polarized (CP) pump pulses with opposite helicities we detect the helicity-dependent (HD) oscillations that have exactly the same precession frequency ω and damping time τ_G as the helicity – independent (HI) ones that are presented in Fig.3.56 (c). However, in contrast with the HI precession that was described in detail in the previous section, this signal is *not affected* by piezo stressing, as shown in Fig 3.56 (c) and (d).

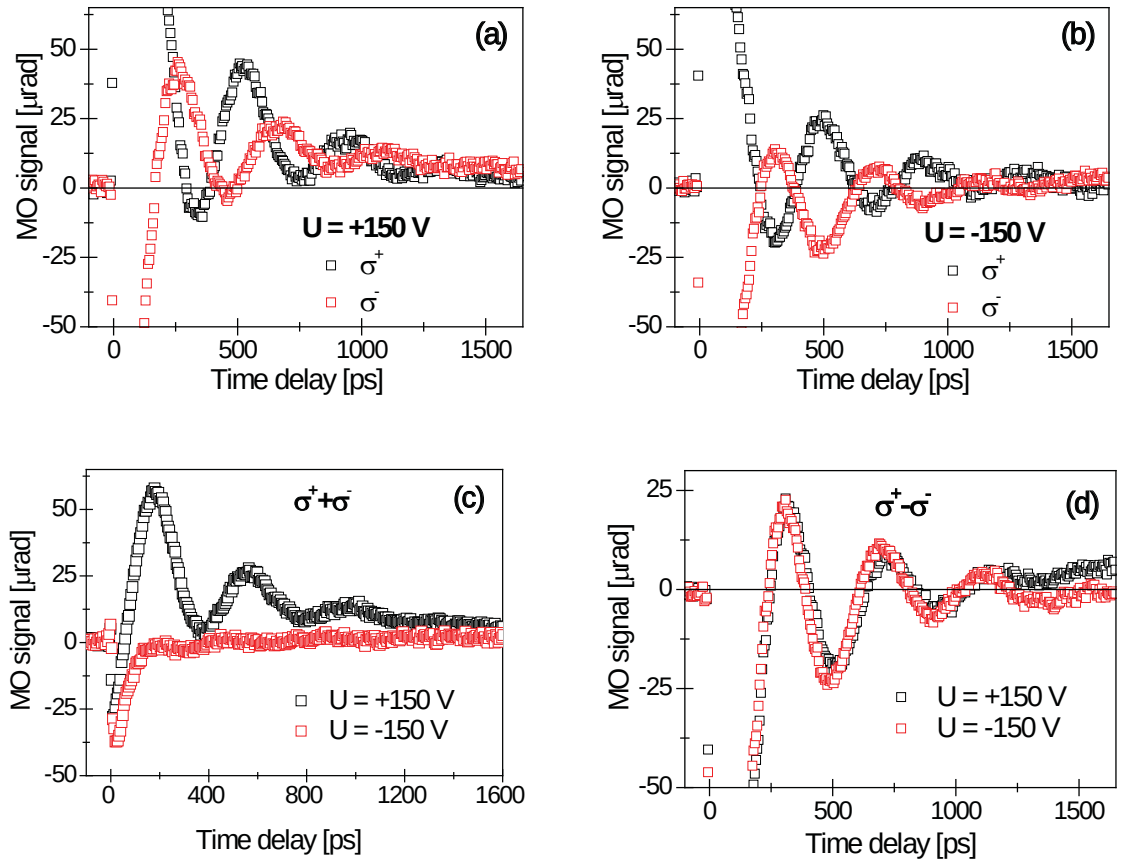

Fig. 3.56: Magnetooptical signal detected on the hybrid structure F016_P1 with circularly polarized σ^- and σ^+ pump pulses for different piezo voltages (a) U = + 150 V and (b) U = - 150 V applied to the stressor. (c) Helicity-independent part and (d) helicity-dependent part of the signals presented in (a),(b). Note that the helicity dependent signal is equivalent for both of the piezo voltages.
The data were taken at T ≈ 40 K, external field $\mu_0 H_{ext}$ = 30 mT applied at φH = 115°, probe beam polarization β = 25° and pump intensity I0 = 70 μJ.cm^{-2}

[11] This means that the magnetic field was applied in the same direction as the piezo-strain: $\varphi_H = \varphi_{str} = 115°$, temperature set to $T \approx 40\ K$ and pump fluence $I_0 = 70\ \mu J cm^2$ and pump pulse duration is ~300fs.

This feature is further highlighted in Fig. 3.57 (a) where the precession amplitude *A* is plotted against the piezo voltage *U* for both of the signal components. In Fig. 3.57 (b) we show the magnetic field dependence of the amplitude *A* of both HD and HI oscillations for $U = \pm 150$ *V*. While the HI precession differs significantly with the piezo stressing and it can be effectively quenched for an appropriate combination of *U* and $\boldsymbol{H}_{ext}$ [see Fig. 3.57 (a),(b)], the HD signal manifests the expected gradual decrease with $\boldsymbol{H}_{ext}$ and the $A(\boldsymbol{H}_{ext})$ dependence is equivalent for both of the piezo voltages. Therefore, we can conclude that the HD precession is *not* connected with the pump-pulse induced modification of the in-plane magnetic anisotropy, as was the case of the HI oscillation.

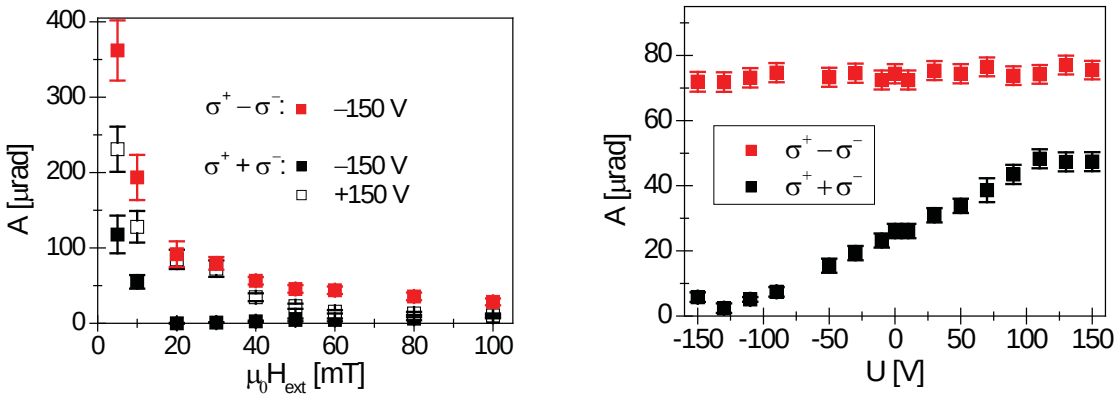

Fig. 3.57: Dependence of the precession amplitudes for helicity dependent (σ^+ - σ^-) and independent (σ^+ + σ^-) signals, which were obtained by fitting the TRMO signals to Eq. (3.21) (a) on the voltage U applied to the piezo-stressor at $\mu_0 H_{ext}$ = 30 mT, and (b) on the external magnetic field H_{ext};
I_0 = 70 µJ.cm^{-2}, $\varphi_H = \varphi_{str}$ = 115°, β = 25°.

In Fig. 3.58 we present the probe-beam polarization (β) dependence of the pulse function amplitude (C) and of the oscillation amplitude (A), extracted from the corresponding TRMO traces detected with U = +150 V applied to the stressor. As was already described in Chap 3.4, analysis of these data sets allows distinguishing the in-plane and out-of-plane part of the magnetization precession (120). $A(\beta)$ has the same oscillatory character for HD and HI excitations [Fig. 3.58 (a)] because, in both cases, it corresponds to precessing moments with time-dependent in-plane and out-of-plane components. On the other hand, $C(\beta)$ is constant for the HD signal [Fig. 3.58 (b)] while it is a harmonic function of β for the HI signal [Fig. 4(b)]. This shows that the non-equilibrium vector along which the magnetization precesses is tilted purely in the out-of-plane direction for the HD excitation and in the in-plane direction for the HI signal. Since we excite with a normally incident laser beam, this observation indicates that carriers generated by the absorption of the CP light (see **Chap. 1.4.1**) with their spins polarized in the out-of-plane direction act on the magnetization in the case of the HD signal and they are sensed mainly by the polar Kerr effect (PKE).

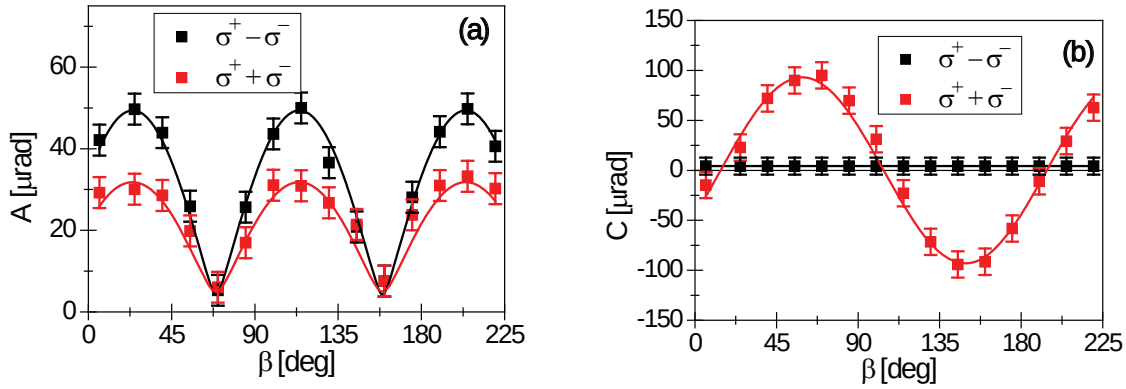

Fig. 3.58: Probe polarization (β) dependence of the amplitudes of (a) the oscillatory part (A) and (b) of the pulse function (C) for helicity dependent ($\sigma^+ - \sigma^-$) and independent ($\sigma^+ + \sigma^-$) parts of the TRMO signals detected for piezo voltage U = +150 V (φ_{str} = 115°), $\mu_0 H_{ext}$ = 30 mT (φ_H = 115°) and I_0 = 70 μJ.cm^{-2}.

Our assumption about the action of the spin-polarized carriers on the magnetic moments is confirmed again in Fig. 3.59. Clearly, the amplitude of the HD precession is proportional to the pump pulse intensity, i.e., to the spin-density of injected photo-carriers – see Fig 3.59 (a). From Fig. 3.59 (b) (inset) it also follows that the HD dependent precession is triggered only by the above-bandgap absorption ($h\nu$ = *1.64 eV*) of the circularly polarized light that results in a net spin polarization of the photoinjected carriers – i.e. there is no HD dependent signal excited by the sub-bandgap wavelengths ($h\nu$ = *1.44 eV).* Furthermore, Fig. 3.59 (b) also demonstrates that the previously reported inverse magneto-optical (MO) mechanism for exciting magnetization precession by CP light [**21**], [**30**] is not contributing in our experiments in (Ga,Mn)As. These effects do not require photon absorption [**21**] and the below band gap excitation energy is favorable for their generation. On the other hand, the angular momentum transfer requires above-bandgap excitation, and the carrier spin polarization is sensed by PKE. The direct PKE is comparable or even larger at 1.44 eV than at 1.64 eV, as shown in Fig. 3.59 (b). Therefore, if active above the bandgap at 1.64 eV, the inverse MO effect should be clearly detectable at 1.44 eV. No magnetization dynamics is, however, excited using the energy of 1.44 eV from which we conclude that the inverse PKE is not contributing in our experiments.

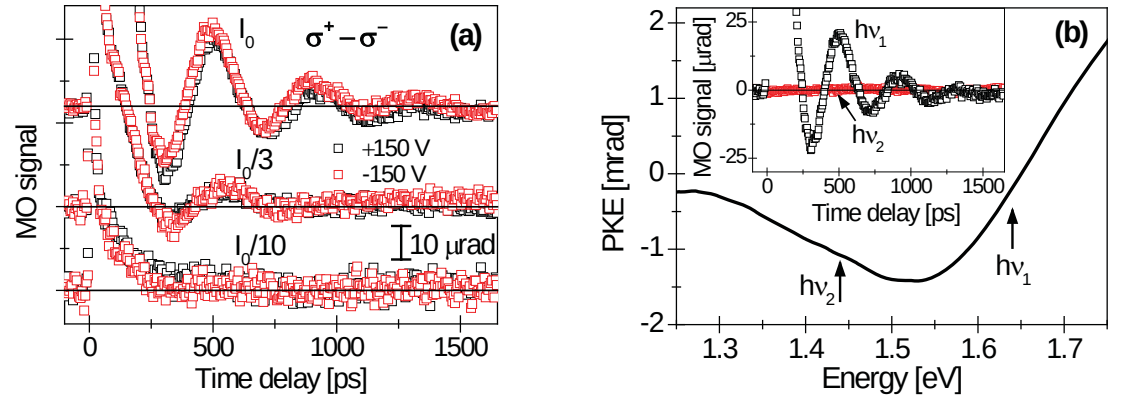

Fig. 3.59: (a) Intensity dependence (I_0 = 70 μJcm^{-2}) of the helicity-dependent signal for the piezo-voltages U = ± 150 V. (b) Energy dependence of the PKE magneto-optical coefficient [**122**]. The vertical arrows depict the photon energies $h\nu_1$ = 1.64 eV (above the semiconductor bandgap) and $h\nu_1$ = 1.44 eV (below the semiconductor bandgap) of the circularly polarized pump pulse that were used in the pump-and-probe measurements shown in the inset. Except for the variation of the photon energy of the pump pulse, the experimental conditions of the measurements shown in the inset are the same as in (a). $\varphi_H = \varphi_{str}$ = 115°, β = 25°, $\mu_0 H_{ext}$ = 30 mT.

To conclude this section, we stress that the measured oscillation frequencies and Gilbert damping constants for the polarization independent and helicity-dependent excitations are identical. Independently of whether the excitation is due to the in-plane shift of the magnetic easy axis or due to the transfer of the angular momentum from the photoinjected carriers, the precessing moments are the same in both cases. While the mechanism connected with the laser-induced change of the magnetic anisotropy has been already extensively studied (see **Chap. 3.2.3**), the precession induced by the angular momentum transfer is a brand new phenomenon. The reason why it has been overlooked so far lies in the fact that the investigated (Ga,Mn) As epilayers were typically very strong in-plane magnets and the HI precession was therefore a dominant contribution to the signal. However, after gluing the (Ga,Mn)As layer to the piezo-stressor and cooling down to a low temperature, the additional biaxial tensile strain ($\sim 10^{-3}$) that is generated (see **Chap. 3.7.3**) results is a significant reduction of the out-of-plane magnetic anisotropy of the (Ga,Mn)As (see comparison with the bare (Ga,Mn)As epilayer in [**125**]). This in turn leads also to a strong enhancement of the HD signal, which is 2.8 times larger than the HI one even with no voltage applied to the stressor. Further application of the piezo voltage (U = -150 V) allows to cancel out the HI precession which improves the "visibility" of the HD precession to the maximum.

Finally, we would like to note that even though the HD signal is relatively weak in the bare (Ga,Mn)As epilayers, it was reliably detected in the majority of the (Ga,Mn)As samples belonging to the "optimized set" [**20**] and thus it can be regarded as a rather general effect.

3.8.2 Optical spin transfer torque theory

In the previous section we showed experimentally that coherent magnetization precession can be induced in (Ga,Mn)As by a transfer of the angular momentum from the spin-polarized carriers. The spin polarized carriers with the concentration $\delta n = \delta p << p_0$ are generated by an above-bandgap excitation by circularly polarized light that results in the optical orientation (see **Chap. 1.4.1**). The angular momentum transfer is enabled by the exchange coupling between the carrier and Mn spins. The exact mechanism the "optical-spin transfer torque" (OSST), which is a phenomenon that was addressed several years ago [**135**], [**97**] and which is described in relation to the TRMO experiments in [**125**]. Here we only briefly summarize its main cornerstones.

In the OSST theory, a coupled dynamics of the magnetization vector **M** and net photo-carrier spin density **s** that occurs due to the exchange interaction between the two spin systems is described by a set of equations of motion – see [**97**], [**125**]. In the geometry of our experiments, with normal incidence of the laser pulse and in-plane easy-axis of (Ga,Mn)As, the equilibrium **M** is perpendicular to direction of the carrier spin orientation (**n**), while the carriers are photo-injected at a rate **P**. There are two limits to the magnetization motion (Fig. 3.60) that arise from the difference between the precession time and the spin life-time of the photo carriers.

The first limit concerns the photo-injected electrons and it is shown in Fig. 3.60 (a). The photo-electrons precess due to the exchange field produced by the high density ferromagnetic Mn moments on a timescale of ≈ 100 fs [**97**]. The major source of spin decoherence of the photo-electrons in (Ga,Mn)As is the exchange interaction with fluctuating Mn moments and the corresponding decoherence time is ≈ 10 ps [**97**]. Furthermore, the photo-electron decay also contributes to the spin life-time and the corresponding time scale is in the order of ≈ 10 ps, as follows from the reflectivity measurements [see Fig. 3.13 (b)]. The photo-electron spins therefore precess many

times around the exchange field of ferromagnetic Mn moments before they relax. As the rate of the out-of-plane tilt of $\mathbf{s}_0$ due to precession around the exchange field is precisely compensated by the rate of photo-injection of out-of-plane oriented electron spins, a steady-state spin density $\mathbf{s}_0$ emerges that is oriented in the sample plane, perpendicular to both **n** and **M** [see Fig. 3.60 (a)]. The spin density $\mathbf{s}_0$ that effectively acts as a "magnetic field" exerts in turn a torque on **M**. The direction of this *optical spin transfer torque (OSST)* is again perpendicular both to $\mathbf{s}_0$ and **M** – analogically to the situation described in **Chap. 3.2.1**. The fast precessing component of the spin of a photo-carrier relaxes to the environment at a random orientation, producing a zero net momentum transfer to the environment and the whole momentum $\mathbf{s}_0$ is transferred to the change of **M**.

The situation is markedly different in the opposite limit, where the spin-life time τ of the photo-carriers and their precession time are comparable. As the precession times are typically very short, this approximation represents a small τ limit [see Fig. 3.60 (b)]. It can be shown [**125**] that the generated steady state spin density of photo-carriers $\mathbf{s}_0$ is oriented out-of-plane and its magnitude scales with τ. The corresponding torque exerted on the magnetization **M** is therefore much smaller than in the previous case and most of the angular momentum of the photo-carriers is transferred to the environment, not to **M.** The precession time of holes in (Ga,Mn)As is ≈10's fs and the spin life-time of holes, dominated by the strong spin-orbit coupling, is estimated to ≈1-10 fs [**97**]. The holes are, therefore, better approximated by this relaxation time limit, and they have negligible influence on the overall magnetization dynamics compared to the photo-electrons.

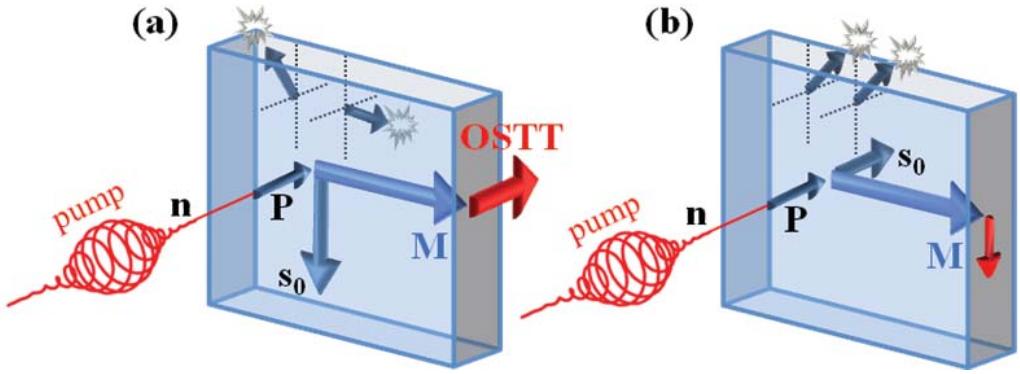

Fig. 3.60: Schematic illustration of the optical spin transfer torque [**125**] (a) Schematic illustration of the optical spin transfer torque in the large spin life-time limit. The rate P of the photo-carrier spin injection along light propagation axis n (normal to the sample plane) is completely transferred to the optical spin transfer torque (OSTT) acting along the normal to the sample plane on the magnetization M of the ferromagnet. The steady state component of the injected spin density s_0 is oriented in the plane of the sample and perpendicular to the in-plane equilibrium position of M. The fast precessing component of the spin of a photo-carrier (small upper arrows) relaxes to the environment at a random orientation, producing a zero net momentum transfer to the environment. This picture applies to photo-electrons in (Ga,Mn)As. (b) A weak torque acting on M produced by photo-carriers with a short spin life-time. Most of the spin angular moment is transferred to the environment in this limit. For photo-holes in (Ga,Mn)As this picture is more relevant than the picture of the strong optical spin transfer torque shown in panel (a).

The OSST generated by the photo-injected electrons acts during the pump pulse duration which is in our experimental setup ~ 300 fs. However, the coherent magnetization precession was detected on a significantly longer timescale – the oscillation period is about 0.4 ns. The action of the OSST is, therefore, reflected only in the initial phase and amplitude of the oscillations. The precession of magnetization itself is described by the Landau-Lifshitz-Gilbert (LLG) equation [(Eq. (3.13)] with the effective field $\boldsymbol{H}_{eff}$ comprising of the anisotropy and external magnetic

field. The same $\boldsymbol{H}_{eff}$ is described the helicity-independent magnetization dynamics induced by the anisotropy modification (**Chap. 3.3**) and hence follows also the equivalency of the precession frequency and Gilbert damping of both the dynamics observed in our experiments.

In Fig. 3.61 a schematic representation of the magnetization dynamics is depicted in the sole presence of the OSST effect – i.e. with NO helicity-independent precession[12]. In contrast with the helicity-independent precession (see Fig. 3.20 in **Chap. 3.4**), there is no slow motion of the magnetization easy axis caused by the laser pulses. The initial tilt of the magnetization is out-of-plane in the direction of the OSST, consistently with the probe-polarization dependence.

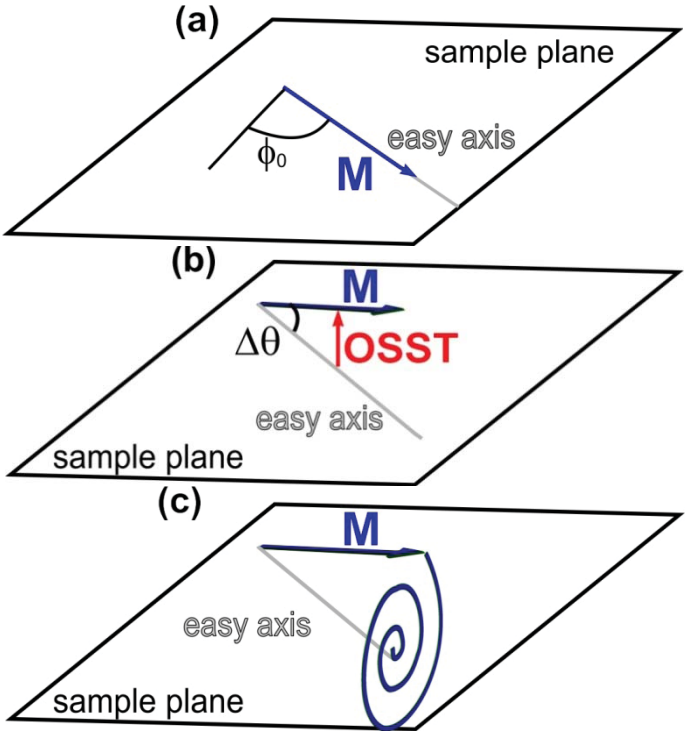

Fig. 3.61: Schematic illustration of the coherent magnetization precession induced by an optical spin transfer torque (OSST). (a) In equilibrium, the magnetization M points in the easy axis direction which is oriented at the angle φ_0 from the [100] direction. (b) Within the duration of the pump pulse (~ 300 fs) the OSST that is perpendicular to the sample plane acts on M, causes its out-of-plane tilt by an angle $\Delta\theta$. (c) After the OSST subsides, the magnetization starts to precess and returns to its equilibrium position. This dynamics corresponds to the situation where signal connected with the anisotropy change is completely suppressed (i.e. by piezo stressing).

Finally, we note that the optical spin transfer torque not only qualitatively explains the main feature of our helicity-dependent magnetooptical signals but it can also quantitatively account for the precession amplitude and initial phase. This can be achieved by introducing the OSTT into a LLG equation numerical modeling. This procedure exceeds the scope of this work and the details can be found in [125] (and the corresponding Supplementary materials).

3.8.3 Conclusions

In conclusion, we observed a new type of magnetooptical signal which is connected with the helicity of the excitation light. We attributed this signal to magnetization precession induced by a transfer of angular momentum from the photo-excited electrons to the net magnetization and we addressed the corresponding theory of optical spin transfer torque. We point out that bringing the spin transfer physics into optics introduces a fundamentally distinct mechanism from the previously reported thermal and non-thermal laser excitations of magnets. Bringing optics into the field of spin transfer torques decreases by several orders of magnitude the timescales at which these phenomena are observed.

[12] This situation corresponds for example to the data shown in Fig. 3.51 for U = -150V, where the helicity-independent precession is completely suppressed by piezo-stressing.

4. NON-MAGNETIC DEVICES

In the beginning of this thesis we discussed the basic concepts of spintronic devices. We stressed that for any spintronic device to work, an efficient injection and detection of spin-polarized carriers was needed, and that it was crucial for these carriers to maintain their spin polarization. In the past decade, significant attention was paid to the studies of spin transport phenomena using a whole range of experimental techniques. Electrical detection of spin polarization is of special importance for application in real spintronic components. However, present techniques rely either on "destructive methods" based on the interface with a ferromagnet .or they are limited to the spin injection area . A non-local, non-destructive method is still needed. It has been shown recently that this can be achieved by measuring the transverse voltage signal directly in the semiconductor channel, which is proportional to the spin polarization of the injected carriers [**5**]. Such detection is possible due to a new phenomenon that belongs to the Hall effects (HE) family. The so called "Spin-Injection Hall effect" (SIHE) is directly related to the spin HE and anomalous HE, both of which have already been observed [**139**] and addressed theoretically [**140**] SIHE, however, provides a new, non-local version of Hall measurements, and thus it opens a way to new spintronics applications. The systems exhibiting SIHE form an ideal basis for the fabrication of the spin field effect transistor (S-FET), a key spintronic component, whose satisfactory implementation has not yet been realized, as they enable efficient gating of the carrier spin states. Achieving this goal without any ferromagnetic parts that were required in the original scheme (see **Chap. 4.4**) is a significant step leading to a purely non-magnetic concept of spintronics.

4.1 Introduction to Spin-Injection Hall Effect

In this chapter we briefly introduce the basic physics of the Spin-Injection Hall Effect (SIHE), a new effect that was first observed in two-dimensional planar photovoltaic cells in 2009 [**5**]. SIHE is a member of the spin-dependent Hall effects family which we will present in the first part of this chapter. We will further proceed to a brief description of the systems exhibiting SIHE, based on their particular symmetries of spin-orbit coupling. The final section of this chapter will be dedicated to the actual principles of SIHE.

4.1.1 Spin-dependent Hall effects

The family of Hall effects takes its name after the original Hall effect (HE), i.e. the appearance of a voltage drop perpendicular to the current direction in a material subject to an external magnetic field. This family now covers a whole range of magneto-transport phenomena among which those connected with the carrier spin polarization are of special importance for spintronics applications. Our work is closely related to three of the spin-dependent HEs – anomalous (AHE), spin (SHE) and inverse spin (iSHE) Hall effects, schematically depicted in Fig. 4.1. The anomalous Hall effect [Fig. 4.1. (a)] occurs in ferromagnetic materials where electric currents are spin polarized [**139**]. The carriers are deflected in opposite directions perpendicular to the charge current according to their spin polarization resulting in a transverse charge accumulation. On the contrary, in non-magnetic materials the presence of the unpolarized charge current leads to spin accumulation perpendicular to the current direction that is known as spin Hall effect (SHE) [**35**], [**42**]. Finally, in analogy to SHE, the inverse effect (iSHE) causes a transverse charge

accumulation if a spin-polarized current flows through a non-magnetic material [**41**]. Unlike AHE and SHE, iSHE requires an efficient spin injection which was provided in the original experiment by a transition with a ferromagnet.

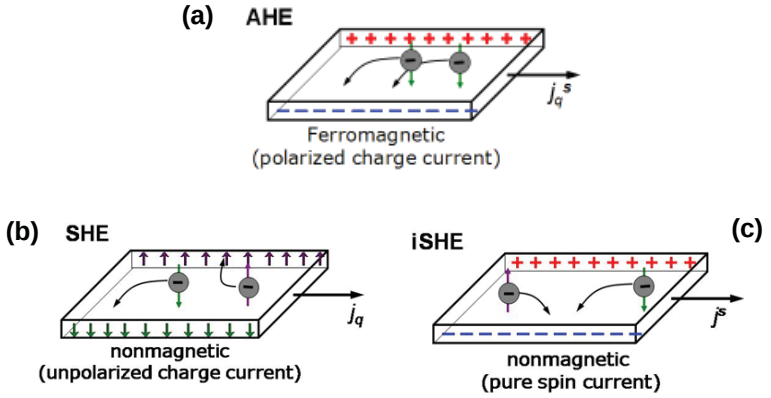

Fig.4.1. Schematic depiction of spin-dependent Hall effects (a) anomalous Hall effect (AHE), (b) spin Hall effect (SHE) and (c) inverse spin Hall effect (iSHE). The Hall effects differ in the nature of the generating currents, where j_q is a pure charge current, j^s pure spin current and j_q^s spin-polarized charge current.

All the above described effects share the origin in the asymmetric, spin dependent deflections of the carriers that occur due to the presence of a strong spin-orbit (SO) coupling. The deflection mechanism can be either *intrinsic* connected with interband coherence [**140**], or *extrinsic* that results from spin-dependent scattering on impurities [**141**], [**142**]. Consequently, a material with strong SO interaction is needed in order to observe a significant Hall response. However, the spin-lifetime is usually short in materials with strong SO coupling due to the enhancement of D'Yakonov-Perel relaxation mechanism [**15**]. This problem can be overcome in two dimensional semiconductor systems with a special type of symmetry, where a long-lived spin state can exist.

4.1.2 Persistent spin helix

As was already discussed in Chap. 1.3, two types of SO coupling are present in the two dimensional electron/hole gas (2DEG,2DHG). The *Rashba* SO coupling is connected with the structure inversion symmetry breaking, while *Dresselhaus* SO coupling relates to the bulk inversion asymmetry. The corresponding form of the Hamiltonian [Eqs. (1.2) and (1.3)] in the presence of SO coupling in the 2DEG/2DHG is [7], [**143**]:

$$H_{2DEG} = \frac{\hbar^2 k^2}{2m} + \alpha\left(k_y\sigma_x - k_x\sigma_y\right) + \beta\left(k_x\sigma_x - k_y\sigma_y\right) \tag{4.1}$$

where m represents the electron/hole effective mass, k is the momentum, $\sigma_{x,y}$ components of Pauli spin matrices, and the constants α, β characterize the Rashba and Dresselhaus interactions, respectively. It was predicted several years ago that if these two types of SO coupling are comparable in strength (i.e. $|\alpha| = |\beta|$), the SU(2) symmetry, that is usually broken in the bulk material by the presence SO interaction, is renewed. As the SU(2) symmetry is connected with spin conservation [7], the spin relaxation in such systems can be strongly suppressed [**143**], [**144**]. This leads to an enhancement of spin lifetime in a particular direction, while in the perpendicular direction a long-lived precession state emerges. This "*persistent spin helix*" (PSH) state was observed only recently using optical transition grating technique [4] but direct electrical detection has been missing so far.

The PSH state can be intuitively understood if the SO interaction is regarded as an effective electric field [7] that is linear in the quasi-particle wave vector $\boldsymbol{k}$ in the first approximation. A schematic visualization of these fields is presented in Fig. 4.2 [**5**]. The *Rashba* field is perpendicular to the $\boldsymbol{k}$ vector [Fig. 4.2 (a)], while the Dresselhaus field is aligned with **k** in the

major crystallographic directions [Fig. 4.2 (b)]. If we assume the same relative strength of both contributions and $\alpha = -\beta$, the SO field is oriented along the [110] direction independently of the $\boldsymbol{k}$ vector orientation, and its magnitude scales only with the projection of $\boldsymbol{k}$ to the [1-10] direction (Fig. 4.2). Consequently, the spins oriented e.g. along [010] direction ("up" spins) injected at certain point precess exactly the same angle after passing the same distance. This manifests as a collective helix mode with a wavelength of:

$$\lambda_{spin\text{-}helix} = \pi\hbar/(2m\alpha) \tag{4.2}$$

The life time of the spins in such a helical mode is in principle infinite, assuming the spin-dependent scattering and cubic contribution to the Dresselhaus term can be neglected [5], [4]. Neither spin-independent scattering processes nor electron-electron interactions influence the PSH mode [4].

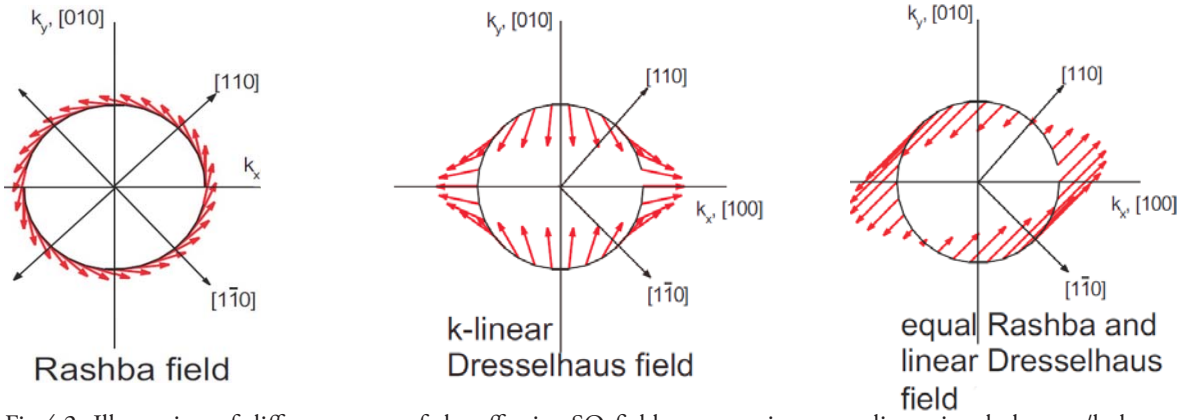

Fig.4.2. Illustration of different types of the effective SO fields, present in a two dimensional electron/hole gas system. (a) Rashba field, (b) Dresselhaus field and (c) combined field for $\alpha = -\beta$. [152]

The above described concept relates to a collective behavior of the spin wave density matrix [143]. Under the given conditions (see the next chapter, and Ref. [5]), it can be used in a single-particle analogy to account for the origin of SIHE.

4.1.3 Physics of SIHE

In the previous two sections we discussed two different aspects of SO coupling action on spin dynamics – the presence of the spin-dependent Hall effects and the symmetry of the SO field that can result in the emergence of the persistent spin helix mode. Combining these two effects within one system, one can observe a new type of Hall effect.

If spin-polarized carriers (electrons) are injected into a non-magnetic structure, they are deflected according to their spin polarization, which results in a charge accumulation perpendicular to the current direction – as schematically illustrated in Fig. 4.3. This leads to SIHE, which is in fact a combination of spin and anomalous HE. Moreover, if the carrier spins can precess around the SO field, the resulting voltage drop across the 2DEG channel varies along the current direction in a way that corresponds to the spin precession.

The origin of the Hall response can be understood in terms of the anomalous Hall effect [132]. The origins of such an effect can be both extrinsic and intrinsic, as described in **Chap. 4.1.1.** In the structures where SIHE was first observed [5], the carriers experience strong scattering, and the carrier transport occurs in the diffusive regime. Therefore, the *extrinsic* origin of the

HE connected with the spin-dependent impurity scattering is expected to dominate (see ref. [5] and supplementary material for more details). However, the spin-dependent scattering that dominates these systems disturbs the conditions for the observation of the PSH state, which would normally decrease the spin lifetime of the carriers significantly. In order to observe the long-lived spin precession, channels comparable in thickness with the precession length are used. This leads to a restriction of the carrier $\boldsymbol{k}$ vectors to a quasi- one-dimensional motion, and the long-lived precession can be generated even for SO fields where the $|\alpha| = |\beta|$ condition is not exactly fulfilled [5]. The spin precession length L can be tuned mainly by changing the strength of the Rashba field (see Eq. 4.2) by quantum well engineering [8]. The expected values are L ≈ 1-2 μm in our devices, which is suitable for electron-lithography fabrication of the quasi – 1DEG channels (see **Chap. 4.2**).

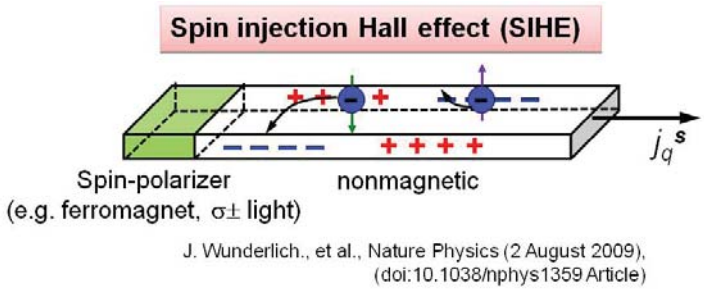

Fig.4.3. Schematic depiction of the spin-injection Hall effect. The spin polarized current jqs flows through a non-magnetic channel, where the spins precess around the SO field and they are deflected according their spin polarization. [151]

The possibility to change the α/β ratio by tuning α using an external electric field opens the way to manipulate electrically the spins in the channel, which forms a basis for the S-FET type device that will be described in **Chap. 4.4**.

4.2 Systems for SIHE detection

In order to detect the precessional signal connected with the Spin-Injection Hall effect (SIHE), a system with tunable SO interaction is needed, where an efficient injection of the spin polarized current is available. The co-planar two dimensional electron (2DEG)/hole (2DHG) gas photodiodes [42], [145] turned out to be ideal systems for the observation of SIHE. In this chapter we summarize the basic properties of these devices. Moreover, we present the selected results related to SIHE that have been published so far.

4.2.1 Planar photovoltaic cell design

The co-planar two dimensional photo-diodes were invented for a measurement of the spin accumulation in the spin Hall effect [42]. In the original concept, the device worked under forward bias as a light-emitting diode (LED), and the circular polarization of the electroluminescence indicated spin polarization of the recombining electrons. In the SIHE design, the same devices were used in the reverse bias regime as photodiodes, and a spin-polarized photocurrent was generated after an illumination of the PN junction. Let us now describe the devices used in this work in more detail.

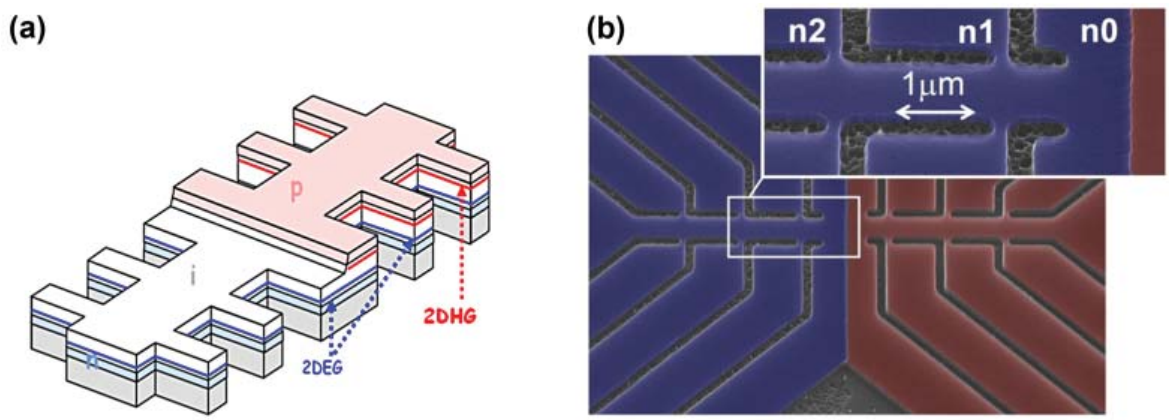

Fig. 4.4. Schematic diagram (a) and SEM image (b) of the planar photovoltaic cell used in this work. The red part in (b) indicates the P-type material of the diode, while the blue one corresponds to the N-type. [5].

Our photodiode consists of the 2DEG and 2DHG vertically offset with respect to each other, as schematically depicted in Fig.4.4 (a). The basic wafer is a vertical p-i-n modulation doped GaAs/AlGaAs heterostructure [**146**] grown by molecular beam epitaxy, where δ-doping for donors (*Si*) and modulation doping for acceptors (*Be*) were used. The change in doping enables manipulation with the SO field which is tuned so that $\alpha \approx$ *0.01-0.03 eVÅ* and $\beta \approx$- *0.02 eVÅ*. The exact configuration of the wafer (*A1671#SI)* used in this work is summarized in Table 4.1. Note that the wafer is identical to the one used later in Ref. [**43**].

No.	Material	Thickness in nm	Doping in cm^{-3}
1	GaAs	5	$N_a = 1.0 \times 10^{19}$
2	$Al_{0.5}Ga_{0.5}As$	50	$N_a = 8.0 \times 10^{18}$
3	$Al_{0.3}Ga_{0.7}As$	3	undoped
4	GaAs	90	undoped
5	$Al_{0.3}Ga_{0.7}As$	5	undoped
6	$Al_{0.3}Ga_{0.7}As$	δ-doped $N_d = 5.0 \times 10^{12}$ cm^{-2}	
7	$Al_{0.3}Ga_{0.7}As$	300	undoped
8	AlGaAs/GaAs SL	500	undoped
9	GaAs	-	undoped

Table 4.1. Wafer configuration of the PN structure [**43**]

The device structure was prepared by electron-beam and optical lithography from the above described wafers [see Fig. 4.4 (a) and (b)]. The Hall bars, approximately 10 nm wide and separated by 2 μm, and the channel (~ 1 μm wide) were patterned by electron-beam lithography. Consequently, the N-region of the PN junction was prepared after removing a P-type layer by chemical wet etching. The Ohmic contacts were fabricated by an evaporative deposition of AuZn. More details about the structure preparation can be found in Ref. [**43**] (supplementary material).

4.2.2 Optical excitation and electrical detection

The working principle of the 2DEG/2DEHG planar photovoltaic cell has already been briefly described in Chap. 2.2, and it is further illustrated in Fig. 4.5 (a). The room temperature VA characteristics [Fig. 4.4. (b)] confirms the photodiode functionality of the device. The bias voltage V_B is applied between the source and the drain (i.e. $V_B = Vs$, $V_d = 0$). Clearly, the device is strongly rectifying in darkness because of the charge depletion of the PN junction. The leakage current is 4 orders of magnitude lower than the forward-bias current [see inset of Fig. 4.5. (b)]. When the laser spot is focused on the PN junction, a photocurrent (I_{PH} ~ 1 mA in our experimental setup) flows along the reverse-biased

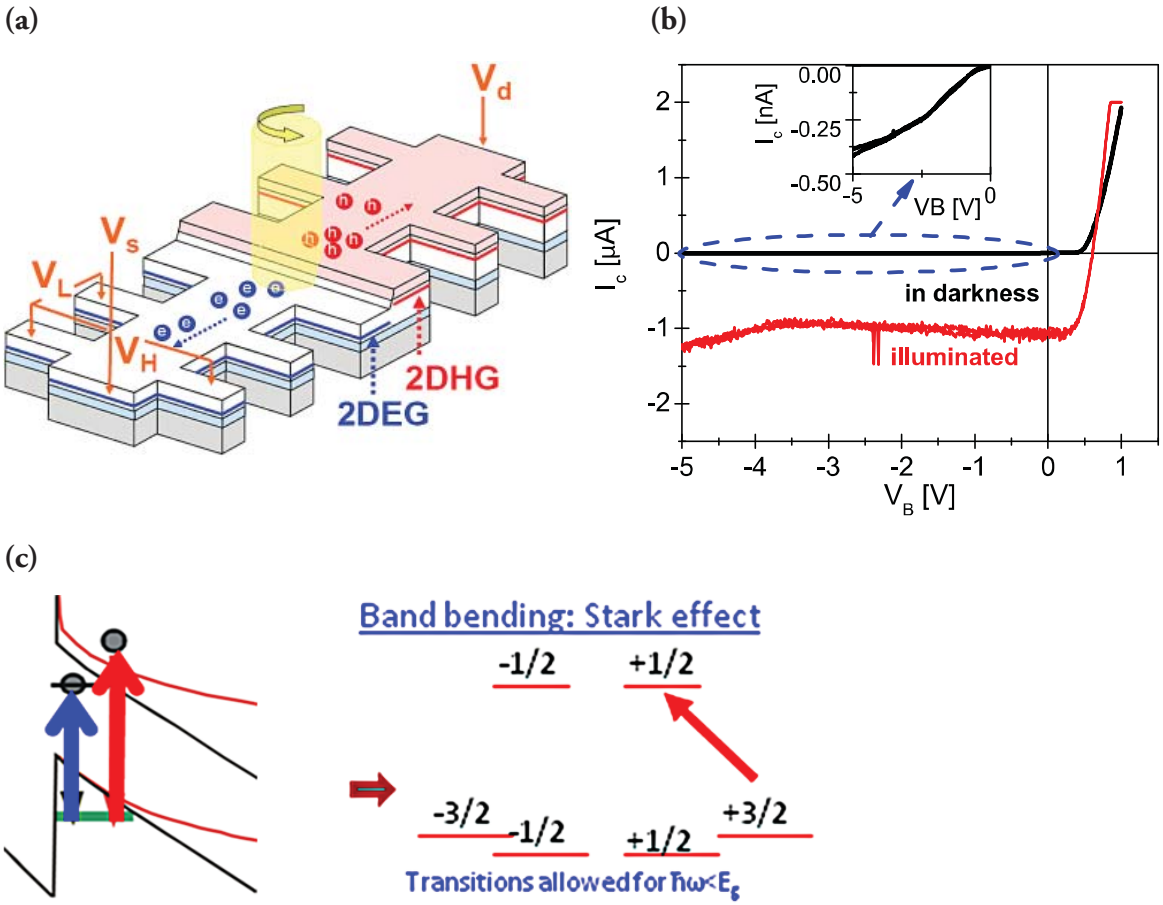

Fig.4.5. (a) Schematic depiction of the working principle of the co-planar photodiode used in the experiments. Here Vs, Vd denote the source and drain voltage, and VL, VH are the longitudinal and transverse (Hall) voltages [5] (b) Room-temperature VA characteristics of the photodiode in darkness (black line) and after the illumination of the PN junction (red line) (c) Illustration of the optical transitions at the PN junction of the (reverse biased) two dimensional p-i-n heterostructure [152].

channel. When circularly polarized light is used for the optical injection, the resulting current is strongly spin-polarized due to the optical selection rules (see **Chap. 1.4**), with the spin oriented parallel with the plane of incidence of the laser light (i.e. perpendicular to the sample plane). In the quantum wells (QWs), the heavy and light hole bands are spin-split (see **Chap. 1.4**) due to quantum confinement. The built in potential of the PN junction, together with the reverse bias applied to the structure, result in a red shift of the electron and hole states (see **Chap. 7.2**

of Ref. [8]) and in a change of the triangular QW symmetry. The symmetry change leads to further spin-splitting – see schematic depiction in Fig. 4.5 (c). Consequently, the resulting spin polarization can be up to 100% when light with sub-band gap wavelength is used.

The spin polarized electrons and the holes generated optically at the PN junction, are driven to the N and P regions, respectively. The transverse voltage (V_H) and the longitudinal voltage (V_L) are detected. If present, the transverse voltage drop is connected with a given Hall effect. The value of V_L is recorded together with the photocurrent I_{PH} in order to account for the change in longitudinal resistance. For details about the experimental setup and conditions see **Chap. 2.2**.

The major difference between the devices presented in this work and those used in the original SIHE detection concept [5] is in the character of the PN junction and the resulting carrier excitation. In the original work, the 2DEG in the P-type region was fully depleted due to the presence of acceptor levels and thus only a small area in the vicinity of the PN junction was optically active [42], [5]. On the other hand, in our devices the 2DEG levels in the P-region are still occupied and the whole P-region is optically active. Before we show the possibilities offered by such devices, let us first briefly summarize the results obtained in the first type of structures.

4.2.3 Experimental observation – previously published results

Two major findings led to the observation of the spin-injection Hall effect – the fact that the anomalous Hall effect can be used as a probe of the local magnetization in ferromagnets [147] and that a spin imbalance occurs when the non-polarized current is sent through a non-magnetic medium, which is known as a spin Hall effect [42], [35] (see **Chap. 4.1.1**). The key experiments showing the presence of the spin-injection Hall effect (SIHE) are summarized in Ref. [5] and in the corresponding supplementary material. Here, we point out only the major observations that are important with respect to our work.

The experiments in Ref. [5] were carried out using the identical setup and the same conditions as those shown below. Figure 4.6 (a) shows a simultaneous electric measurement of the transverse voltage drop on Hall bar 0 *(HB0)*, partially overlapped with the carrier injection area, and *HBs 1-3* that are further away from the PN junction (see Fig. 4.4.). The Hall voltage is recalculated to Hall angles α_H according to Eq. (2.6) (see **Chap. 2.2.2**).

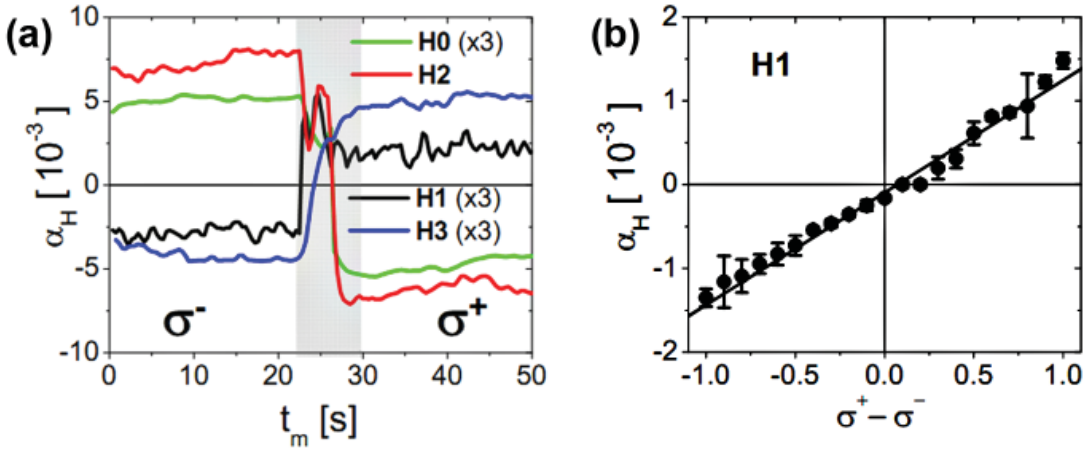

Fig. 4.6. (a) SIHE signals recorded for Hall bars 0 – 3. The transient region corresponds to a manual rotation of the waveplate which changes the polarization state [5] (b) Experimental Hall angles measured at Hall bar 1 at different polarization states of the excitation light. The reverse bias is V_B = – 10 V, laser wavelength is λ = 850 nm and temperature T = 4 K. [5]

A signal, which corresponds to tens of Ohms in transverse resistance R_H, was detected. The variation of the signal measured for individual Hall bars (separation of the Hall crosses is 2 μm) is typical for the presence of SIHE. Moreover, the signal changes sign upon reversal of the circular polarization (CP) helicity which confirms its origin in the polarized spin injection. Furthermore, the Hall angle scales linearly with the degree of light circular polarization [Fig. 4.6 (b)] in analogy with AHE effect that is linear in magnetization of the ferromagnet [**139**]. The temperature dependence of the Hall signal measured at *HB2* [Fig. 4.7 (a)] in combination with the linear dependence on the degree of CP [Fig. 4.6 (b)] clearly indicates that that the SIHE device can be used as a purely electrical polarimeter up to high temperatures.

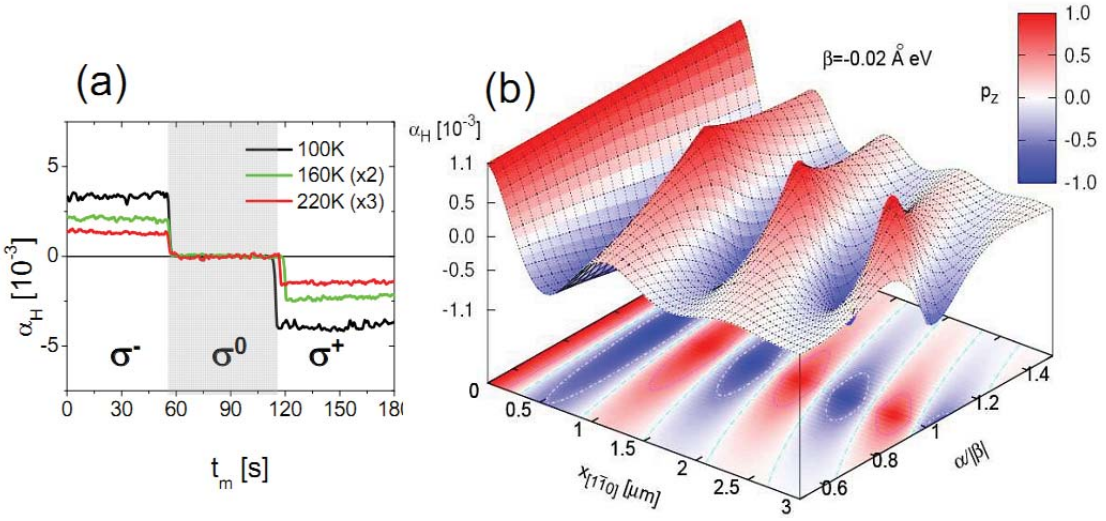

Fig.4.7. (a) SIHE signals recorded for Hall bar 2 at T = 100 K, 160 K and 220 K. The experimental conditions are the same as in Fig. 4.6 (b) Microscopic theory of SIHE assuming spin-orbit coupled band structure of the experimental 2DEG system. The colour-coded surface shows the proportionality between the Hall angle and the out-of-plane spin component. [5]

The theoretical description of the SIHE signal is based on the fact that the micrometer length scales typical for the non-equilibrium spin dynamics are much larger than the mean free path in these 2DEG systems (10-100 nm). Thus the steady-state spin dynamics can be computed and the corresponding Hall response can be inferred using the AHE theory. The results of the modeling are shown in Fig. 4.7 (b). We see that precessional Hall response at the scales of several micrometers is present even for $\alpha \neq \beta$. All calculated spin precession and spin coherence lengths, as well as the magnitude of the Hall angles are consistent with the experimental values.

4.3 Experimental results on SIHE

In this chapter we summarize the results concerning the detection of SIHE in the 2DEG/2DEHG planar photovoltaic cell described earlier. First, we introduce several basic SIHE measurements (**Chap. 4.3.1**) similar to those published in Ref. [5] in order to show consistency with the previous measurements, and to present the basic characteristics. The main focus of the experimental work is reported in **Chap. 4.3.2**, where direct electrical detection of the spin precession is demonstrated using SIHE. Finally, the effect of an additional electric field on the SIHE signal realized by an unpolarized charge current is described in **Chap. 4.3.3**.

Each subsection begins with a note about the method of signal processing, and then the actual experimental results are presented. All the measurements were performed by the method

described in **Chap. 2.2** and **4.2**. Unless noted differently, the experimental conditions were as follows: laser light of wavelength $l = 850\ nm$ and intensity J_0 was used to excite the photocurrent of $I_{PH} \approx 1\ mA$ under the reverse bias of $V_B = -10\ V$. The voltage drop on the Hall bars 1 (≈ 1.3 μm from PN junction) and 2 (≈ 2.6 μm from PN junction) was detected at the temperature of T = 5 K, and the Hall resistivity was calculated according to Eq. (2.5)

4.3.1 Preliminary experiments on SIHE

A. Data analysis

The data shown in this section were obtained by recording the difference between the transverse Hall voltages U_H detected with s^+ and s^- circular polarization of the excitation laser light, as the SIHE signal is known to change sign upon the excitation helicity reversal (see Fig. 4.6). The helicity was modulated at the frequency of 50 kHz by a photoelastic modulator (PEM, see Chap.2.2). The reference of the PEM was connected to lock-in amplifiers that detected amplitude U_{Rmeas} and phase φ_{meas} of the transverse Hall voltages at the individual Hall bars. However, this signal comprises both the real SIHE signal and the polarization-independent background modulated at 50 kHz. This background signal, which appears as an artificial offset in the measured data, comes probably from the PEM power supply and cannot be easily removed in the experiment. Therefore, in the actual measurement, we first detected the amplitude and phase of the transverse voltage obtained after the excitation with linear polarization σ^0 ($U_{Roff,}$ φ_{off}) – when the SIHE signal is not present, and then we switched to circular polarization ($U_{Rmeas,}$ φ_{meas}) – see Fig. 4.8 (a). The temporal stability of the measured signal over the 200 s measuring interval provided us with the information about the error in the estimation of the Hall voltage.

In order to extract the real SIHE signal ($U_{Rsig,}$ φ_{ig}) from the measured data, a simple analysis has to be performed. In Fig. 4.8 (b) and (c), the schematic depiction of the detected signal with and without offset is presented. Note that the main axes represent the reference system of the lock-in amplifier. With no offset present during the measurement, naturally $U_{Rmeas} = U_{Rsig}$ and $\varphi_{meas} = \varphi_{sig.}$ On the other hand, the offset influences both the phase and the amplitude of the signal. Following the cosine law, the extraction of the real SIHE signal amplitude is relatively straightforward:

$$U_{Rsig} = \sqrt{U_{Roff}^2 + U_{Rmeas}^2 - 2U_{Roff}\,U_{Rmeas}\,\cos\left(\varphi_{meas} - \varphi_{off}\right)} \qquad \textbf{4.3}$$

The amplitude U_{Rsig} describes properly the Hall signal magnitude, which is sufficient for the current and voltage dependence presented in this chapter. However, SIHE is characteristic by the phase changes between the individual Hall bar signals (see **Chap. 4.2.3**), for which the phase of the real signal should be taken into account. This procedure is relatively complicated for the preliminary data obtained here, but it can be overcome experimentally, as will be shown in the next chapter. Finally, we note that for the dependence of the Hall signal on the excitation position (section C), the signal phase is accounted only in a qualitative way. We assume the real signal large enough compared to the offset, and we take $\varphi_{meas} = \varphi_{sig.}$

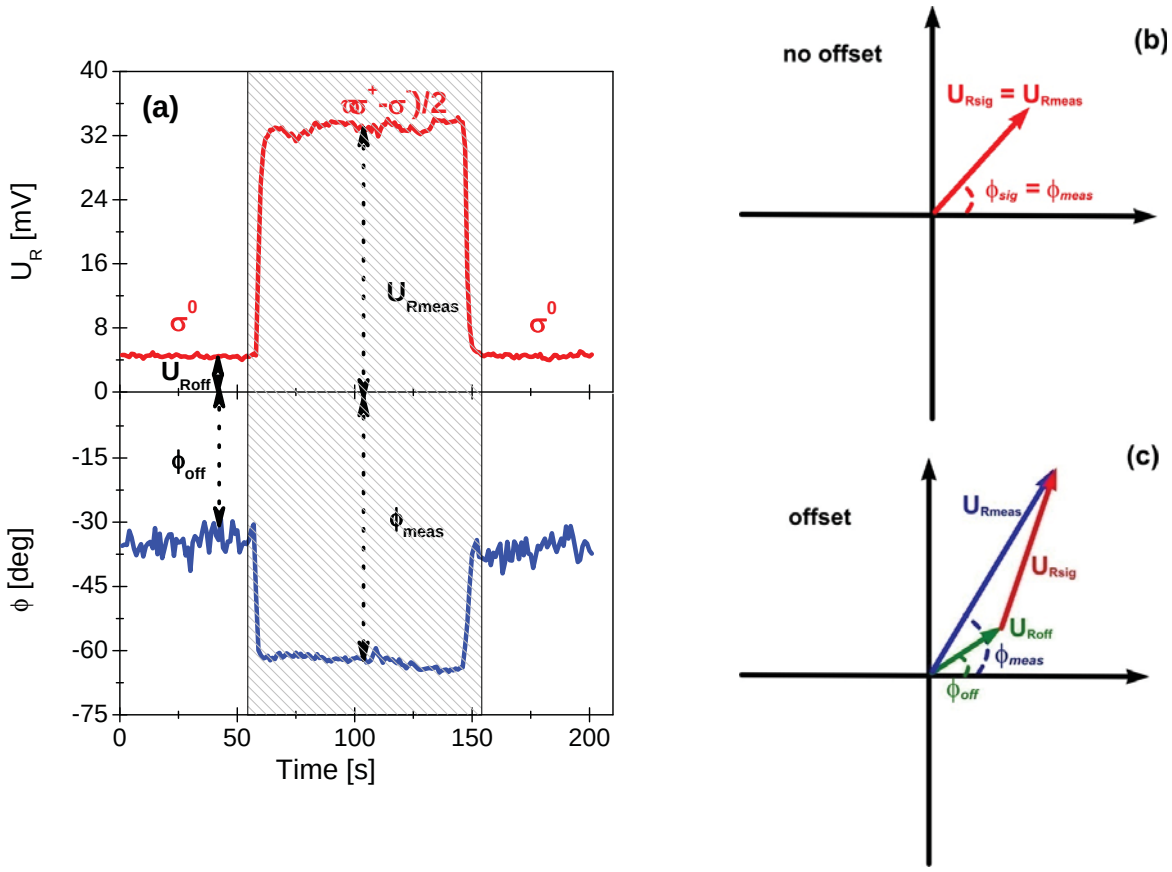

Fig.4.8. (a) Sample data detected on the Hall bar 1 at the reverse bias voltage VB = -5 V and photocurrent IPH ≈ 1 μA. Upper panel shows the signal amplitude excited by linearly polarized (U_{Roff}) and circularly polarized (U_{Rmeas}) light. The lower panel plots the corresponding phases (φ_{meas}, φ_{off}). (b) Schematic depiction of the signal with no offset and (c) with the offset in the reference frame of the lock-in amplifier.

B. Current and voltage dependence

In this section we show the character of the SIHE signal depending on the excitation conditions. In Fig. 4.9 (a), the amplitude of the Hall resistance is depicted as a function of the injected photocurrent I_{PH}, which is related to the excitation laser intensity, at a fixed reverse bias of V_B = *-10 V.* Clearly, the increase of the photocurrent leads to a stronger Hall resistance detected at both Hall bars, which is a natural consequence of the higher number of spin polarized carriers generating the Hall effect. The Hall resistance and photocurrent detected at the same Hall bars are plotted against the reverse bias in Fig. 4.9. (b). While the current remains unaffected in a relatively wide range of voltages, the Hall signal increases in a monotonous way with the bias voltage magnitude. We can thus conclude that the increase of the number of photoinjected spins [Fig. 4.9. (a)] cannot be the only reason for such behavior. One possible explanation is the influence of the reverse bias on the PN junction and amplification of the Stark effect that leads to higher spin polarization of the photocurrent. The impact of the reverse bias on the PN junction is apparent also from the degradation of the temporal stability of the signal detected at higher V_B, which is reflected in larger measurement errors in Fig. 4.9. (b).

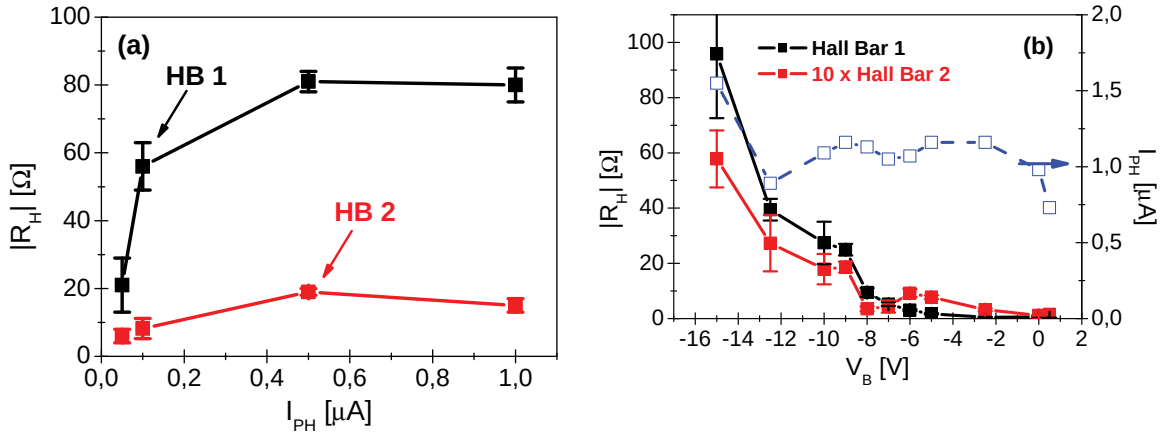

Fig.4.9. Amplitude of the Hall resistance detected at Hall bars 1 and 2 (HB1, HB2) as a function of (a) injected photocurrent, for a fixed bias voltage V_B = -10 V, and (b) bias voltage. In part (b) the dependence of the photocurrent on the bias voltage is plotted as well. The temperature was set to T = 5 K, laser wavelength λ = *850 nm*.

Finally, we would like to note that each of the dependencies presented in Fig. 4.9 (a) and (b) was measured after a readjustment of the injection laser spot to the PN junction. The apparent mutual inconsistence between these two data sets in terms of the Hall resistance can be explained by the strong position dependence of the measured signals, as shall be shown in the next chapter. Nevertheless, the overall trends detected within one measurement remain valid.

C. Dependence on the excitation position

In contrast with the original type of devices [5], where the spin-injection point was strictly defined by a narrow PN junction, in our photodiodes the whole unetched region is optically active. In Fig. 4.10., the experiment where the injection spot was shifted from the etched N part towards the unetched P region is shown. The Hall signals from the two subsequent Hall bars 1 and 2 are recorded simultaneously at each fixed injection point. The resulting Hall resistances, calculated as a projection to the *X* axis of the lock-in amplifier reference frame, are presented in Fig. 4.10. (b). Here *x* indicates the distance along the channel which is measured from the PN junction, where negative values correspond to the N region and positive to the P region. The behavior of the Hall resistance differs significantly in both parts. In the N region only a small signal that is independent of the spot position remains. This signal can be attributed to the anomalous Hall effect caused by the spin polarized electrons in the place of spin injection [5]. In contrast, in the P region the signals from both Hall bars show a periodical variation, with the period of ~ 1 μm. Furthermore, the signals detected at neighboring Hall bars – that are separated by approximately 1.3 μm – have the phase of this periodical variation reversed. All these facts strongly suggest that we observe spin precession directly using SIHE.

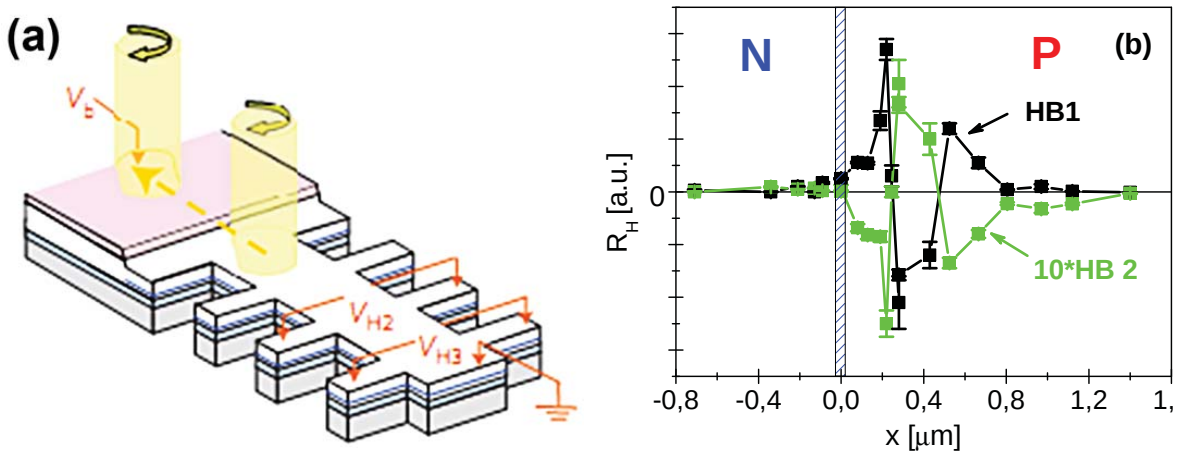

Fig.4.10. (a) Schematic depiction of the experiment where the spin polarized carriers are injected at different positions in the device. (b) Hall resistance detected at different positions x of the injection laser spot along the device channel. The positive values of the x correspond to the P region shift while the negative x is in the N region. The experimental conditions are as follows: $V_B = -10$ V, $I_{PH} = 1$ μA, $T = 10$ K.

4.3.2 Direct spin precession experiments

The experiment described in the end of the previous chapter indicates a new path to detect the long-lived spin precession state directly in the space domain by a continuous shift of the injection point along the device channel. However, in order to properly account for the phase changes of the Hall signal typical for spin precession, it is necessary to perform a careful analysis of the measured data.

A. Data analysis

The issue of the correct inclusion of the Hall signal phase in the presence of the artificial background modulated at the frequency of the PEM used for the polarization modulation can be relatively complicated, as discussed earlier. In this section we show that the problem can be overcome experimentally taking advantage of SIHE symmetry. Note that in order to obtain the signals that are readily phase-sensitive, we always detect X, θ combination of the lock-in amplifier output, in contrast with the previous chapter where the R, θ pair was recorded.

It has been shown that the signal due to SIHE reverses sign upon change of the circular polarization (CP) helicity of the light that injects the spin polarized carriers (see **Chap. 4.2**). If no artificial background is present, the signals for both excitation helicities can be schematically depicted as in Fig. 3.11 (a). In particular, in the absence of the background these signals are phase shifted by 180° in the reference frame given by the lock-in amplifier and the PEM reference ("zero phase" at lock-in). notation is the same as in the Chap. 4.3.1 (A), and U_{xsig} stands for the x projection of the detected signal. The situation becomes more complicated if the background has to be taken into account, as shown in Fig. 4.11 (b) and (c). Clearly, an additional artificial phase shift is introduced between the signals measured (U_{meas}) for the opposite helicites. We therefore rotated the reference frame so that the x axis of the new system is aligned with the *correct* SIHE signal. The corresponding x projections (U_{xsig}, U_{xmeas}, U_{xoff}) will be always related to this new reference system in further discussion. Following the illustration in Fig. 4.11 (b) we see that for the excitation by the σ^+ circularly polarized light, the projection $U_{xmeas}^{\sigma+}$ of the measured signal can be expressed as:

$$U_{xmeas}^{\sigma+} = U_{xsig} + U_{Roff} \cos\Psi \tag{4.4}$$

where U_{roff} and Ψ are the amplitude and phase of the background signal in the new reference frame. For the opposite polarization helicity the σ , only the real SIHE signal changes sign but the background remains unaffected [see Fig. 4.11 (c)]

$$U_{xmeas}^{\sigma-} = -U_{xsig} + U_{Roff} \cos\Psi \tag{4.5}$$

Hence it directly follows that the real signal U_{xsig} can be obtained by taking difference between the signals excited by the opposite circular polarization:

$$U_{xsig} = \frac{1}{2}\left(U_{xmeas}^{\sigma+} - U_{xmeas}^{\sigma-}\right) \tag{4.6}$$

Concerning the experimental realization of the above described procedure, the rotation of the reference frame into the direction of the SIHE signal can be roughly done by inserting an artificial phase shift to the lock-in amplifier so that the *x* component of the measured signal is maximized. For large signals – background neglected The helicity reversal of the circular polarization is then achieved by manually rotating the λ/2 wave plate located in front of the PEM by 45° (see Fig. 2.4 for the experimental setup).

Finally, we stress that the value and the sign of U_{xsig}, as obtained from Eq. (4.6), contain full information about SIHE and it is completely independent of the background. Therefore, it can be directly used to calculate the Hall resistivity.

B. Spin polarized charge current experiment

In this section we summarize the basic results obtained after sweeping the excitation spot of diameter ~ 1-2 μm along the unetched P-region of the photodiode and passing the spin-polarized *charge* current along the device channel. The electrical configuration, schematically illustrated in Fig. 4.12 (a), is the same as the one used in the original SIHE experiments discussed above. By shifting the focused laser spot, the injection point of the photocarriers is smoothly changed with respect to the position of the Hall crosses. The shift was realized by manually moving the objective placed on a piezo stage that focuses the spot on the device.

Sample data detected under typical experimental conditions (i.e. V_B = *-10 V, T = 4 K*) are presented in Fig. 4.12 (b). The upper part of the panel shows the Hall resistivity detected at Hall bar 1 for both helicites of circular polarization (CP) of the incident light. Clearly, the traces are almost anti-symmetrical, which indicates SIHE origin of the signal with a rather low influence of the background on the measured data. In the lower part, the real SIHE trace extracted according to Eq. (4.6) is plotted against the distance from the PN junction, which is estimated according to the onset of the photocurrent. Note that the slowly changing background (see section C) was subtracted from the data. Consistently with Fig. 3.10, the precession starts at the PN junction, and its period is around 1 μm which, when compared to the theoretical models [see Fig.4.7 (b)], again indicates the spin-precession origin of the signal.

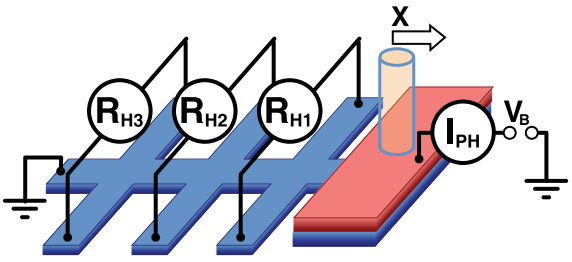

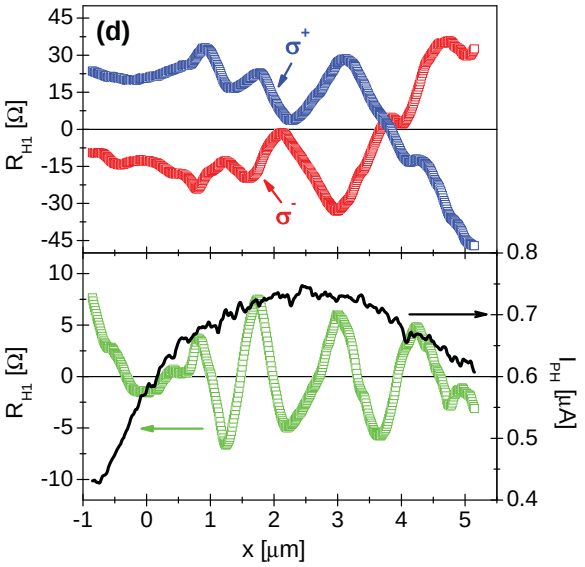

Fig.4.12. (a) Schematic depiction of the experimental setup in the "spot-sweeping" experiments, where RH denotes the Hall resistance, V_B the bias voltage and IPH the photocurrent (43) (b) Hall resistance detected at Hall bar 1 for the two helicities of the excitation light (upper panel) and the corresponding SIHE signal obtained from the data using the Eq. (4.6), together with the photocurrent IPH (lower panel), as a function of the excitation position x. Increasing x means shifting the spot further from the Hal bars. Here bias voltage V_B = -10 V, T = 4 K

In Fig. 4. 13, we further demonstrate the major characteristics of the precessional signal. The signals detected at the three subsequent Hall bar pairs (HB1-HB3) are shown in Fig. 4.13 (a) and (b) for low (4 K) and room (300 K) temperature measurement, respectively. The experimental conditions are the same as in Fig. 4.12. Clearly, the traces recorded at the three HBs are phase shifted with respect to each other, and their periods are equivalent. Furthermore, the oscillatory signals persist up to room temperature with their periods virtually unaffected, as further highlighted in Fig. 4.13 (c), where the corresponding Fourrier transforms of the HB1 and HB2 signals detected at 4 K and 300 K are presented. We see that the precession period is $\Lambda = (1.3 \pm 0.3)$ μm, which is in a good agreement with the theoretical prediction for our systems [see Fig. 4.7 (b)]. The period does not change significantly with temperature. This is in accord with the previous observation of the persistent spin helix state (see [4], Fig. 6), where the expected shift in the precession wave vector when changing the temperature from 300 K to 5 K is about ~ 20%, which is below our resolution.

All the above described features lead to the conclusion that we are able to directly observe the spin precession in the space domain.

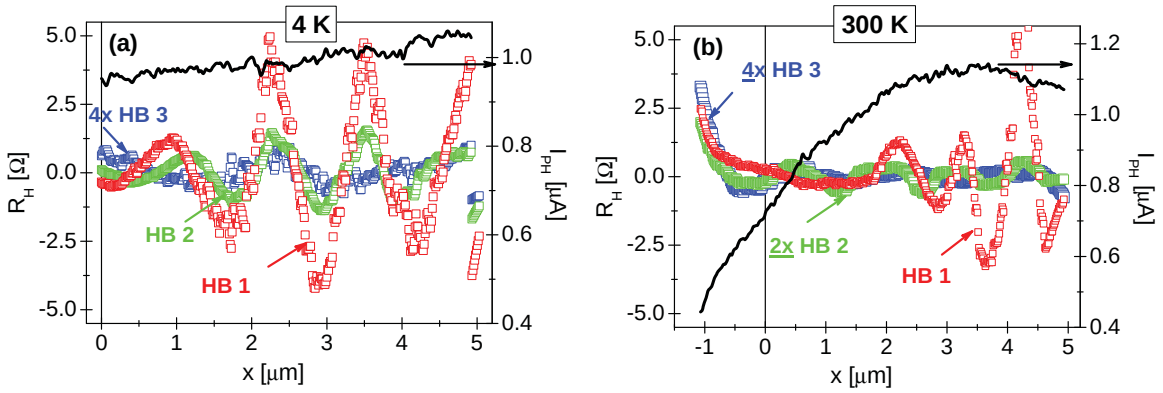

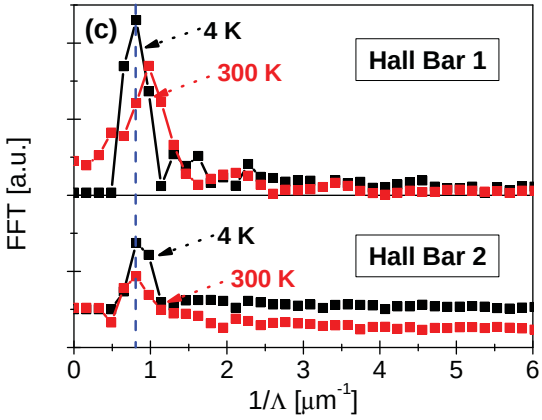

Fig. 4.13. Hall resistance and photocurrent detected at the three Hall bars nearest to the PN junction (HB 1- 3) as functions of the injection position x at (a) low temperature T = 4 K and (b) room temperature T = 300 K.

(c) Fourrier transform of the corresponding signals detected at HB 1 (upper part) and HB 2 (lower part). Here the bias voltage is V_B = -10 V.

C. Pure spin current experiment

The experimental method presented above is directly sensitive to the spin dynamics through SIHE. Consequently, it is not bound to the presence of the charge current but only to spin imbalance. We performed an experiment analogical to the one described in the previous section but with the charge current drained before it reaches the first detection Hall bar (see Fig. 4.14 (a) for illustration of the experimental configuration). In such case, only a pure spin current [41], [148] that can be understood as a diffusion of the spin polarized carriers in the opposite directions is injected into the channel and generates the Hall effect, which in this case can be understood as an inverse Spin Hall Effect (iSHE, see **Chap. 4.1.1**)

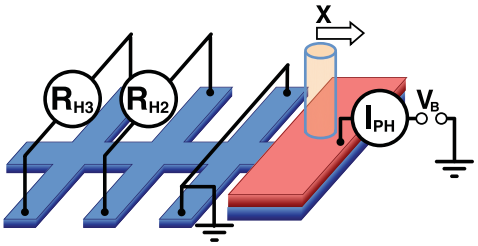

Fig. 4.14. (a) Schematic depiction of the experimental setup in the "spin current" experimental configuration, where the photocurrent IPH is drained at Hall bar 1 (43) (b) Hall resistance detected as a function of the injection spot position at Hall bar 2 for the pure spin current and spin-polarized charge current geometries (upper part) and corresponding photocurrents (lower part). The position x = 0 indicates the PN junction.

Here the bias voltage V_B = -5 V, T = 4 K.

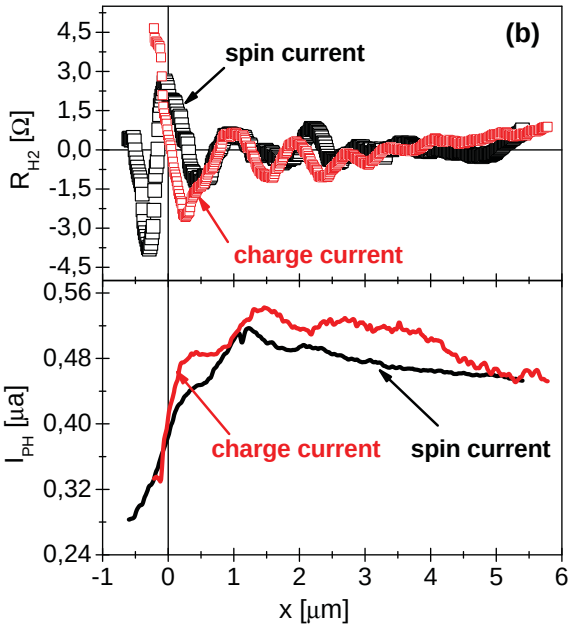

The experimental results demonstrating the generation of the Hall signal by the pure spin current are presented in Fig. 4.14 (b). Hall resistance was detected at Hall bar 2 which is approximately 4 μm away from the PN junction. Two sets of data were detected under the same experimental conditions (i.e. reverse bias V_B = *-10 V,* temperature T = *4 K,* and photocurrent I_{PH} = *1 μA*). The first set was measured in the "charge current" geometry [Fig. 4.12 (b)], while the second one in the "spin current" geometry [Fig. 4.14 (b)], and we see that there is no significant difference neither in the amplitude nor the phase of these two signals. All the differences can

be explained in terms of the precision of the spot alignment, to the PN junctions. Thus we can conclude that Hall effect detection of the pure spin current can be realized in the same way as the detection of the spin-polarized charge current in our experimental setup.

D. Experimental issues

In the end of this part of the work dealing with the "spot-sweep experiments" we address two major experimental issues connected with laser beam adjustment that can strongly influence the measured data.

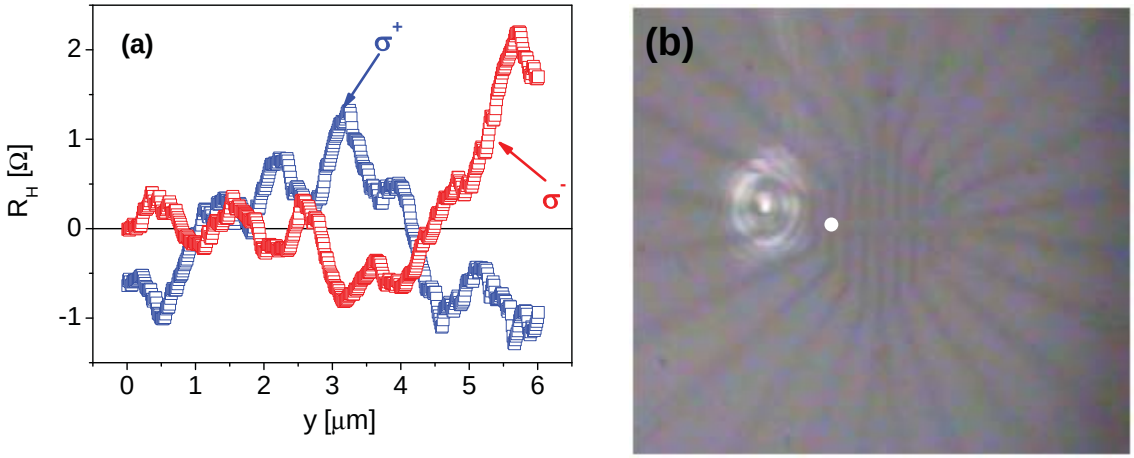

Fig. 4.15. (a) Hal resistance detected at Hall bar 1 as a function of the shift of the excitation laser spot perpendicular to the channel (b) Image of the laser spot location after the experiment where the laser spot was shifted along the channel [Fig. 4.12(b)]. The white point indicates the initial laser spot position.

The first problem concerns the slowly varying background that has already been discussed in connection with Fig. 4.12 (b). This background can be understood if we look at the signal detected at the Hall bars when moving the excitation laser spot perpendicular to the channel (y direction) – see Fig. 4.15 (a). Clearly, the same slowly varying trace that forms the background of the SIHE data (see Fig. 4.12) is generated as a result of the y motion that causes injection of the photoelectrons with various directions of the $\boldsymbol{k}$-vector with respect to the spin-orbit field. In Fig 4.15 (b) we show the picture taken by the camera directly after the spot-sweep experiment where the data presented in Fig. 4.12 (b) were obtained. The white point indicates the initial position of the laser spot and we see that that the motion along the channel is accompanied by significant shift in the perpendicular direction, which probably results from the misalignment of the objective with respect to the sample plane.

The second experimental issue is connected with the oscillatory behavior of the photocurrent that is apparent from Fig. 4.15. These oscillations are connected with multiple reflections of the laser beam from the cryostat windows and it can be circumvented by a slight tilt of the objective with respect to the cryostat. Though this effect might seem trivial, it has to be carefully prevented as the precession frequency of the oscillations in the photocurrent is similar to the real SIHE signal and it projects into the Hall resistance signal.

4.3.3 "Current mixing" experiment

In the previous chapter we demonstrated the spin-injection Hall effect (SIHE) generated by spin-polarized charge current and by pure spin current. So far, the presence of SIHE has been considered only in the systems where carrier transport takes place in purely diffusive regime, and

the spin of the carriers is manipulated using the spin-orbit (SO) coupling [5]. However, the spin current $\boldsymbol{j}_s$ is connected not only with the carrier spins (s) but also with their velocity ($\boldsymbol{v}$) [149]:

$$j_s = \hat{s}v \tag{4.7}$$

Consequently, the spin current can be influenced not only by changing the spin polarization s [43] but also by changing the *velocity* of the carriers. This can be done experimentally by introducing the drift component to the purely diffusive spin current using an additional external electric field [150].

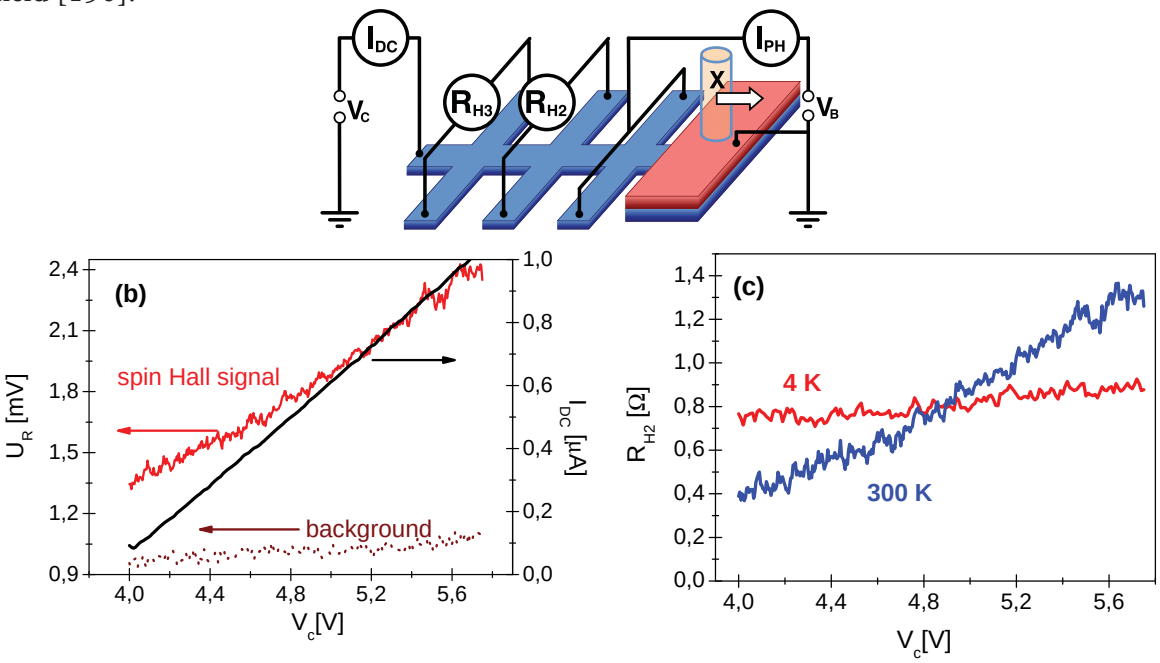

Fig. 4.16. (a) Schematic depiction of the experimental setup in the "current mixing" experimental configuration, where the additional voltage V_c is applied along the N region of the channel. V_B is the voltage across the PN junction, and IPH the photocurrent. (b) Hall voltage detected at room temperature at Hall bar 2 after excitation by the circularly ("spin Hall signal") and linearly ("background") polarized light. For comparison, the DC current through the N channel is shown (c) Hall resistance measured at room (300 K) and low (5 K) temperatures.
For all the measurements, the conditions are as follows: V_B = -5 V, I_{PH} ~ 1 μA

In our work, we propose a realization of this spin current manipulation using the voltage V_C applied along the N-type channel of the planar photodiode. This voltage causes an additional, spin-unpolarized current (I_{dc}). Schematic illustration of the experimental configuration is depicted in Fig. 4.16 (a), and the Hall voltage V_H measured at room temperature at Hall bar 2 as a function of V_C in this configuration is presented in Fig. 4.16 (b) together with the current I_{dc} measured along the channel. While the background detected after excitation with linearly polarized light does not depend on V_c, the Hall voltage increases, and it scales roughly with the additional current flowing through the channel. Knowing the photocurrent I_{PH} through the PN junction, we can calculate the Hall resistance R_H. The corresponding R_H measured at room temperature (RT) and at T = 4 K, is depicted in Fig. 4.16 (b) and (c) after the subtraction of the background. Clearly, the Hall resistance increases upon application of a higher V_C, the increase being more pronounced at RT where the channel conductivity is higher.

Both of the above described findings strongly suggest that in this case we indeed add an additional drift component to the spin current. This leads to the conjecture that we can achieve spin amplification by the additional unpolarized charge current in the SIHE experiment.

However, these results can be regarded only as preliminary and further experimental work would be needed to study this phenomenon.

4.4 Towards the Spin Hall Effect Transistor

Even though the working principle of the spin field effect transistor (S-FET), was proposed more than 20 years ago [1], its experimental realization turned out to be a challenging problem and it has been solved only recently [148]. In its original concept, the S-FET would work in the ballistic regime. The Rashba spin-orbit coupling is modified by an electrostatic gate, which enables manipulation with the spin of the electrons in the two dimensional channel [2]. Spin injection and detection in the original S-FET scheme are realized through an interface between a semiconductor and a metallic ferromagnet.

The "Spin Hall Effect (SHE) transistor" proposed in [43] is based on a similar principle as the original Datta-Das scheme – the spin precession induced by spin-orbit coupling is controlled by external gate electrodes in the 2DEG channel. The electrodes are fabricated as the unetched P-type top layers in the N-channel of the heterostructure described earlier.For spin injection, an optical method is used (see **Chap. 4.2.2**), which enables all-semiconductor design of the device with no external magnetic field required for operation. Unlike in the original S-FET proposal, the detection is provided by the inverse Spin Hall Effect (iSHE) that was demonstrated in **Chap. 4.3.2** (D). The non-destructive detection method is suitable for incorporation of more gates within one transistor and, consequently, for realizing logic operations [43].

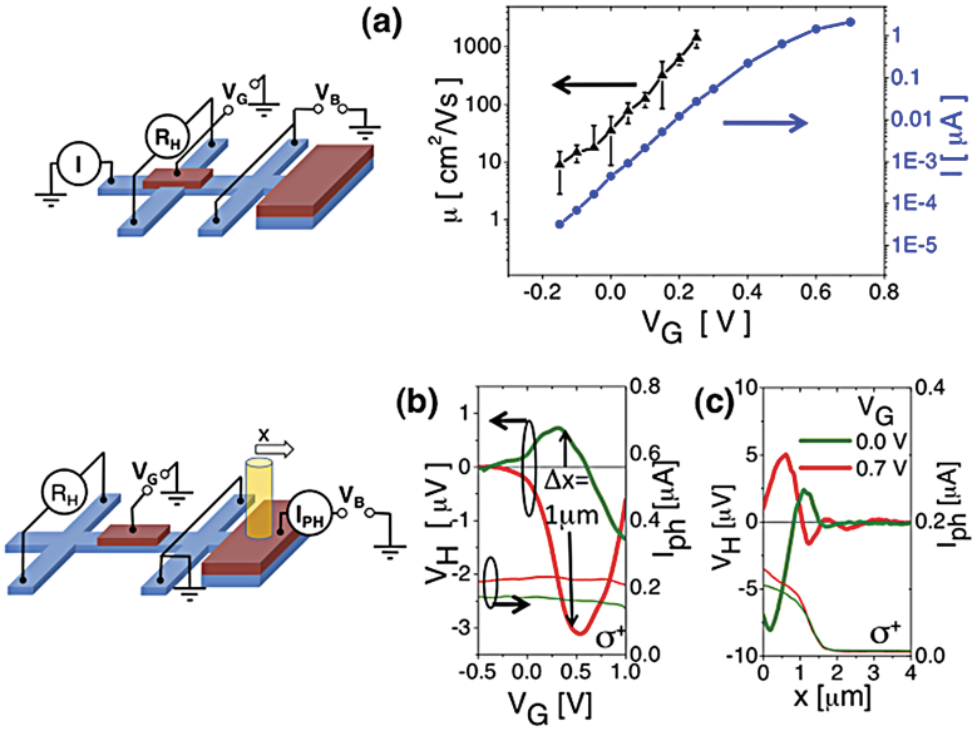

Fig. 4.17. Spin Hall effect transistor: (a) Schematics of the measurement setup corresponding to the conventional field-effect transistor and experimental dependence of the electrical current (blue) through the channel and mobility (black) underneath the gate on the gate voltage. (b) Schematics of the setup of the spin Hall transistor and experimental Hall signals as functions of the gate voltage at a Hall cross placed behind the gate electrode for two light spot positions with a relative shift of 1μm and the green curve corresponding to the spot shifted further away from the detection Hall cross. (c) Hall signals as functions of the spot-positions for two different gate voltages, $V_G = 0$ (green) and $V_G = 0.7V$ (red). The thin green and red curves in (b,c) correspond to the respective photo-currents.(Data presented in (a-c) are taken from Ref. [43])

The conventional FET functionality and a demonstration of the new S-FET properties are shown in Fig. 3.17 (a) and (b), (c), together with a schematic depiction of the experimental settings in the individual configurations. The standard FET is obtained if the gate is placed between the detecting Hall bars, as presented in Fig. 3.17 (a), where we show the gate voltage dependence of the channel current and mobility underneath the gate. At zero gate voltage, we detect only a small residual channel current consistent with the partial depletion of the 2DEG in the unetched part of the heterostructure. By applying forward or reverse voltages below 1 V, we can open or close the 2DEG channel, respectively, at a negligible gate-channel leakage current.

The sensitivity of the measured Hall signal at the cross placed behind the gate on the voltage applied to the gate electrode is shown in Fig 4.17 (b). In order to exclude any potential gate voltage dependence of spin-injection conditions in the device, the experiments are performed with the electrical current drained before the gated part of the channel (see **Chap. 4.3.2 C**). The data show two regimes of operation of the SHE transistor. At large reverse voltages the Hall signals disappear as the diffusion of spin-polarized electrons from the injection region towards the detecting Hall cross is blocked by the repulsive potential of the intervening gate electrode. Upon opening the gate, the Hall signal first increases, in analogy to the operation of the conventional field-effect transistor. While the optically generated current I_{PH} is kept constant, the electrical current in the manipulation and detection parts of the transistor channel remains zero at all gate voltages. The onset of the output transverse electrical signal upon opening the gate is a result of a pure spin current. The initial increase of the detected output signal upon opening the gate shown in Fig. 4.17(b) is followed by a non-monotonic gate voltage dependence of the Hall voltage. This is in striking contrast to the monotonic increase of the normal electrical current in the channel observed in the conventional field-effect-transistor measurement in Fig. 4.17(a). Apart from blocking the spin-current at large reverse gate voltages, the intermediate gate electric fields are modifying spin precession of the injected electrons and therefore the local spin polarization at the detecting Hall cross when the channel is open. This is the spin manipulation regime analogous to the original Datta-Das proposal. The presence of this regime in the device is further demonstrated by comparing two measurements shown in Fig. 3.17 (b), one where the laser spot is aligned close to the lateral p-n junction on the p-side (red, bold line) and the other one with the spot shifted by approximately 1 μm in the direction away from the detecting Hall crosses (green, bold line). The reverse voltage at which the Hall signals disappear is the same in the two measurements. For gate voltages at which the channel is open, the signals are shifted with respect to each other in the two measurements, have opposite signs at certain gate voltages, and the overall magnitude of the signal is larger for smaller separation between injection and detection points, all confirming the spin precession origin of the observed effect. Further evidence of the gate-voltage dependent variation of spin precession underneath the gate electrode is shown in Fig. 3.17 (c), where the phase shifted Hall signal variations as functions of the spot position for two different gate voltages, $V_G = 0$ (green bold line) and $V_G = 0.7\ V$ (red, bold line) are compared. The photocurrents (thin green and red lines) drop down to zero when exceeding the light-spot position of 2 μm away from the etch-step in the p-region.

One of the important attributes of our nondestructive spin detection method integrated together with the electrical spin manipulation, along the semiconductor channel is the possibility of fabricating devices with a series of Hall cross detectors and also with a series of gates that

can lead to a logic functionality of the device. Such multiple-gate transistors were successfully prepared, and a logic AND operation was demonstrated. The details exceed the scope of this work and can be found in Ref. (43)

4.5 Conclusions

In conclusion, we presented the results obtained by measuring the Spin-Injection Hall Effect (SIHE) in the planar photovoltaic cell with a broad PN junction, motivated by fabrication of the spin Hall transistor. The main achievement of this experimental part is in the demonstration of direct detection of spin dynamics in the space domain by shifting the position of the carrier injection point and detecting simultaneously the Hall signal at different Hall bars. Using the standard configuration with the spin-polarized charge current sent through the channel, the Hall signal corresponds to the direct observation of SIHE. On the other hand, if the charge current is drained before the detection Hall bars, the signal reflects the spin dynamics by an inverse Spin-Hall effect. These experiments open a way to compare directly the spin dynamics with the theoretical models, and they show a good agreement with the up-to-date theoretical prediction for the spin precession period (1.3 μm). Furthermore, the pure spin current measurement turned out to be of special importance for the construction of the spin Hall transistor that works purely in the diffusive regime and uses inverse Spin Hall Effect for the polarization detection. Such a spintronic device is not only an experimental realization of the Datta-Das type of spin-transistor but it also extends the concept into new functionalities in terms of integration of logic operations within one component.

In addition to the above described experiments dedicated to the observation of the spin precession in the diffusive regime, we also suggested a possibility to influence the spin dynamics by introducing an additional electric field. The field adds a drift component to the spin current that results in spin amplification.

SUMMARY

Spintronics is a relatively new field in physics that aims to incorporate spin of the carriers to create new functionalities in standard electronic components. The goal of this doctoral thesis was to explore spin dynamics in such semiconductor systems that have potential in spintronics applications in order to unveil some of the laws that rule spin precession in different types of the inherent effective fields. The systems of interest were based on semiconductor GaAs that is both commonly used in standard electronics and theoretically well described, and thus it forms an ideal starting point for the studies.

In our work we followed two distinct semiconductor spintronic concepts. First, the ferromagnetic order in the magnetically doped common semiconductor ("diluted magnetic semiconductor") was studied on a model system (Ga,Mn)As. Using the methods of ultrafast laser spectroscopy, we observed the laser-induced magnetization precession both in native (Ga,Mn)As and in hybrid multiferroic devices (Ga,Mn)As/piezo stressor. The thorough exploration of such magnetization dynamics helped us understand the processes behind laser excitation of magnetic semiconductors with circularly polarized light. This in turn led to the proposition of a model that describes the precession as motion of the magnetization in a quasi-equilibrium anisotropy field. We found out that the precession can be triggered not only by the transfer of energy from laser pulses but also by transfer of angular momentum from optically injected spin-polarized electrons. The latter effect can be understood as an optical analogy to the well-known and used spin transfer torque (STT). In contrast, the optical STT is a new and unexplored phenomenon with vast impact on spintronics applications, as the relevant timescales are in the order of tens of femtoseconds. In addition to the discovery of the optical STT effect, the detailed understanding of the origin of magnetization precession enabled us to perform efficient optical and voltage control by piezo-stressing.

The second spintronics concept is based on a complete exclusion of the magnetic parts from the devices, and all the manipulation with the spin states is done by a spin-orbit (SO) interaction. We studied the GaAs/AlGaAs heterostructures patterned to form a planar two dimensional electron/hole gas photodiode with a special type of SO coupling symmetry that shows a spin helix state with extremely long coherence time. We demonstrated a new method to directly electrically detect this spin precession in space domain using the measurement of the transverse Hall signal as a function of the position of the spin injection point. The possibility to generate a varying Hall signal by a pure spin current (i.e. with no net charge current flowing) helped to propose a new, spin-current based Hall effect transistor that can incorporate multiple gates and thus perform integrated logic operations.

BIBLIOGRAPHY

[1] I. Žutić, J. Fabian, S. Das Sarma: *Spintronics: Fundamentals and Applications.* Revue of Modern Physics **76,** 323 (2004)

[2] S. Datta, and B. Das: *Electronic analog of the electrooptic modulator*. Applied Physics Letters **67**, 155201 (1990)

[3] N. Samarth: *Solid State Physics.* Elsevier Academic Press 58, (2004)

[4] J. D. Koralek, C. P. Weber, J. Orenstein, B. A. Bernvig, S-Ch. Zhang, S. Mack, and D. D. Awschalom: *Emergence of the persistent spin helix in semiconductor quantum wells*. Nature **458**, 610 (2010)

[5] J. Wunderlich, A. C. Irvine, J. Sinova, B. G. Park, L. P. Zarbo, X. L. Xu, B. Kaestner, V. Novák, and T. Jungwirth: *Spin-injection Hall effect in a planar photovoltaic cell*. Nature Physics **5**, 675 (2009)

[6] T. Dietl: *A ten-year perspective on dilute magnetic semiconductors and oxides*, Nature Physics **9**, 965 (2010).

[7] R. Winkler: *Spin-Orbit Coupling Effects in Two-Dimensional Electron and Hole Systems,* Springer-Verlag, Heidelberg - Berlin, (2007)

[8] J. H. Davies: *The physics of low-dimensional semiconductors*, Cambridge University Press, Cambridge (1998)

[9] Y. Kato, R. C. Myers, A. C. Gossard, and D. D. Awschalom: *Coherent spin manipulation without magnetic fields in strained semiconductors,* Nature **427,** 50 (2004)

[10] S.A.Crooker, and D.A. Smith: *Imaging Spin Flows in Semiconductors Subject to Electric, Magnetic, and Strain Fields*, Physical Review Letters **94**, 236601 (2005)

[11] B. Habib, J. Shabani, E. P. De Poortere, M. Shayegan, and R. Winkler: *Anisotropic low-temperature piezoresistance in (311)A GaAs*. Applied Physics Letters **91**, 012107 (2007)

[12] J. Wenisch, C. Gould, L. Ebel, J. Storz, K. Pappert, M.J.Schmidt, C. Kumpf, G. Smidt, K. Brunner, and L.W.Molenkamp: *Control of Magnetic Anisotropy in (Ga,Mn)As by Lithography-Induced Strain Relaxation*. Physical Review Letters **99**, 077201 (2007)

[13] A. W. Rushforth, E. De Ranieri, J. Zemen, J. Wunderlich, K. W. Edmonds, C. S. King, E. Ahmad, R. P. Campion, C. T. Foxon, B. L. Gallagher, K. Výborný, J. Kučera, and T. Jungwirth: *Voltage control of magnetocrystalline anisotropy in ferromagnetic-semiconductor-piezoelectric hybrid structures*. Physical Review B **78**, 085314 (2008)

[14] D. Sprinzl: *Dynamika spinově polarizovaných nosičů náboje v polovodičích*. doktorská práce, Univerzita Karlova v Praze (2009)

[15] M. I. Dyakonov: *Spin physics in semiconductors.* Springer-Verlag, Berlin - Heidelberg, (2009)

[16] J.A. Gupta: *Coherence and Manipulation of Spin States in Semiconductor Nanostructures.* doctoral thesis, University of California, Santa Barbara (2002)

[17] A. K. Zvezdin, V. A. Kotov: *Moderen Magnetooptics and Magnetooptical Materials.* Institute of Physics, Bristol, Philadelphia (1997)

[18] A.V. Kimel, G.V. Astakhov, A. Kirilyuk, G. M. Schott, G. Karczewski, W. Ossau, G. Schmidt, L.W. Molenkamp, and Th. Rasing: *Observation of Giant Magnetic Linear Dichroism in (Ga,Mn)As.* Physical Review Letters **94**, 227203 (2005)

[19] J. **Šubrt:** *Studium feromagnetických polovodičů pomocí magnetooptických jevů*. diplomová práce, Univerzita Karlova v Praze, MFF UK, Praha (2009)

[20] T. Jungwirth, P. Horodyská, N. Tesařová, P. Němec, J. Šubrt, P. Malý, P. Kužel, C. Kadlec, J. Mašek, I. Němec,M. Orlita, V. Novák, K. Olejník, Z. Šobáň , P. Vašek, P. Svoboda, and Jairo Sinova: *Systematic Study of Mn-Doping Trends in Optical Properties of (Ga,Mn)As*. Physical Review Letters **102**, 067204 (2010)

[21] A. Kirilyuk, A.V. Kimel, T. Rasing: *Ultrafast optical manipulation of magnetic order.* Revue of Modern Physics **80**, 2731 (2010)

[22] E.Rozkotová: *Dynamika spinově polarizovaných nosičů náboje v polovodičich.* diplomová práce, Univerzita Karlova v Praze, MFF, Praha (2007)

[23] M. Stellmacher, J. Nagle, J. F. Lampion, P. Santoro, J. Vaneecloo, A. Alexandrou: *Dependence of the carrier lifetime on acceptor concentration in GaAs grown at low temperature under different growth and annealing conditions.* Journal of Appied Physics **88**, 6026 (2000)

[24] H. Abe, H. Harima, S. Nakashima, M. Tani, K. Sakai, Y. Tokuda, K. Kanamoto, Y. Abe: *Characterization of crystallinity in low-temperature-grown GaAs layers by Raman scattering and time-resolved photoreflectance measurements.* Japanese Journal of Applied Physics **35** (1), 5955 (1996)

[25] J. Wang, Ch. Sun, Y. Hashimoto, J. Kono, G. A. Khodaparast, Ł. Cywiński, L. J. Sham, G. D. Sanders, Ch. J. Stanton, and Hiro Munekata: *Ultrafast magneto-optics in ferromagnetic III–V.* Journal of Physics: Condensed Matter **18**, R501-R530 (2006)

[26] Q. Zhang, A. V. Nurmikko, A. Anguelouch, G. Xiao, A. Gupta: *Coherent Magnetization Rotation and Phase Control by Ultrashort Optical Pulses in CrO_2 Thin Films*. Physical Review Letters **89**, 177402 (2002)

[27] M. van Kampen, C. Jozsa, J. T. Kohlhepp, P. LeClair, L. Lagae, W. J. M. de Jonge, and B. Koopmans: *All-Optical Probe of Coherent Spin Waves.* Physical Review Letters **88,** 227201 (2002)

[28] F. Hansteen, A. Kimel, A. Kirilyuk, and T. Rasing: *Femtosecond Photomagnetic Switching of Spins in Ferrimagnetic Garnet Films.* Physical Review Letters **95,** 047402 (2005)

[29] H. Back, G. Woltersdorf, *Microwave Assisted Switching of Single Domain $Ni_{80}Fe_{20}$ Elements,* Physical Review Letters **99**, 227207 (2007)

[30] A. V. Kimel, A. Kirilyuk, F. Hansteen, R. V. Pisarev, T. Rasing: *Nonthermal optical control of magnetism and ultrafast laser-induced spin dynamics in solids.* Journal of Physics: Condensed Matter **19**, 043201 (2007)

[31] D. Chiba, M. Sawicki, Y. Nishitani, Y. Nakatani, F. Matsukura, and H. Ohno: *Magnetization vector manipulation by electric fields.* Nature **455**, 515 (2008)

[32] H. Ohno, D. Chiba, F. Matsukura, T. Omiya, E. Abe, T. Dietl, Y. Ohno, and K. Ohtani: *Electric-field control of ferromagnetism*. Nature **408**, 944 (2000)

[33] M. H. S. Owen, et al.: *Low-voltage control of ferromagnetism in a semiconductor p–n junction*. New Journal of Physics **11,** 023008 (2009)

[34] J. M. Kikkawa, and D. D. Awschalom: *Lateral drag of spin coherence in gallium arsenide.* Nature **397,** 139 (1999)

[35] Y. K. Kato, R. C. Mayers, A. C. Gossard, D. D. Awschalom: *Observation of the Spin Hall Effect in Semiconductors.* Science **306**, 1910 (2004)

[36] S. A. Crooker, et al.: *Imaging spin transport in lateral ferromagnet/semiconductor structures.* Science **309,** 5744 (2005)

[37] R. Fiederling, et al.: *Injection and detection of a spin-polarized current in a light-emitting diode.* Nature **402,** 787 (1999)

[38] Y. Ohno, et al.: *Electrical spin injection in a ferromagnetic semiconductor heterostructure* . Nature **402**, 790 (1999)

[39] J.-N. Chazalviel: *Spin-dependent Hall effect in semiconductors.* Physical Review B **11,** 3918 (1976)

[40] P. R. Hammar, and M. Johnson: *Detection of Spin-Polarized Electrons Injected into a Two-Dimensional Electron Gas.* Physical Review Letters **88**, 066806 (2002)

[41] S. O. Valenzuela, and M. Tinkham: *Direct electronic measurement of spin Hall effect.* Nature **442**, 176 (2006)

[42] J. Wunderlich, B. Kaestner, J. Sinova, and T. Jungwirth: *Experimental Observation of the Spin-Hall Effect in a Two-Dimensional Spin-Orbit Coupled Semiconductor System.* Physical Review Letters **94**, 047204 (2005)

[43] J. Wunderlich, et al.: *Spin Hall Effect Transistor*. Science **330**, 1801 (2010)

[44] A. Mauger, and S. Godart: *The magnetic, optical, and transport properties of representative of a class of magnetic semiconductors: the europium chalcogenides.* Physical Reports **141**, 56 (1986)

[45] R. S. Weisz: *Interatomic distances and ferromagnetism in spinels.* Physical Review **84**, 379 (1951)

[46] J. K. Furdyna: *Diluted magnetic semiconductors*. Journal of Applied Physics **64**, R29 (1988)

[47]. A. Haury, A. Wasiela, A. Arnoult, J. Cibert, S. Tatarenko, T. Dietl, and Y. Merle d'Aubigné: *Observation of a ferromagnetic transition induced by two-dimensional hole gas in modulation-doped CdMnTe quantum wells.* Physical Review Letters **79,** 511 (1997).

[48] T. Story, R. R. Galazka, R. B. Frankel, and P. A. Wolf: *Carrier-concentration-induced ferromagnetism in PbSnMnTe.* Physical Review Letters **56**, 777 (1986)

[49] H. Munekata, H. Ohno, S. von Molnar, A. Segmüller, L. L. Chang, and L. Esaki: *Diluted magnetic III-V semiconductors.* Physical Review Letters **63,** 1849 (1989)

[50] H. Ohno, H. Munekata, T. Penney, S. von Molnár, and L. L. Chang: *Magnetotransport properties of p-type (In,Mn)As diluted magnetic III-V semiconductors.* Physical Review Letters **68**, 2664 (1992)

[51] H. Ohno: *Making Nonmagnetic Semiconductors Ferromagnetic*. Science **281**, 951 (1998).

[52] H. Ohno, A. Shen, F. Matsukura, A. Oiwa, A. Endo, S. Katsumoto, and Y. Iye.: (*Ga,Mn) As: A new diluted magnetic semiconductor based on GaAs.* Applied Physics Letters **69**, 363 (1996)

[53] F. Matsukura, H. Ohno, A. Shen, and Y. Sugawara: *Transport properties and origin of ferromagnetism in (Ga,Mn)As.* Physical Review B **57,** R2037 (1998)

[54] T. Dietl, H. Ohno, F. Matsukura, J. Cibert, D. Ferrand: *Zener model description of ferromagnetism in zinc-blende magnetic semiconductors.* Science. **287**, 1019 (2000)

[55] A. H. MacDonald, P. Shiffer, and N. Samarth: *Ferromagnetic semiconductors: Moving beyond (Ga,Mn)As.* Nature Materials **4**, 195 (2005)

[56] M. Wang, R. P. Campion, A. W. Rushforth, K. W. Edmonds, C. T. Foxon, and B. L. Gallagher. *Achieving high Curie temperature in (Ga,Mn)As.* Physical Review B **93**, 132103 (2008).

[57] K. S. Burch, J. Stephans, R. K. Kawakami, D. D. Awschalom, and D. N. Basov: *Ellipsometric study of the electronic structure of Ga1-xMnxAs and low-temperature GaAs.* Physical Review B **70**, 205208 (2004)

[58] K. Ando, H. Saito, K. C. Agarwal, M. C. Debnath, and V. Zayets: *Origin of the Anomalous Magnetic Circular Dichroism Spectral Shape in Ferromagnetic* $Ga_{1-x}Mn_xAs$*: Impurity Bands inside the Band Gap.* Physical Review Letters **100**, 067204 (2008)

[59] T. Jungwirth, J. Sinova, J. Mašek, J. Kučera, and A. H. MacDonald: *Theory of ferromagnetic III-V semiconductors.* Revue of Modern Physics **78,** 809 (2006)

[60] S. C. Erwin, A. G. Petukhov: *Self-compensation in manganese-doped ferromagnetic semiconductors.* Physical Review B **89**, 227201 (2002)

[61] T. Dietl, H. Ohno, and F. Matsukura: *Hole-mediated ferromagnetism in tetrahedrally coordinated semiconductors*. Physical Review B **63,** 195205 (2001)

[62] J. Zemen, J. Kučera, K. Olejník, and T. Jungwirth: *Magnetocrystalline anisotropies in (Ga,Mn)As: Systematic theoretical study and comparison with experiment.* Physical Reviw B **80,** 155203 (2009)

[63] C. S. King, J. Zemen, K. Olejník, L. Horák, J.A. Haigh, V. Novák, A. Irvine, J. Kučera, V. Holý, R. P. Campion, B. L. Gallagher, and T. Jungwirth: *Strain control of magnetic anisotropy in (Ga,Mn)As microbars.* Physical Review B **83,** 1115312 (2011)

[64] M. Sawicki, K, Wang, K. Edmonds, R. Campion, C. Staddon, N. Farley, C. Foxon, E. Papis, E. Kaminska, A. Piotrowska, T. Dietl, and B. Gallagher: *In-plane uniaxial anisotropy rotations in (Ga,Mn)As thin films*. Physical Review B **71**, 121302(R) (2005)

[65] U. Welp, V. K. Vlasko-Vlasov, A. Menzel, H. D. You, X. Liu, J. K. Furdyna, T. Wojtowicz: *Uniaxial in-plane magnetic anisotropy of* $Ga_{1-x}Mn_xAs$*.* Applied Physics Letters **85,**260 (2004)

[66] V. Stanciu, and P. Svedlindh: *Annealing-induced changes of the magnetic anisotropy of (Ga,Mn) As epilayers.* Applied Physics Letters **87,** 242509 (2005)

[67] J. M. D. Coey: *Magnetism and Magnetic Materials.* Cambridge University Press, Cambridge (2010)

[68] X. Liu, and J. K.Furdyna: *Ferromagnetic resonance in Ga1–xMnxAs dilute magnetic semiconductors*. Journal of Physics: Condensed Matter **18**, R245 (2006)

[69] K. Olejník: *Preparation and characterization of ferromagnetic GaMnAs epilayers.* doctoral thesis, Charles University in Prague, Prague (2009)

[70] S. Mack, R. C. Mayers, J. T. Heron, A. C. Gossard, and D. D. Awschalom: *Stochiometric growth of high Curie temperature heavily alloyed GaMnAs.* Phys. Rev. B **92**, 192502 (2008)

[71] T. Jungwirth, K. Y. Wang, J. Mašek, K. W. Edmonds, J. König, J. Sinova, M. Polini, N. A. Goncharuk, A. H. MacDonald, M. Sawicki, A. W. Rushforth, R. P. Campion, L. X. Zhao, C. T. Foxon, and B. L. Gallagher: *Prospects for high temperature ferromagnetism in (Ga,Mn)As semiconductors.* Physical Review B **72,** 165204 (2005)

[72] C. Chappert, A. Fert, and F.N.V. Dau: *The emergence of spin electronics in data storage.* Nature Materials **6**, 813 (2007)

[73] D. C. Ralph, and M. D. Stiles: *Spin transfer torques.* Journal of Magnetism and Magnetic Materials **320**, 1190 (2008)

[74] E. Beaurepaire, J.-C. Merle, A. Daunois, and J.-Y. Bigot: *Ultrafast Spin Dynamics in Ferromagnetic Nickel*. Physical Review Letters **76**, 4250 (1996).

[75] B. Koopmans, M. van Kampen, J. T. Kohlhepp, and W. J. M. de Jonge: *Ultrafast Magneto-Optics in Nickel: Magnetism or Optics?* Physical Review Letters **85,** 844 (2000)

[76]. J. Wang, I. Cotoros, K. M. Dani, X. Liu, J. K. Furdyna, and D. S. Chemla: *Ultrafast Enhancement of Ferromagnetism via Photoexcited Holes in GaMnAs.* Physical Review Letters **98**, 217401 (2006)

[77] A. V. Kimel, A. Kirilyuk, A. Tsvetkov, R. V. Pisarev, and Th. Rasing: *Laser-induced ultrafast spin reorientation in the antiferromagnet $TmFeO_3$*. Nature **429**, 850 (2004)

[78] G. Ju, et al.: *Ultrafast Generation of Ferromagnetic Order via a Laser-Induced Phase Transformation in FeRh Thin Films.* Physical Review Letters **93,** 197403 (2004)

[79] J.-U. Thiele, M. Buess, and C. H. Back: *Spin dynamics of the antiferromagnetic-to-ferromagnetic phase transition in FeRh on a sub-picosecond time scale*. Applied Physics Letters **85**, 2857 (2004)

[80] B. Hillebrands, G. Ounadjela: *Spin Dynamics in Confined Magnetic Structures I*.: Springer, (2001)

[81] M. Djordjevic-Kaufman: *Magnetization dynamics in all-optical pump-probe experiments:spin-wave modes and spin-current damping*. doctoral thesis, Georg-August-Universitat zu Gottingen, Gottingen (2006)

[82] B. Lenk, H. Ulrichs, F. Garbsa, and M. Münzenberg: *The building blocks of magnonics.* Physical Reports - in press.

[83] B. Lenk, G. Eilers, J. Hamrle, and M. Münzenberg: *Spin-wave population in nickel after femtosecond laser pulse excitation.* Physical Review B **82,** 134443 (2010)

[84] W. K. Hiebert, A. Stankiewicz, and M. R. Freeman: *Direct Observation of Magnetic Relaxation in a Small Permalloy Disk.* Physical Review Letters **79**, 1134 (1997)

[85] X. Liu, Y. Y. Zhou, and J. K. Furdyna: *Angular dependence of spin-wave resonances and surface spin pinning in ferromagnetic (Ga,Mn) As films.* Physical Review B **75,** 195220 (2007)

[86] A. H. Morris: *Physical principles of magnetism*. Wiley, New York (1965)

[87] K. Khazen: *Ferromagnetic Resonance Investigation of GaMnAs Nanometric Layers.* doctoral thesis, Université Paris VI - Pierre et Marie Curie Institut des NanoSiences de Paris, Paris (2008)

[88] Kh. Khazen, H. J. von Bardeleben, M. Cubukcu, J. L. Cantin, V. Novak, K. Olejnik, M. Cukr, L. Thevenard and A. Lemaître: *Anisotropic magnetization relaxation in ferromagnetic $Ga_{1-x}Mn_xAs$ thin films.* Physical Review B **78**, 195210 (2008)

[89] C. D. Stanciu, A. V. Kimel, F. Hansteen, A. Tsukamoto, A. Itoh, A. Kirilyuk, and Th. Rasing: *Ultrafast spin dynamics across compensation points in ferrimagnetic GdFeCo*. Physical Review B **73**, 220402 (2006)

[90] T. Kobayashi, H. Hayashi, Y. Fujiwara, and S. Shiomi: *Damping parameter and wall velocity of RE-TM films*. IEEE Transactions on Magnetics **41**, 2848 (2005)

[91] G. M. Müller, G. Eilers, Z. Wang, M. Scherff, R. Ji, K. Nielsch, C. A. Ross, and M. Mürnzberg: *Magnetization dynamics in optically excited nanostructured nickel films.* New Journal of Physics **10**, 123004 (2008)

[92] A. Comin, C. Giannetti, G. Samoggia, P. Vavassori, D. Grando, P. Colombi, E. Bontempi, L. E. Depero, V. Metlushko, B. Ilic, and F. Parmigiani: *Elastic and Magnetic Dynamics of Nanomagnet-Ordered Arrays Impulsively Excited by Subpicosecond Laser Pulses*. Physical Review Letters 97, 217201 (2006)

[93] V. V. Kruglyak, A. Barman, R. J. Hicken, J. R. Childress and J. A. Katine: *Picosecond magnetization dynamics in nanomagnets: Crossover to nonuniform precession.* Physical Review B **71**, 220409 (2005)

[94] A. V. Kimel, A. Kirilyuk , P. A. Usachev , R. V. Pisarev , A. M. Balbashov, and Th. Rasing: *Ultrafast non-thermal control of magnetization by instantaneous photomagnetic pulses.* Nature **435,** 655 (2005)

[95] F. Hansteen, A. Kimel, A. Kirilyuk, and T. Rasing: *Nonthermal ultrafast optical control of the magnetization in garnet films*. Physical Review B **73**, 014421 (2006)

[96] F. Hansteen, A. Kimel, A. Kirilyuk, and Th. Rasing: *Femtosecond Photomagnetic Switching of Spins in Ferrimagnetic Garnet Films.* Physical Review Letters **95,** 047402 (2005)

[97] J. Fernandez-Rossier, A. S. Nunez, M. Abolfath, and A. H. MacDonald: *Optical spin transfer torque in ferromagnetic semiconductors.* http://arxiv.org/abs/cond-mat/0304492.

[98] X. Liu, Y. Sasaki, and J. K. Furdyna: *Ferromagnetic resonance in Ga1-xMnxAs: Effects of magnetic anisotropy*. Physical Review B **67**, 205204 (2003)

[99] L. Thevenard, L. Largeau, O. Mauguin, A. Lemaître, K. Khazen, and H. J. von Bardeleben: *Evolution of the magnetic anisotropy with carrier density in hydrogenated* $Ga_{1-x}Mn_xAs$. Physical Review B **75**, 195218 (2007)

[100]. Kh. Khazen, H. J. von Bardeleben, J. L. Cantin, L. Thevenard, L. Largeau, O. Mauguin, and A. Lemaître. Ferromagnetic resonance of Ga0.93Mn0.07As thin films with constant Mn and variable free-hole concentrations. Physical Review B. 2008, Vol. 77, p. 165204.

[101] J.K. Furdyna, X. Liu, and Y.Y. Zhou: *Magnetic excitations in ferromagnetic semiconductors*. Journal of Magnetism and Magnetic Materials **321,** 695 (2009)

[102] A.Werpachowska, and T. Dietl: *Theory of spin waves in ferromagnetic (Ga,Mn)As.* Physical Review B **82,** 085204 (2010)

[103] S. T. B. Goennenwein, et al.: *Spin wave resonance in* $Ga_{1-x}Mn_xAs$. Applied Physics Letters **82**, 730 (2002)

[104] Y. Sasaki, X. Liu, T. Wojtowicz, and J. K. Furdyna: *Spin Wave Resonances in GaMnAs*. Journal of Superconductivity **16**, 143 (2003)

[105] T. G. Rappoport, P. Redliński, X. Liu, G. Zaránd, J. K. Furdyna,and B. Jankó: *Anomalous behavior of spin-wave resonances in $Ga_{1-x}Mn_xAs$ thin films.* Physical Review B **69**, 125213 (2004)

[106] C. Bihler, W. Schoch, W. Limmer, S. T. B. Goennenwein,and M. S. Brandt: *Spin-wave resonances and surface spin pinning in Ga1–xMnxAs thin films.* Physical Review B **79**, 045205 (2009)

[107] H. Takechi, A. Oiwa , K. Nomura , T. Kondo , and H. Munekata: *Light-induced precession of ferromagnetically coupled Mn spins in ferromagnetic (Ga,Mn)As.* Physica Status Solidi (c) **3**, 4267 (2006)

[108] A. Oiwa, H. Takechi, and H. Munekata: *Photoinduced magnetization rotation and precessional motion of magnetization in ferromagnetic (Ga,Mn)As.* Journal of Superconductivity **19**, 9 (2005)

[109] Y. Hashimoto, S. Kobayashi, and H. Munekata: *Photoinduced precession of magnetization in ferromagnetic (Ga,Mn)As*. Physical Review Letters **100,** 067202 (2008)

[110] J. Qi, et al.: *Coherent magnetization precession in GaMnAs induced by ultrafast optical excition.* Physical Review B **79,** 085304 (2009)

[111] J. Qi, Y. Xu, A. Steigerwald, X. Liu, J. K. Furdyna, I. E. Perakis, and N. H. Tolk: *Ultrafast laser-induced coherent spin dynamics in ferromagnetic $Ga_{1-x}Mn_xAs$/GaAs structures.* Physical Review B **79**, 085304 (2009)

[112] S. Kobayashi, Y. Hashimoto, and H. Munekata: *Investigation of an effective anisotropy field involved in photoinduced precession of magnetization in (Ga,Mn)As.* Journal of Applied Physics **105**, 07C519 (2009)

[113] D. M. Wang, Y. H. Ren, X. Liu, J. K. Furdyna, M. Grimsditch, and R. Merlin: *Light-induced magnetic precession in (Ga,Mn)As slabs: Hybrid standing-wave Damon-Eshbach modes.* Physical Review B **75,** 233308 (2007)

[114] Y. Hashimoto, and H. Munekata: *Coherent manipulation of magnetization precession in ferromagnetic semiconductor (Ga,Mn)As with successive optical pumping.* Applied Physics Letters **93,** 202506 (2008)

[115] K. Suda, S. Kobayashi, J. Aoyama, and H. Munekata: *Photo-Induced Precession of Magnetization in (Ga,Mn)As Microbars.* IEEE Transactions on Magnetics **46**, 2421 (2010)

[116] M. Overby, A. Chernyshov, L. P. Rokhinson, X. Liu, and J. K. Furdyna: *GaMnAs-based hybrid multiferroic memory device.* Applied Physics Letters **92**, 192501 (2008)

[117] S. T. B. Goennenwein, M. Althammer, C. Bihler, A. Brandlmaier, S. Geprägs, M. Opel, W. Schoch, W. Limmer, R. Gross, and M. S. Brandt: Piezo-voltage control of magnetization orientation in a ferromagnetic semiconductor. Phys. Stat. Sol. (RRL). 2008, Vol. 2, p. 96.

[118] E. Kojima, R. Shimano, Y. Hashimoto, S. Katsumoto, Y. Iye, and M. Kuwata-Gonokami: *Observation of the spin-charge thermal isolation of ferromagnetic $Ga_{0.94}Mn_{0.06}As$ by time-resolved magneto-optical measurements.* Physical Review B **68**, 193203 (2003)

[119] N. Tesařová, P. Němec, E. Rozkotová, F. Trojánek and P. Malý: *Light-Induced Precession of Magnetization in Ferromagnetic Semiconductor (Ga,Mn)As.* Acta Physica Polonica A **118**, 1065 (2010)

[120] P. Němec, E. Rozkotová, N. Tesařová, F. Trojánek, K. Olejník, J. Zemen, V. Novák, M. Cukr, P. Malý, and T. Jungwirth. *Non-thermal laser induced precession of magnetization in ferromagnetic semiconductor (Ga,Mn)As.* ArXiv: Cond. Matt. 1101.1049. 2011.

[121] Khazen, K. oral communication.

[122] N. Tesařová, oral communication.

[123] H. Son, S. Chung, S.-Y. Yea, S. Kim, T. Yoo, S. Lee, X. Liu and J. K. Furdyna: *Vertical gradient of magnetic anisotropy in the ferromagnetic semiconductor (Ga,Mn)As film.* Applied Physics Letters **96,** 092105 (2010)

[124] D. Butkovičová: I*nvestigation of spin polarization in semiconductors by laser spectroscopy.* diploma thesis, Charles University in Prague, Prague (2011)

[125] P. Němec, E. Rozkotová, N. Tesařová, F. Trojánek,E. De Ranieri, K. Olejník, J. Zemen, V. Novák, M. Cukr, P. Malý, and T. Jungwirth: *Experimental observation of the optical spin transfer torque*. accepted to Nature Physics

[126] N. Tesařová, doctoral thesis, to be published.

[127] D.M. Wang, Y.H. Ren, X. Li, J.K. Furdyna, M. Grimsditch, and R. Merlin: *Ultrafast optical study of magnons in the ferromagnetic semiconductor GaMnAs.* Superlattices and Microstructures **41**, 372 (2007)

[128] K. Olejník, M. H. S. Owen, V. Novák, J. Mašek, A. C. Irvine, J. Wunderlich, and T. Jungwirth: *Enhanced annealing, high Curie temperature, and low-voltage gating in (Ga,Mn)As.* Physical Review B **78**, 054403 (2008)

[129] J. Wunderlich, et al.: *Local control of magnetocrystalline anisotropy in (Ga,Mn)As microdevices: Demonstration in current-induced switching*. Physical Review B **76**, 054424 (2007)

[130] C. Bihler, M. Althammer, A. Brandlmaier, S. Geprägs, M. Weiler, M. Opel, W. Schoch, W. Limmer, R. Gross, M. S. Brandt, and S. T. B. Goennenwein: *$Ga_{1-x}Mn_xAs$/piezoelectric actuator hybrids: A model system for magnetoelastic magnetization manipulation*. Physical Review B **78,** 045203 (2008)

[131] Low voltage co-fired multilayer stacks, rings and chips for actuation. [Online] 2011. *http://www.piezomechanik.com/en/home/allcatalogs/index.html.*

[132] Micro-Measurements - Strain Gages and Applications. Tech Note: TN-505-4, TN 504-1, TN 507-1. [Online] *http://www.vishaypg.com/micro-measurements*.

[133] J. Zemen: oral communication.

[134] M. Shayegan, K. Karrai, Y. P. Shkolnikov, K. Vakili, E. P. De Poortere, and S. Manus. *Low-temperature, in situ tunable, uniaxial stress measurements in semiconductors using a piezoelectric actuator.* Applied Physics Letters **83,** 5235 (2003)

[135] A. S. Núnez, J. Fernández-Rossier, M. Abolfath, and A. H. MacDonald. *Optical control of the magnetization damping in ferromagnetic semiconductors.* Journal of Magnetism and Magnetic Materials **1913,** 272 (2004)

[136] D. Chiba, F. Matsukura, and H. Ohno.: *Electric-field control of ferromagnetism in (Ga,Mn) As*, Applied Physics Letters **89,** 162505 (2006)

[137] G. Ju, A. V. Nurmikko, R. F. C. Farrow, R. F. Marks, M. J. Carey, and B. A. Gurney: *Ultrafast Time Resolved Photoinduced Magnetization Rotation in a Ferromagnetic/Antiferromagnetic Exchange Coupled System.* Physical Review Letters 82, 3705 (1999)

[138] P. Horodyská: *Spin Dynamics of Charge Carriers in Semiconductor Nanostructures*, doctoral thesis, Charles University in Prague, Prague (2008)

[139] N. Nagaosa, J. Sinova, S. Onoda, A. H. MacDonald, and N. P. Ong: *Anomalous Hall effect.* Revue of Modern Physics **82**, 1539 (2010)

[140] M. I. D'Yakonov, and V. I. Perel: *Current-induced spin orientation of electrons in semiconductors.* Physical Letters A **35**, 459 (1971)

[141]. S. Murakami, N. Nagaosa, and S. CH. Zhang: *Dissipationless Quantum Spin Current at Room Temperature.* Science **301**, 1348 (2003)

[142] J. Sinova, D. Culcer, N.A. Sinitsyn, T. Jungwirth, and A. H. MacDonald: *Universal Intrinsic Spin Hall Effect.* Physical Review Letters **92**, 126603 (2004)

[143] B. A. Bernevig, J. Orenstein, and S.-Ch. Zhang: *Exact SU(2) Symmetry and Persistent Spin Helix in a Spin-Orbit Coupled System*. Physical Review Letters **97,** 236601 (2006)

[144] B. A. Bernevig, T. L. Hughes, and S.-C. Zhang: *Quantum Spin Hall Effect and Topological Phase Transition in HgTe Quantum Wells*. Science **314**, 1757 (2006)

[145] B. Kaestner, J. Wunderlich, J. Sinova, T. Jungwirth: *Co-planar spin-polarized light-emitting diodes.* Applied Physics Letters **88**, 091106 (2006)

[146] B. Kaestner, D. G. Hasko, and D. A. Williams: *Lateral p-n junction in modulation doped AlGaAs/GaAs.* Japanese Journal of Applied Physics **41**, 4513 (2002)

[147] M. Yamanouchi, D. Chiba, F. Matsukura, and H. Ohno: *Current-induced domain-wall switching in a ferromagnetic semiconductor structure.* Nature **428**, 539 (2004)

[148] C. Brune, et. al.: *Evidence for the ballistic intrinsic spin Hall effect in HgTe nanostructures.* Nature Physics **6**, 448 (2010)

[149]. K. Olejník, J. Wunderlich, A.C. Irvine, R. P. Campion, V. M. Amin, J. Sinova, and T. Jungwirth*: Spin Hall transistor with electrical spin injection.* ArXiv. 1202.0881v1. 2012.

[150]. H. Ch. Koo, J. H. Kwon, J. Eom, J. Chang, S. H. Han, and M. Johnson: *Control of spin precession in a spin-injected field effect transistor.* Science **325**, 1516 (2009)

[151] J. Wunderlich: oral communication